Winter 2014

Ultrasonic Real-Time Quality Monitoring Of Aluminum Spot Weld Process

Waldo Josue Perez Regalado
University of Windsor

Ultrasonic Real-Time Quality Monitoring Of Aluminum Spot Weld Process

by

Waldo Josue Perez Regalado

A Dissertation
Submitted to the Faculty of Graduate Studies
through Electrical and Computer Engineering
in Partial Fulfillment of the Requirements for
the Degree of Doctor of Philosophy at the
University of Windsor

Windsor, Ontario, Canada

2013

Ultrasonic Real-Time Quality Monitoring Of Aluminum Spot Weld Process

by

Waldo Josue Perez Regalado

APPROVED BY:

_____

Dr. Cliff Lissenden, External Examiner
Pennsylvania State University, Department of Engineering Science and Mechanics.

_____

Dr. William McConkey, Outside Reader
Department of Physics

_____

Dr. Majid Ahmadi
Department of Electrical and Computer Engineering

_____

Dr. Jonathan Wu
Department of Electrical and Computer Engineering

_____

Dr. Roman Gr. Maev, Advisor
Department of Physics, and Electrical and Computer Engineering

October 22, 2013

DECLARATION OF ORIGINALITY

I hereby certify that I am the sole author of this thesis and that no part of this thesis has been published or submitted for publication.

I certify that, to the best of my knowledge, my thesis does not infringe upon anyone's copyright nor violate any proprietary rights and that any ideas, techniques, quotations, or any other material from the work of other people included in my thesis, published or otherwise, are fully acknowledged in accordance with the standard referencing practices. Furthermore, to the extent that I have included copyrighted material that surpasses the bounds of fair dealing within the meaning of the Canada Copyright Act, I certify that I have obtained a written permission from the copyright owner(s) to include such material(s) in my thesis and have included copies of such copyright clearances to my appendix.

I declare that this is a true copy of my thesis, including any final revisions, as approved by my thesis committee and the Graduate Studies office, and that this thesis has not been submitted for a higher degree to any other University or Institution.

ABSTRACT

The real-time ultrasonic spot weld monitoring system, introduced by our research group, has been designed for the unsupervised quality characterization of the spot welding process. It comprises the ultrasonic transducer (probe) built into one of the welding electrodes and an electronics hardware unit which gathers information from the transducer, performs real-time weld quality characterization and communicates with the robot programmable logic controller (PLC). The system has been fully developed for the inspection of spot welds manufactured in steel alloys, and has been mainly applied in the automotive industry.

In recent years, a variety of materials have been introduced to the automotive industry. These include high strength steels, magnesium alloys, and aluminum alloys. Aluminum alloys have been of particular interest due to their high strength-to-weight ratio. Resistance spot welding requirements for aluminum vary greatly from those of steel. Additionally, the oxide film formed on the aluminum surface increases the heat generation between the copper electrodes and the aluminum plates leading to accelerated electrode deterioration. Preliminary studies showed that the real-time quality inspection system was not able to monitor spot welds manufactured with aluminum.

The extensive experimental research, finite element modelling of the aluminum welding process and finite difference modeling of the acoustic wave propagation through the aluminum spot welds presented in this dissertation, revealed that the thermodynamics and hence the acoustic wave propagation through an aluminum and a steel spot weld differ significantly. For this reason, the hardware requirements and the algorithms

developed to determine the welds quality from the ultrasonic data used on steel, no longer apply on aluminum spot welds.

After updating the system and designing the required algorithms, parameters such as liquid nugget penetration and nugget diameter were available in the ultrasonic data acquired during the aluminum welding process. Finally, a fuzzy system was designed to receive these parameters and determine the weld quality.

To My Family, the Foundation of My Life.

ACKNOWLEDGEMENTS

I would like to express my most sincere gratitude and deep respect to my supervisor Dr. Roman Gr. Maev. His guidance, encouragement and advice have been invaluable on my personal and professional growth. I would also like to thank Dr. Andrey Chertov for the deep knowledge he generously shared. His support and patience have been very important for the development of this project. Special thanks to the welding group: Anthony Karloff, Janusz Kocimski, Pawel Kustron and Anthony Lui.

I express my gratitude to Dr. Ahmadi, Dr. Wu, Dr. McConkey and Dr. Lissenden, for their role as my committee members.

I want to thank the students that I have had the privilege of supervising for their hard work and the fresh perspective they brought to the project: Mustafa Sheikh, Andrew Ouellette, Mohamed Abdinur and Matheus Zanivan.

My deepest appreciation is given to CONACYT for the financial support received through the scholarship number 198975.

My work is fully dedicated to my family and in memory of my father Juan B. Perez, a great man who always set a great example inspiring me to be a responsible individual. I would like to thank my mother Rosa Maria Regalado for her unconditional love and support. My brothers and sisters: Jose Juan Perez, Noel Perez, Claudia Perez and Luis Perez for sharing all their experiences with me, making me a better person.

Finally, I would like to thank Valeria Espinoza Vega for her support and for being with me through thick and thin.

TABLE OF CONTENTS

LIST OF TABLES

LIST OF FIGURES

CHAPTER I

INTRODUCTION

Foreword

Resistance spot welding has been extensively used in sheet metal fabrication for several decades. The low cost per spot and the ease of process automation make spot welding an attractive joining method for industries such as automotive manufacturing, where thousands of welds bond the final product. In the past, low strength steels were the material of choice compromising over 70% of the materials used in resistance spot welding in the automotive industry [1]. Today, however, a variety of materials can be found within the vehicle structure. These includes high strength steels, magnesium alloys, and aluminum alloys [2][3]. Aluminum has been of particular interest for a number of reasons. First and most importantly, the aluminum alloys under consideration (AA5XXX, AA6XXX) offer strength-to-weight ratio improvements over mild steel on the order of 3:1 [4]. Through this significant weight savings, aluminum structures offer an increase in fuel efficiency without compromising performance or safety. Aluminum also adds an inherent flexibility of design whereby, lighter cars do not need to be smaller and larger cars do not need to be heavier. Another interesting feature of aluminum alloys is that an oxide film is formed on its surface. This oxide layer acts as a barrier against further corrosion, leading to longer lasting and safer vehicles.

The electrical and thermal properties of the material play an important role in the spot welding process. This is clearly seen if we compare the welding process on low strength steels and aluminum alloys. The bulk electrical resistivity of aluminum is quite low (approximately 5 μΩ-cm compared to about 15 μΩ-cm for steel), furthermore, the thermal conductivity of aluminum is greater than that of steel. As a result, if the same electrical current flows through an aluminum stack up and a steel stack up; less heat will be generated on the aluminum due to the low electrical resistivity, also the rate of heat loss from the weld region will be greater in aluminum due to the higher thermal conductivity. These facts indicate that short welding times and high current levels are required to develop the necessary resistance heating to melt aluminum. Three to five times the current and one half the welding time is required to weld an equivalent thickness of aluminum compared to steel. Thermal expansion on aluminum alloys is higher as well, these alloys undergo greater expansion and contraction during the melting and solidification processes than does steel, these dimensional changes are greater in the weld zone and commonly result in weld cracking. Additionally, the aluminum oxide formed on the aluminum surface causes a disadvantage in the resistance spot welding process. With its high electrical resistance, this layer increases the heat generation between the copper electrodes and the aluminum plates leading to rapid electrode deterioration.

A very important aspect for the mass implementation of any manufacturing process is quality control. This is especially the case for the aluminum resistance spot welding (RSW) process. The above-mentioned characteristics indicate that the process is somewhat unstable, with poor robustness and excessive electrode wear. For these reasons, frequent selective quality tests are performed in industry. There are several destructive and non-destructive methods used to inspect the welds. Destructive tests are labour intensive and costly due to its nature. Non-destructive testing (NDT) methods are much more efficient because the part can be re-used after the inspection; however the part being tested still needs to be pulled from the production line and be scanned manually. The latest approach is focused on ultrasonic NDT real time applications. These methods incorporate an ultrasonic probe in one of the welding electrodes, they are fully automated and each spot weld is tested at the moment of its manufacture. This is the direction of the University of Windsor research group, where a revolutionary inspection method was developed [5] [6]. The proposed inspection technique is able to reveal features such as the exact moment of melting, the amount of liquid metal penetration into each plate, the thickness of the weld pool and an estimation of the pool diameter. The method has been successfully applied in the monitoring of low and high strength steel spot welds. Nevertheless, due to the huge differences in the welding process, the direct application of this method to monitor aluminum spot welds is not currently possible. The main objective of this dissertation is to analyze the differences between the ultrasonic monitoring of steel and aluminum alloys and to update the necessary system components and/or processing algorithms to be able to determine the quality of aluminum spot welds.

This chapter will introduce you meticulously to the difficulties of the aluminum spot welding process and the current quality evaluation techniques used in the automotive industry. Finally at the end of the chapter, the scope of the dissertation will be explained and described in detail.

Aluminum Resistance Spot Welding Difficulties

The resistance spot welding process (RSW) consists on squeezing two or more sheets of metal between two copper alloy electrodes, then, an electric current in the order of 10 - 40 KA is passed through the stack up. Figure I-1 shows a typical configuration for the RSW process.

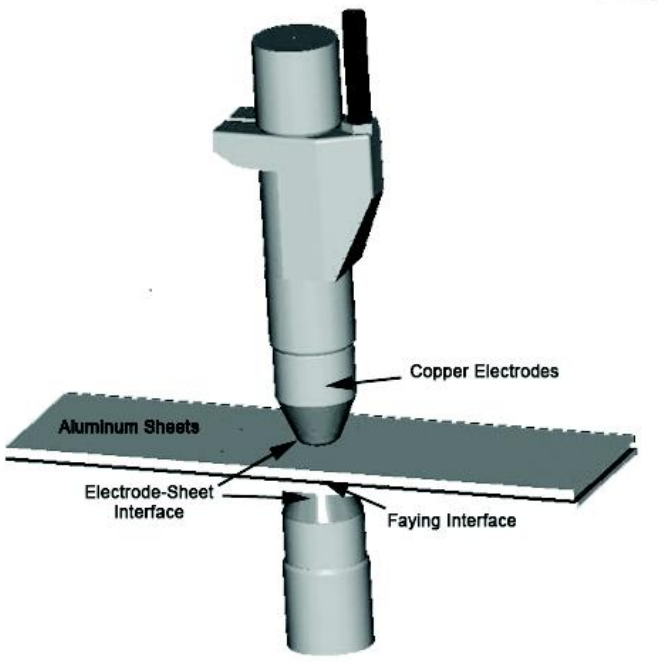

Figure I-1. Typical RSW Configuration

The heat generated on the process follows Joules first law (Equation I-1) which describes the relationship between the heat generated *Q* and the current *I* flowing through a conductor with resistance *R* during the time *t*. The current flows until a portion of the metal between the plates is melted. Finally the plates are held together with the water cooled electrodes until the molten nugget solidifies, creating the joint between the sheets of metal.

$$Q = I^2Rt$$ **Equation I-1**

Aluminum spot welding is based on exploiting the electrical resistance at the faying interface (Figure I-1). However, the resistance at this interface is not the only electrical resistance in the system. In a typical setup there are seven electrical resistances (Figure I-2) in series along the current path [7]. These resistances are summed to give the total resistance. The bulk resistances of aluminum and the copper electrode (R1, R3, R5, R7) are minimal compared with the contact resistances (R2, R4, R6) at the interfaces [8, 9]. Thus, unlike steel, the main heat generation is a consequence of the contact resistance at the interfaces rather than the bulk resistance of the worksheet [10-12].

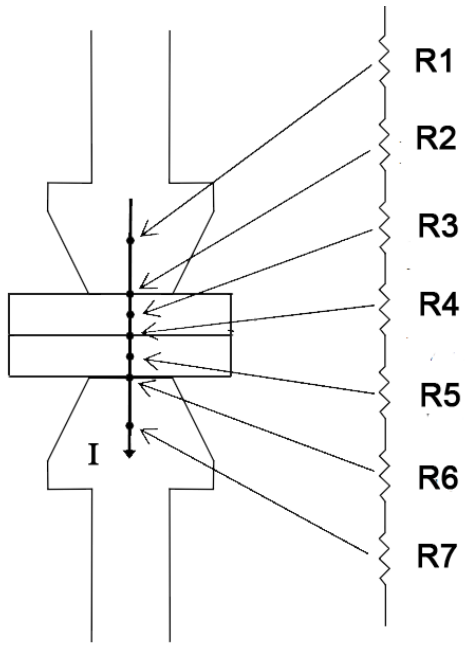

Figure I-2. Electrical resistances on the RSW process

Besides the electrical, the thermal properties of the material are of great importance, these dictate the temperature losses and deformations suffered in the material during welding. Table I-1 highlights the general differences between the aluminum and steel alloys properties [13-17]. Aluminum alloys show roughly three times the thermal conductivity and one-sixth the electrical resistivity compared to steel alloys. As a result, even with its low melting point, aluminum alloys require considerably higher welding currents and shorter welding times. To illustrate this, Table I-2 shows the welding parameters used to successfully weld a pair of 2 mm mild steel and Al6022 aluminum plates [13].

Property	Aluminum	Steel
Melting Temperature (°C)	660	1510
Electrical Resistivity (μΩ-cm)	2.82-5.73	18-45
Thermal Conductivity (W/m-K)	195-237	65-80
Coefficient of Thermal Expansion(10^{-6}/°C)	23	12

Table I-1. Aluminum and steel properties summary

The demand of higher and well controlled currents makes the usage of MFDC (medium frequency direct current) power supplies a necessity for the aluminum resistance spot welding process. These power supplies due to their inherent complexity have a higher cost and shorter life expectancy when compared to an equivalent AC unit. In addition the electrical and water cooling requirements for this setup are significantly higher [18].

Parameter	Al6022	Mild Steel
Current (KA)	31	11.8
Weld Time (ms)	130	416
Force (lbs)	930	900

Table I-2. RSW parameters for Al6022 and mild steels.

Another particular characteristic of aluminum alloys is its natural spontaneous passivation, which consists on the formation of a thin, protective oxide film that limits the potential for further corrosion. This process, for aluminum, can be expressed by the following reaction [19]:

$$4Al + 3O_2 = 2Al_2O_3$$

The process describes the formation of an aluminum oxide barrier when a reaction between aluminum and atmospheric oxygen is present. As this barrier grows, the ability of oxygen molecules to diffuse down to the metal surface is diminished. The process of aluminum oxidation will protect the metal surface, slowing the oxidation rate nearly to zero. The rate at which aluminum-oxide forms, depends upon a number of factors including atmospheric conditions, metal purity, and the presence of an existing oxide film [19]. Recent studies have shown that the oxide layer for pure aluminum, achieves a thickness of 3.5 nm in only 100 ps for an oxide-free surface and that typical oxide thicknesses lay between 3.5 to 10nm [20]. Due to passivity and the intrinsic corrosion resistance properties that it produces, aluminum has become one of the most widely used non-ferrous metals. However, the presence of this layer plays a disadvantage for the spot welding process.

Table I-3 shows a comparison of the properties of interest of the aluminum oxide layer (alumina) and aluminum [21]. From the table it can be seen that alumina with its high electrical resistivity acts as an insulator and that the melting point and hardness of the layer is much higher than the base material. This combination of properties has a huge

impact on the spot welding process. Due to the high electrical resistivity, the current flow is restricted; therefore, theoretically, the electrical current cannot flow into the aluminum plates preventing heat generation at the faying interface. The high melting point indicates that this layer cannot be burnt or removed with the heat generated during the spot welding process without melting the base material. However the difference in hardness between the oxide layer and aluminum plays an important role on the RSW process.

Property	Aluminum	Aluminum Oxide
Hardness (HV)	15	1800
Melting Temperature (°C)	660	2072
Electrical Resistivity (Ωcm)	$2.82\text{-}5.73 \times 10^{-6}$	1×10^{14}

Table I-3. Aluminum oxide and aluminum properties comparison.

Mohamed et al [21] proposed that if the hardness of the oxide layer is higher than the aluminum base alloy, a normal load applied to the metal would cause dislocation movement of the base material in the lateral direction, causing oxide layer fracture. It was shown that in the solid state bonding of high purity aluminum, where the hardness of the oxide layer (1800 HV) is two orders of magnitude higher than the base metal (15 HV), the oxide layer fractures in brittle manner under the normal load. Since the oxide layer is present on every aluminum surface, metal to metal contact can be only established if the cracks on both surfaces aligned together. Although Mohamed's [21] studies were performed on high purity aluminum and did not involve the resistance spot welding

process directly, the loading conditions established represent the tribological interactions during the squeeze cycle of the resistance spot welding process [22].

Surface roughness plays an important role as well. It has been established that the real contact area between two metals is much smaller than apparent area of contact. If we take the aluminum oxide into consideration, the metal to metal contact areas described by Mohamed [21] are further reduced. Studer [23] proposed five contact conditions: metal to metal contact (Region A), areas where a mixed contact (metal-oxide) is present (Region B), regions with no contact at all (Region C) and finally oxide to oxide contacts (Region D). According to several authors, regions A and B are considered the only conduction paths for the electric current [23-25].

High heat generation between the electrode and worksheet material leading to local diffusion [26] occurs. This is caused by the combination of high currents, high contact resistance at the electrode interface and the restriction of current flow described above. Alloying between the electrode and the worksheet and subsequent loss of material from the electrode, is considered as the main electrode degradation mechanism on aluminum RSW [26-28] opposite to steel RSW where electrode degradation is caused mainly by plastic deformation [30]. Dilthey et al [29] performed metallurgical investigation of the electrode degradation during aluminum RSW. They proposed that local diffusion at the copper-aluminum boundary started from the very first weld and that the material transfer sequence follows one of three possible scenarios. The first is known as pick-up and involves the transfer from the worksheet to the electrode. The second is a transfer from the electrode to the worksheet, and is known as electrode pitting. Finally the third case is when pick-up and pitting occurs simultaneously.

Further research on electrode degradation was conducted by Lum [26, 29]. Electrode life tests were performed by acquiring carbon imprints of the electrodes at different stages of the tests. Metallurgical analysis was performed after a specific number of welds with the same electrodes and joint strength measurements were performed by subjecting the spot welds to an increasing shear force until they failed. Electrode life was defined as the weld number when the strength fell below 80% of the initial value [26, 29]. Results showed that the electrode life was in the 400-600 welds range. Lum and Fukamoto [26-29] proposed that electrode degradation follows four different phases. First electrode picks up aluminum from the first weld as tiny molten drops, then copper-aluminum intermetallic compounds ($CuAl_2$, Cu_9Al_4) are formed at the interface between the electrode and the work piece. Finally pitting and consolidation occurs, when the alloyed regions are detached from the electrode, either through a transfer of molten Cu-Al mixture to the worksheet or by the brittle fracture of the solidified intermetallic phases.

Review of Improvements of the Aluminum RSW Process

Short electrode life has been the major issue in the aluminum RSW process. Recommended practices include frequent redressing of the electrodes in order to mitigate the factors that reduce electrode life time [31]. However, for the automotive industry this is not practical, so electrode life becomes a concern. Different methods have been proposed in the literature to improve the spot welding process in aluminum. These methods can be generalized in three categories: aluminum surface pre-treatments, custom electrodes and modified welding equipment.

Li et al in [32] investigated the effects of the aluminum sheet surface conditions on electrode life. The authors systematically compared three different surface pre-treatments: chemical cleaning, degreasing and electric- arc cleaning. An electrode lifetime experiment was performed for each cleaning method. The conclusion of this set of experiments was that when the aluminum sheets were cleaned chemically by soaking the aluminum sheets in NaOH and then HNO_3, the electrode life was extended 10 times. The authors concluded that this cleaning method not only removes greases and impurities from the surface, but also reduces the thickness of the oxide layer.

Another approach for improving the life of the electrodes is the modification of the electrode itself. Spinella and Patrick [33] showed that by reducing electrode face diameter, improvements on electrode life could be achieved. This was related to maintaining specific pressures and current densities as the electrodes wore. Placing surface coatings on the electrode face is another approach that has been explored. Ostgaard [34] and Glagola [35] applied different coatings on the electrode face using different depositing techniques. They found that all the coatings that they tried increased the electrical contact resistance at the electrode-worksheet interface leading to rapid coating and electrode deterioration. Recent developments have been made by Chan and Scotchmer [36]. They presented results where by coating the electrode face with TiC and using current stepping techniques, one pair of electrodes can be able to produce up to 5000 welds. Figure I-3A shows a picture of the coated electrode. The phenomenon was related to taking advantage of roughened surfaces. The asperity on the tips and the force applied helped the conduction paths (regions A and B) for more established metal-to-metal contacts at the electrode interface. Related works by other authors provided

confirmation to this approach. Sigler et al. [37] examined grit blasted electrodes and radially ridged electrodes (Figure I-3B). The studies done did not include electrode life testing. However, weld consistency was improved.

A

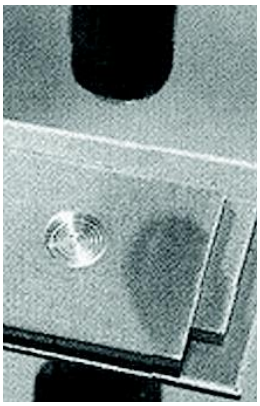

B

Figure I-3. Modified electrodes. A - TiC coated. B- Radially ridged. Courtesy of [39,40]

Finally, another possible option to increase electrode life time is to modify the welding equipment. In [38] a welding controller able to change the polarity of a DC power supply is presented. The polarity is changed after each weld, with this approach the electrodes are deteriorated homogenously increasing its functional lifetime by reducing the Peltier effect. This effect will be described in detail in chapter 3. The maximum electrode life using the proposed welding controller is 1600 welds. Another innovative approach is shown in [39], where a welding gun was designed in order to run a nickel based process tape between the electrodes and the work sheet. By the usage of this tape, a perfect contact surface on every weld is provided. The author claims that each spot weld is identical with 100% reproducibility. However there is no data on how often the process tape should be changed. Figure I-4 shows a picture of this welding gun.

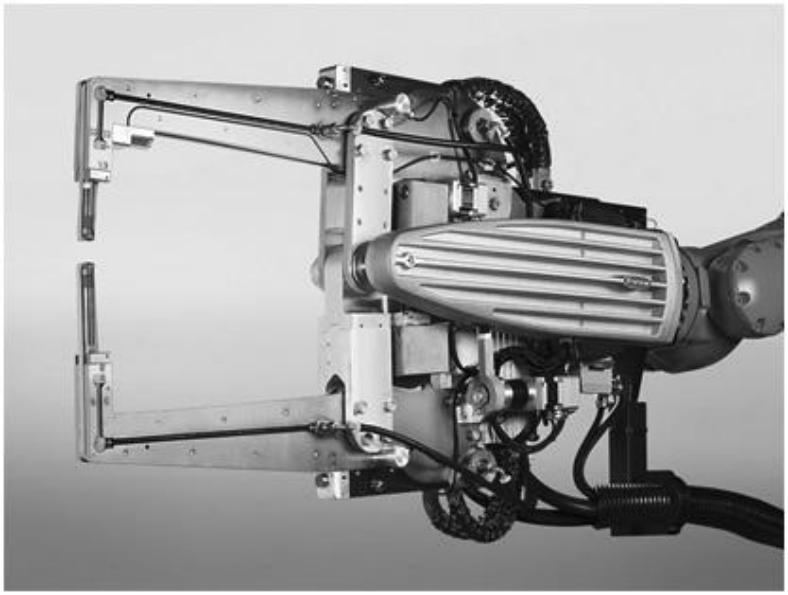

Figure I-4. Process Tape Welding Gun (courtesy of [39])

Spot Weld Quality Evaluation

In the previous section, several approaches to improve the aluminum RSW process were presented. While some of the proposed methods seem to alleviate the electrode deterioration problem, in practice they are hard to implement and the aluminum RSW process still suffers from excessive electrode wear, poor robustness and instability [4]. For this reason, quality control on the aluminum RSW process is of utmost importance.

Non-destructive testing (NDT) of resistance spot weld quality has always been a subject of interest in automotive and other sheet assembly industries. Spot welds ensure structural integrity of the assembly and it is crucial to control the quality of these joints. Periodic destructive tests are common (peel test, chisel test, metallographic analysis) to ensure that technological parameters are within the predefined limits. However, in the recent decades destructive methods have been replaced by non-destructive testing (NDT)

procedures. The usage of NDT inspection not only drops manufacturing costs, but also saves time since it is less labour intensive.

Some of the most common NDT methods for the inspection of resistance spot welds include ultrasonics, thermography and the monitoring of electrical properties such as voltage and resistance. Schlichting et al [42] developed a flash thermography technique able to distinguish between good welds, stick welds and welds at the expulsion limit. Weld characterization was done based on the fact that the smaller the nugget, the higher the lateral thermal gradient.

Ultrasonic methods are by far more utilized to inspect spot welds and have been documented and implemented since the 80's [43]. In this method a piezoelectric transducer located perpendicular to the welded plates, excites acoustic waves which travel across the layered structure and are reflected at the acoustical interfaces within the weld. Conclusions about the weld quality are drawn by analyzing the received pulse-echo patterns. Advance techniques involving phase arrays and 2D matrix array transducers also have been reported. In [44] a tool able to measure the spot weld nugget diameter is presented. The tool uses a 2D matrix transducer; the welded area is scanned with each individual element on the matrix. The presence of a reflection from the area between the metal sheets indicates that the sheets are separated from each other. If the metal is welded, there is no internal reflection, and only the reflection from the bottom of the second sheet can be detected. Using this principle an image of the welded area is created. Figure I-5 shows a comparison between the image created with the ultrasonic tool (B), an acoustic microscope image (A) and the peel test of the weld (C).

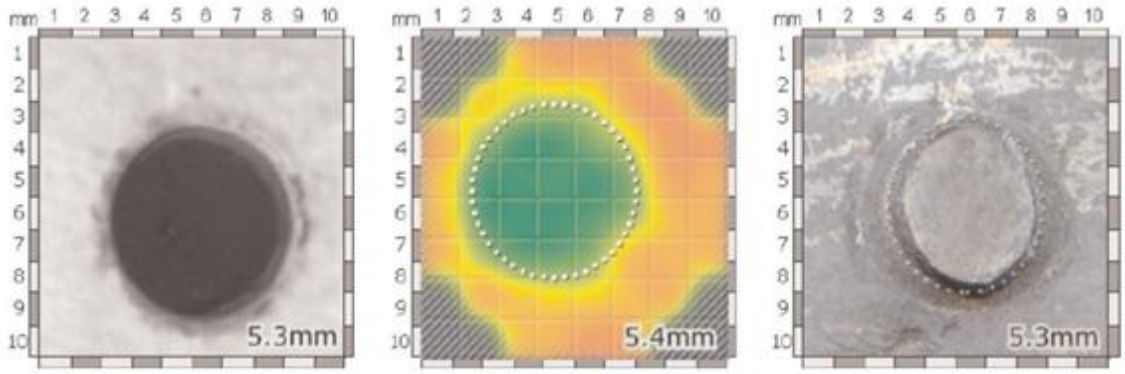

A **B** **C**

Figure I-5. 2D ultrasonic inspection of a spot weld. A- Acoustic microscope image. B – 2D ultrasonic tool. C- Peel test. Courtesy of [44]

Ultrasonic offline NDT techniques prove to be reliable on the inspection of spot welds. However such approaches have their drawbacks: The part to be inspected should be pulled out from the production line and scanned manually. Only a small portion of the produced volume can be inspected and more than 99% of parts are never tested. For this reason, many efforts have been made to develop a real-time spot weld inspection or quality assurance system. Dynamic resistance measurements and electrode displacement monitoring have been studied and applied for quality evaluation. Cho and Rhee [45] combined computer intelligence techniques such as neural networks with dynamic resistance measurements in order to detect patterns and estimate the quality of the weld. In other approaches, monitoring of electrode displacement or force dynamics is used to predict weld quality [46]. Unfortunately, these techniques perform indirect quality estimation based on secondary parameter measurements.

Real time ultrasonic methods have also been tried by many research groups [47-50]. For different reasons, the methods did not make it to the industrial floor. Resistance spot welding has experienced dramatic improvements such as robotization (and thus mechanical stabilization of the process), application of tip dressers (maintaining clean and consistent contact surfaces), use of servo motors, etc. At the same time, electronics hardware, ultrasonic transducer manufacturing technology, computers and software have been improving at exponential rates. It became possible to achieve data acquisitions and processing speeds unimaginable only a decade before. For this reason, our group has put a lot of effort to design a new ultrasonic method for real time spot weld inspection using modern tools and approaches. Preliminary studies showed that the dry ultrasonic contact between copper electrode and steel plate allow enough sound energy through the contact. This is made possible due to high electrode force pushing on the plate (500-1200 lb at contact area of 5-7 mm in diameter). Cooling water stream running inside the electrodes is used as a couplant to convey ultrasonic wave from the probe down into the copper electrode [51]. After several iterations between the industry floor and the lab environment [52] a commercial product was developed. The Real-Time Weld Analyzer (RIWA), a device capable to determine the quality of steel and various types of high strength steel spot welds in real time.

However, the introduction of lighter materials such as aluminum to the automotive industry brought new challenges into the real time inspection of such welds. The short welding times, the high temperature achieved at the electrodes, electrode pitting and the thermo-electrical differences between the steel and aluminum welding

process makes the direct application of the new real time NDT method currently not possible. Therefore, a deep study and development is required.

Scope of the Dissertation

The main focus of this dissertation is the analysis and development of the real-time ultrasonic inspection of the aluminum spot welding process. The current system, able to monitor the steel RSW process (RIWA) should be re-evaluated and the system components should be updated accordingly. Also, the algorithms that determine the quality should be revised and re-designed in order to take into consideration the huge thermodynamic and mechanical differences between the two processes. In order to identify and overcome the difficulties and challenges of this task, a deep knowledge of the welding process is required. For this reason, this dissertation will focus not only on the development of the NDT process, but also on the analysis of good practices and development of new alternatives to improve the stability of the aluminum RSW process.

Chapter 2 describes the physical experimental setup and presents a deep analysis and modeling of the aluminum welding process and the sound propagation principles within the aluminum layered structure. The focus of chapter 3 is to characterize the aluminum spot welding process on dissimilar thickness plates, with the main objective of proposing alternatives to improve the welding process itself and provide guidelines for the ultrasonic monitoring setup. Based on the deep understanding of the welding process developed on the first three chapters, Chapter 4 and 5 describe the main ultrasonic parameters and the signal processing algorithms developed to extract such parameters to

be able to determine the quality of the aluminum spot welds. Finally chapter 6 presents the conclusions and the future work of this research.

References

1. *Fundamental Study of Contact Resistance Behavior in RSW Aluminum,* by M.A Ta-Chien, Ph.D. Dissertation 2003, The Ohio State University.
2. *The Role of Aluminum in Automotive Weight Reduction Part I*, by Y. Kurihara, Journal of Metals 1993, Vol. 45 No. 11, pp. 32-33.
3. *Overall Benefits and Value of Aluminum for an Automobile Body Structure*, by F. Tuler, A. Warren, S. Mariano, and M. Wheeler, Proc. IBEC 1994, Automotive Body Materials, pp. 8-14.
4. *Joining Aluminum Sheet in the Automotive Industry – A 30 Year History*, by J.E. Gould, AWS Welding Journal 2012, Vol. 91, No. 2, pp. 23s-34s.
5. *Transducer Built Into an Electrode*, by R. Maev, A. Ptchelintsev, J. Mann., US Patent Number 6,297,467 B1, Date of Patent Oct.2, 2001.
6. *Ultrasonic In-Process Monitoring and Feedback of Resistance Spot Weld Quality*, US Patent Number 1,688,738 B1, Date of Patent Sep. 27, 2005.
7. *Welding Handbook*. American Welding Society, USA, 1991.
8. *The effect of mechanical loading on the contact resistance of coated aluminum,* by P. S. James, H. W. Chandler, J. T. Evans, D. J. Browne, and C. J. Newton. Materials Science and Engineering A-230 1997, pp. 194-201.
9. *Contact resistance of aluminum*, by P. H. Thornton, A. R. Krause, and R. G. Davies. Welding Journal Research Supplement 1997. Vol. 45, No. 11, pp. 331s-341s.

10. *Modeling dynamic electrical resistance during resistance spot welding*, by S.C. Wang and P.S. Wei. Journal of Heat Transfer 2001. Vol. 123, No. 3, pp. 576-585.
11. *Optimization and Validation of a model to predict the Spot Weldability Parameter Lobes for Aluminum Automotive Body Sheet*, by D. J. Browne, C. J. Newton, and D. Boomer. Proc. Advanced Technologies & Processes 1995, pp. 100-106.
12. *Spot welding of aluminum sheet: a statistical approach to measure the influence of different surfaces*, by M. Thornton, C. Newton, B. Keay, and T. Evans. Proc. Advanced Technologies & Processes 1996, pp. 58-66.
13. *Resistance Welding: Fundamentals and Applications*, by H. Zhang, J. Senkara Second Edition, CRC Press, 2011.
14. *Electrical resistivity of some engineering alloys at low temperatures* by A.F. Clark, G.E. Childs and G.H. Wallace. Cryogenics 1970. Vol. 10, No. 4, pp. 295-305.
15. *Thermal Conductivity of Selected Materials* by R.Powell, C.Y. Ho and P.E. Liley, National Standard Reference Data Series National Bureau of Standards, 1966.
16. *High-Temperature Property Data: Ferrous Alloys*, Editor M.F. Rothman, ASM International, 1988.
17. *Aerospace Structural Materials Handbook*, by W.F. Brown, Mechanical Properties Data Center, Battelle Columbus Laboratories, 1981.
18. *Energy Consumption in AC and MFDC Resistance Spot Welding*, by W. Li, E. Feng, D. Cerjanec and G.A Grzadzinski. Proc. Sheet Metal Welding Conference XI, 2004, pp. 41-49.
19. *Corrosion of Metals: Physicochemical Principles and Current Problems,* By H. Kaesche, First Edition, Springer, 2003.

20. *Dynamics of Oxidation of Aluminum Nanoclusters using Variable Charge Molecular-Dynamics Simulations on Parallel Computers*, by T. Campbell, R. K. Kalia, A. Nakano, and P. Vashishta. Physical Review Letters, June 1999. Vol. 82, Num. 24, pp 4866-4869.

21. *Mechanics of solid state pressure welding*, by H. A. Mohamed and J. Washburn. Welding Journal Research Supplement, 1975. Vol. 9, pp. 302s-310s.

22. *Some Tribological Influences on the Electrode-Worksheet Interface During Resistance Spot Welding of Aluminum Alloys*, by M. Rashid. Journal of Materials Engineering and Performance, 2011. Vol. 20, pp. 456-462.

23. *Contact Resistance in Spot Welding*, by F.J. Studer. The Welding Journal, 1979. Vol. 18, No. 10, pp. 374s-380s.

24. *The effect of surface roughness, oxide film thickness and interfacial sliding on the electrical contact resistance of aluminum*, by E. Crinon and J.T. Evans. Materials Science and Engineering 1998. Vol. A No. 242, pp. 121-128.

25. *Contact Resistance in Spot Welding*, by P. H. Thornton, A. R. Krause, and R. G. Davies. Welding Journal Research Supplement 1996. Vol. 75 No. 12 pp. 402s-412s.

26. *Electrode Pitting in Resistance Spot Welding of Aluminum Alloy 5182*, by I. Lum, S. Fukumoto, E. Biro, D.R. Boomer, and Y. Zhou. Metallurgical and Materials Transaction 2004. Vol. A No. 35, pp. 217-225.

27. *Effect of Electrode Degradation on Electrode Life in Resistance Spot Welding of Aluminum Alloy 5182*, by S. Fukumoto, I. Lum, E. Biro, D.R. Boomer, and Y. Zhou. Welding Journal Research Supplement 2003. Vol. 82, No. 11, pp. 307s-312s.

28. *Electrode deterioration in the medium frequency DC resistance spot welding of 5182 aluminum alloy,* by I. Lum. MASc thesis, University of Waterloo, 2002.

29. *Metallographic Investigation into Wear Processes on Electrodes during the Resistance Spot Welding of Aluminum*, by U. Dilthey and S. Hicken. Proceedings Welding and Cutting 1998, pp. 34-40.

30. *Electrode degradation mechanism during resistance spot welding of zinc coated steel using Cu- TiB_2 electrodes*, by D. Shrjie, Z. Norman, C. Changkun, S. Yaowu, C. Baohua, Trans. Nonferrous Met. Soc. China 2005. Vol. 15, No. 6, pp. 1220-1225.

31. *Welding Theory and Practice*, 4th edition. The Aluminum Association, 2002.

32. *Effects of Sheet Surface Conditions on Electrode Life in Resistance Welding Aluminum*, by Z. Li, C. Hao, J. Zhang, H. Zhang. AWS Welding Journal, 2007. Vol. 82, No. 11, pp. 81s – 89s.

33. *Fundamental effects of electrode wear on aluminum resistance spot welding performance*, by D. J. Spinella, J. R. Brockenbrough, and J. M. Fridy, Sheet Metal Welding Conference XI, 2004. paper 1-1.

34. *Spot welding of aluminum as delivered*, by E. Ostgaard. The Danish Welding Institute, Doc III-614-79, 1979.

35. *Nickel plated electrodes for spot welding aluminum*, by M.A. Glagola and C.A. Roest. SAE-Technical paper-760167, 1976.

36. *Quality and electrode life improvements to automotive resistance welding of aluminum sheet*, by K. R. Chan, and N. S. Scotchmer, Sheet Metal Welding Conference XIII, 2008, paper 5-3.

37. *New electrode weld face geometries for spot welding aluminum*, by D. R. Sigler, J. G. Schroth, M. J. Karagoulis, and D. Zuo, Sheet Metal Welding Conference XIV 2010, paper 5-3.
38. *Resistance Welding*, by L. Dorn, TALAT Lecture 4500 Technische Universität, Berlin.
39. http://www.rwelectrodes.com/v/vspfiles/downloadables/CMW-Catalog.pdf
40. http://media.gm.ca/media/us/en/gm/news.detail.html/content/Pages/news/us/en/2012/Sep/0924_welding.html
41. *Delta Spot*, http://www.fronius.com/cps/rde/xchg/fronius_usa/hs.xsl/3022_2888.htm.
42. *Thermographic testing of spot welds*, by J. Schlichting, S. Brauser, L. A. Pepke, Ch Maierhofer, M. Rethmeier, M. Kreutzbruck. NDT & E International, June 2012.Vol. 48, pp. 23-29.
43. *Resistivity Testing of Spot Welds Challenges Ultrasonics*, by R. Hain. Welding Journal, May 1988.
44. *Spot weld analysis with 2D ultrasonic Arrays*, by A.A.Denisov, C.M. Shakarji, B.B. Lawford, R.G. Maev, J.M. Paille. J. Res. Natl. Inst. Stand. Technol 2004. Vol. 109, No. 2, pp. 233-238.
45. *Quality estimation of resistance spot welding by using pattern recognition with neural networks*, by Y. Cho and S. Rhee. Instrumentation and Measurement, IEEE Transactions 2004. Vol. 53, pp. 330-334.
46. *Real-Time Quality Estimation of Resistance Spot Welding Based on Electrode Displacement Characteristics and HMM* by X. Wang. Proc. Fifth International Conference on Natural Computation 2009 pp. 634-638.

47. *In-process ultrasonic evaluation of spot welds*, by S. I. Rokhlin, S. Meng, and L. Adler. Mater. Eval. 1989. Vol. 47, pp. 935–943.
48. *In-process ultrasonic weld inspection and adaptive control*, by J. E. Sutter. Sheet Metal Welding Conf. XI, Sterling Heights, MI, 2004, paper 2-3.
49. *Method of monitoring a welding operation*, by R. P. Hurlebaus. U.S. Patent 3,726,130, Dec. 9, 1970.
50. *Ultrasonic testing method and apparatus for resistance welding*, by T. Okuda and M. Inada. U.S. Patent 4,099,045, Nov. 29, 1976.
51. *Monitoring of Pulsed Ultrasonic Waves, Interaction With Metal Continuously Heated to the Melting Point*, by R. Gr. Maev, A. Ptchelintsev. Quantitative Non-destructive Evaluation, edited by D. O. Thompson and D.E. Chimenti., AIP Conference Proceedings 2000, pp. 1517-1524.
52. *Integration of the Ultrasonic Real-Time Spot Weld Monitoring System*, by **W. Perez Regalado**, A.M. Chertov, R.Gr. Maev. Proceedings 5th Pan American Conference for NDT, October 2011. Paper 1-24.

CHAPTER II

BASIC PRINCIPLES AND PROBLEM STATEMENT

Real-Time Ultrasonic Monitoring

The real-time weld analyzer (RIWA) consists of a single element ultrasonic transducer built into the welding electrode with a frequency in the range of 5-10 MHz. The transducer uses the cooling water it is submerged in as a coupling medium to deliver sound beyond the replaceable copper electrode cap and further into the welded sheets. The transducer works in pulse-echo mode and receives multiple reflections from the layered structure of the resistance spot weld. The system encloses a custom designed electronics board, a personal computer, and a communications module. The electronics board is in charge of generating short electric pulses to excite the transducer and also to digitize the received analog signals. The personal computer receives the digital data and performs complex pattern recognition algorithms to extract the quality of the weld. Finally, a communications module is connected to the welding equipment to obtain information about the weld being produced and also to provide feedback about the quality of the weld. The schematic of the system setup is shown in Figure II-1 while a photograph of the complete commercial system is shown in Figure II-2. Observe that the PC and the electronics board described above are embedded on the RIWA main unit whereas the ultrasound transducer is already built-in into the welding electrode.

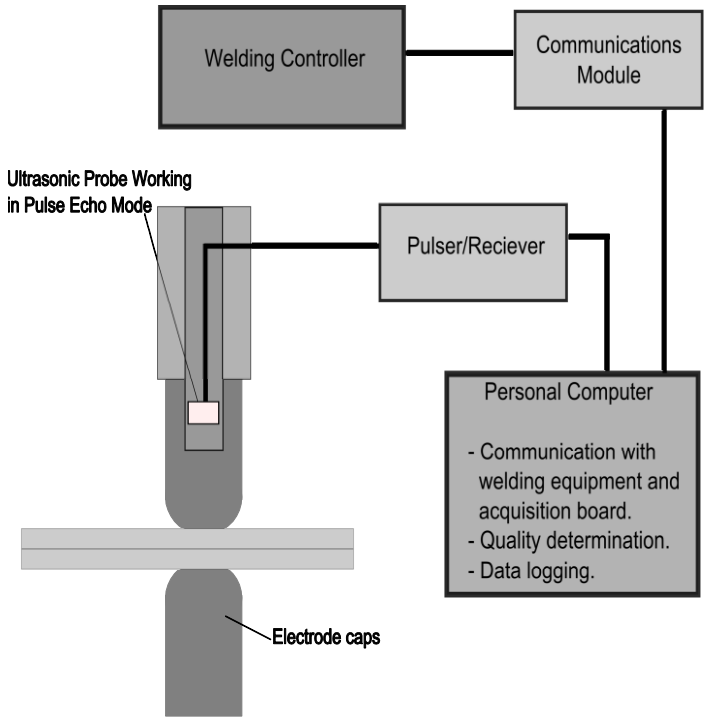

Figure II-1. Schematic of the ultrasonic monitoring setup.

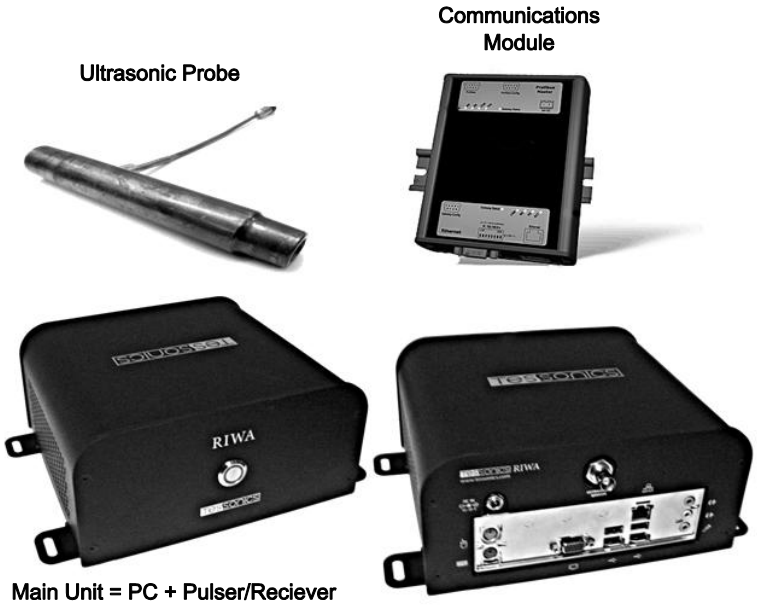

Figure II-2. The real-time integrated weld analyzer (RIWA) system

The system working in pulse-echo mode collects A-scans of the waves passing through the welded plates in the direction perpendicular to the plate's surface. A-scans are gated to allow reflections between the two copper electrodes to be recorded. Figure II-3 shows a schematic of the different reflectors in a standard welding stack up, and a synthetic A-Scan emphasizing the received reflections.

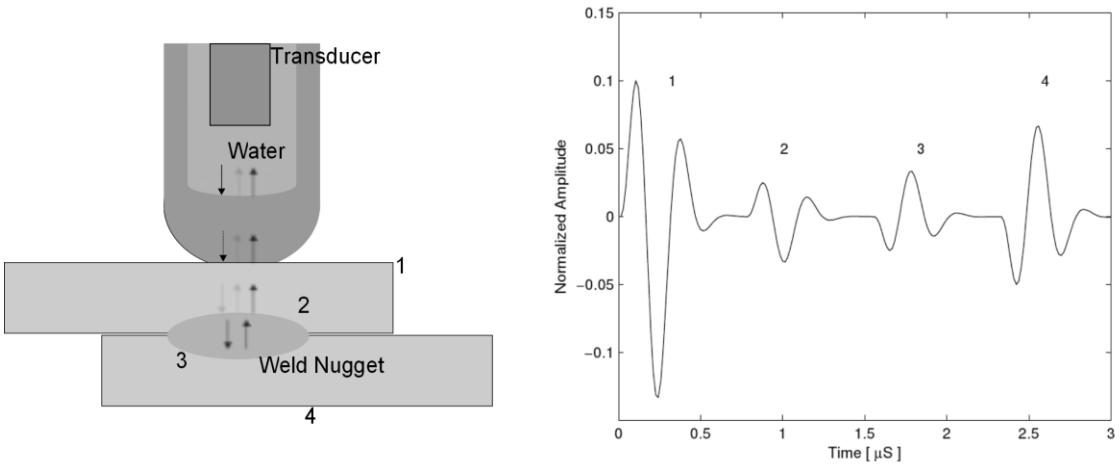

Figure II-3. Reflectors on a 2T stack and synthetic A-Scan

Several A-Scans are acquired at different times during welding in order to form an M-Scan. Figure II-4A shows an ultrasonic M-Scan acquired during the welding process of two 1 mm steel plates. Figure II-4B shows the schematic representation of the M-Scan emphasising the received reflections. Each column of the ultrasonic M-Scan corresponds to an A-Scan acquired at certain time during welding. The amplitude of the received signals is coded on the gray level of the pixels forming the M-Scan. During the squeeze stage of the welding process 3 reflections are visible corresponding to the copper-steel, steel-steel and steel-copper boundaries. These three reflections are labeled

on the schematic view of the M-Scan as 1, 5 and 4 respectively. When the current starts flowing and the temperature starts rising within the plates, reflections 4 and 5 suffer a delay caused by the decrease of sound velocity produced by the temperature increase [1-3]. When melting occurs, the changes in density and elastic properties between solid and liquid material provoke two extra reflections corresponding to the top and bottom of the molten nugget labeled as 2 and 3 respectively. Finally during the cooling phase, the molten nugget shrinks. Both reflections 2 and 3 approach each other until they disappear, which indicates full solidification.

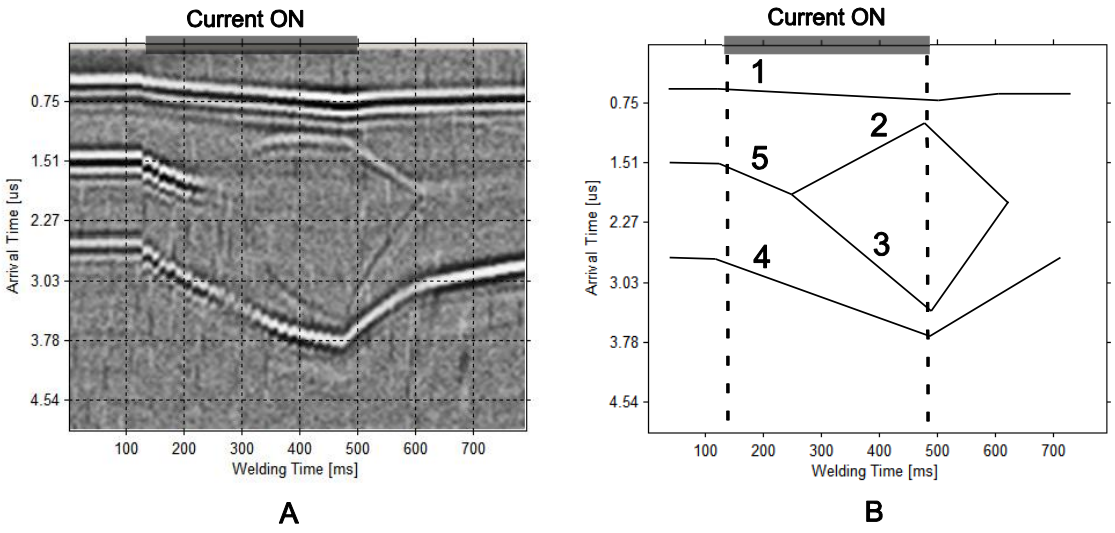

Figure II-4. Ultrasonic M-Scan. A - Ultrasonic data. B - Schematic view

The ultrasonic M-Scan carries significant information about the steel welding process. Extensive research has been conducted on the analysis of the different weld features that can be extracted from the ultrasonic data. One of the well studied parameters is the maximum delay of reflection number 4. As was mentioned above, the main mechanism causing this delay is the velocity drop due to temperature increase. Kurz et al

in [4] performed sound velocity measurements on mild steel above the melting point. Figure II-5 presents the linearization of such measurements and shows the temperature dependence of sound velocity. In the figure it is clearly seen how the increase of temperature, decreases sound velocity. Therefore, the delay of reflection number 4 is higher when the temperature within the plates is elevated. Statistical studies have shown a very high linear correlation between the signal delay and nugget diameter. Maev et al in [7-10] have determined that this delay can be directly used to provide an estimate of the weld nugget diameter without breaking the weld.

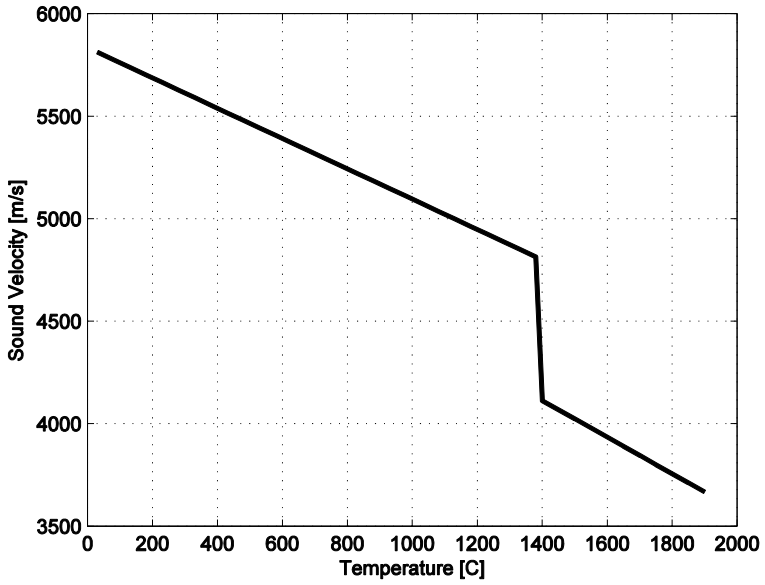

Figure II-5. Linearization of the sound velocity measurements on steel performed by Kurz in [4].

Another parameter used in weld quality characterization is the degree of liquid penetration into the welded plates. Liquid penetration by itself is an important parameter. Automotive standards mandate that this penetration should be above 35% of the stack up thickness [6]. This information can be easily extracted from the ultrasonic data due to

reflections number 2 and 3 which arise due to the acoustic impedance mismatch between the solid and liquid metal [10]. Figure II-6 shows a comparison between the ultrasonic M-Scan and a metallographic cross-section of two steel welds with different liquid penetration. The clear vertical lines shown on the micrographs marked with 1.52 and 1.47 mm respectively, indicate the level of liquid penetration. Therefore, From Figure II-6 it can be seen that there is a correspondence between the liquid penetration measured from the ultrasonic data and the actual fused area observed in the cross sections.

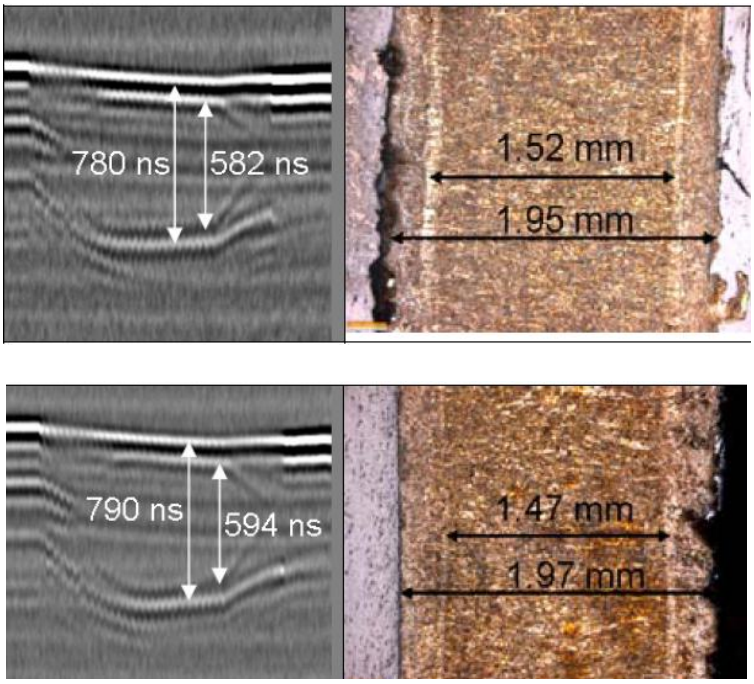

Figure II-6. Ultrasonic M–Scan liquid penetration measurements and its comparison with the welds cross-sections. Courtesy of Chertov [5]

It's important to notice that all the previous results have been obtained for spot welds in the case of steel materials. An early attempt to monitor aluminum welds revealed that the system is not capable of monitoring such welds. Figure II-7 shows an ultrasonic M-Scan acquired during the welding process of two 1 mm aluminum plates.

The figure clearly shows that the ultrasonic features described above are not visible and that the weld quality information that the M-Scan carries is limited.

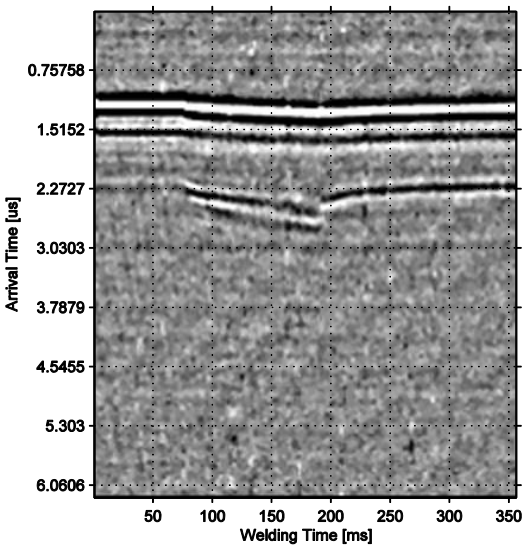

Figure II-7. Aluminum M-Scan

In this chapter a numerical model of the aluminum resistance spot welding (RSW) process will be presented and compared to a steel RSW model. A sound propagation study through aluminum welds will be presented as well. The final section of the chapter will summarize the conclusions of the studies and describe the issues to be solved in order to adapt the RIWA system to monitor the aluminum spot weld process.

Temperature Distributions in an Aluminum Spot Weld

The varying temperature distributions during a welding process causes drastic changes in the elastic properties and density of the material being welded. These changes have an inherent effect on sound velocity and acoustical impedance. These changes are noticeable both as time delays and appearance/disappearance of reflections on the M-Scans. In order to determine the quality of the weld from the ultrasonic data; a deep understanding of the temperature changes is crucial.

To study such temperature gradients, a 2D electro-thermal model was prepared to simulate the RSW process on aluminum. The simulation was done in the software COMSOL Multiphysics. COMSOL is based on the Finite element method which is a well known numerical technique for finding solutions to partial differential equations (PDE).

The system of equations to solve consisted of two PDEs corresponding to the electrical and thermal stages of the model. The governing equation of the electrical stage is shown in

Equation II-1, where ∇ denotes the 2D partial spatial derivatives ($\nabla = \frac{\partial}{\partial x} + \frac{\partial}{\partial y}$), σ electrical conductivity, V the electric potential, j_e the external current density and Q_j the current source.

$$Q_j = -\nabla(\sigma \nabla V - j_e)$$ **Equation II-1**

The transient heat conduction equation shown in Equation II-2 is the governing equation for the thermal stage. Figure II-8 shows the temperature dependence of the electrical resistivity ($^1/_\sigma$), thermal conductivity (k), density (ρ) and specific heat capacity (C_p) on the aluminum plates [10-17]. The properties of the copper electrodes are shown in appendix A.

$$Q = \rho C_p \frac{\delta T}{\delta t} - \nabla(k \nabla T) \qquad \textbf{Equation II-2}$$

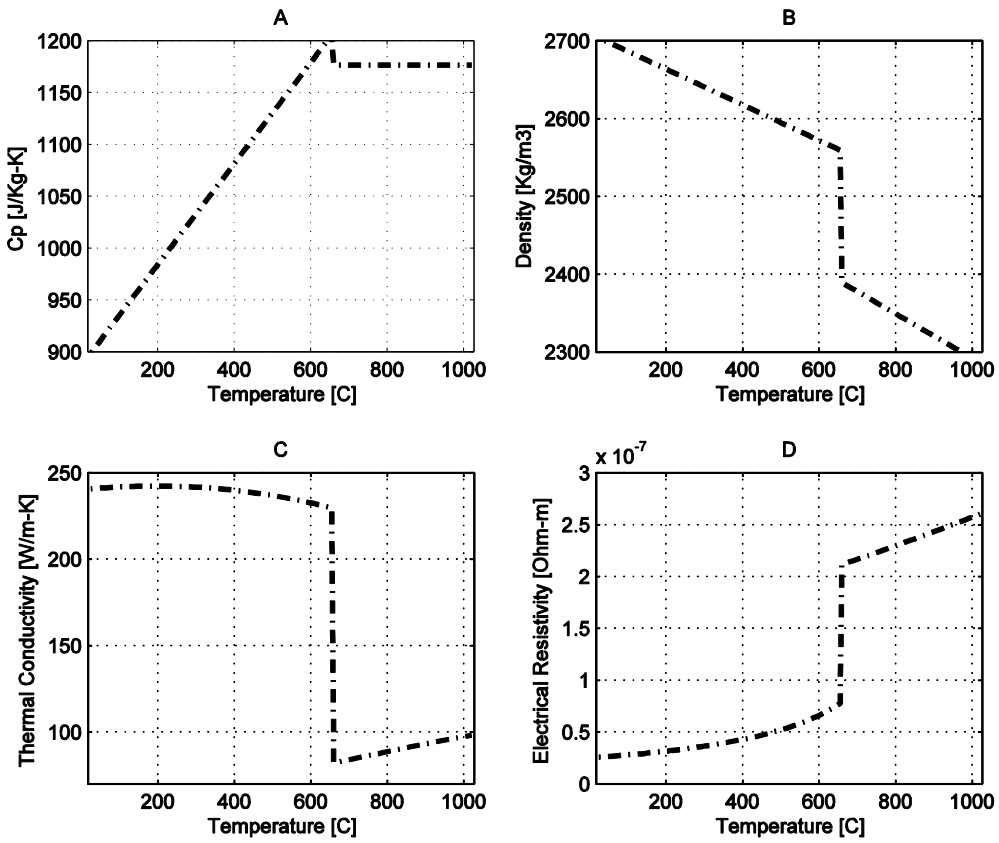

Figure II-8. Temperature dependence of the aluminum properties (melting temperature is 660 °C).

The effects of the load applied during welding were based on the work of Ta-Chien in [18] where the temperature dependence of the contact resistance and contact area under different loads were investigated. Figure II-9 shows the temperature dependence of the contact area. The current density input on the model was adjusted using this relation and the initial contact area of 19.6350 mm^2 (5 mm cap face).

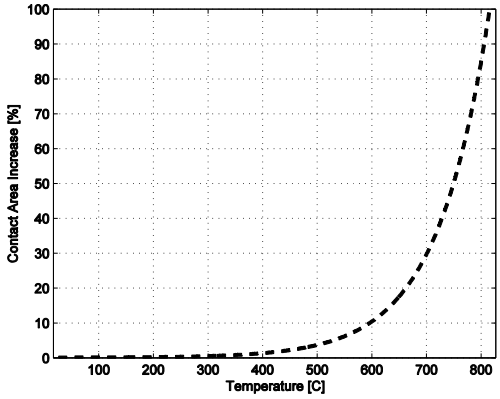

Figure II-9. Contact area. Data courtesy of [18]

The contact resistance at the copper-aluminum interfaces and the aluminum-aluminum interface were modeled using the thin-layer approximation technique described in [19] where, by the usage of assemblies (group of independent geometries) and pairs (boundary condition between assemblies) the effect that thin layers such as the aluminum oxide have on contact resistance can be modeled. Figure II-10 shows the contact resistance data used in the model [18].

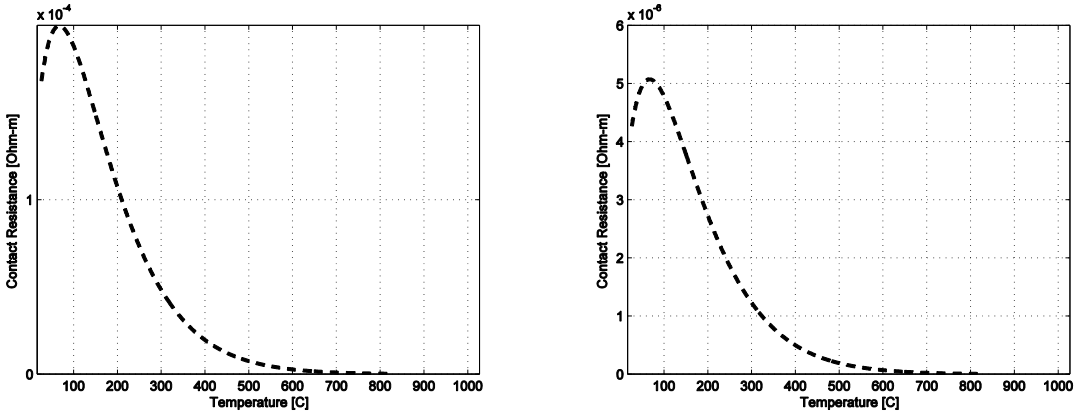

A B

Figure II-10. Contact resistance. A - Al-Al interface. B - Al-Cu interface. Data courtesy of [18]

The heat losses where simulated through heat conduction and the assumption that the electrodes are water-cooled and the temperature of the water maintains a constant temperature of 26 C. Also, the boundaries of the aluminum plates that are not in contact with the copper electrode were modeled assuming that they were air cooled at room temperature.

Figure II-11 shows the axisymmetric geometry used in the model together with a summary of the electrical and thermal boundary conditions. Note that c_a denotes the contact area shown in Figure II-9, ρ_{cc} the contact resistance at the electrode shown in Figure II-10B and ρ_{ca} the contact resistance at the faying interface shown in Figure II-10A.

The initial temperature in the whole geometry was set to 20 C ($T(t_0) = 20\,C$). The simulated welding schedule is shown in Table II-1. Note that the Al2XXX plate thickness is 0.9 mm.

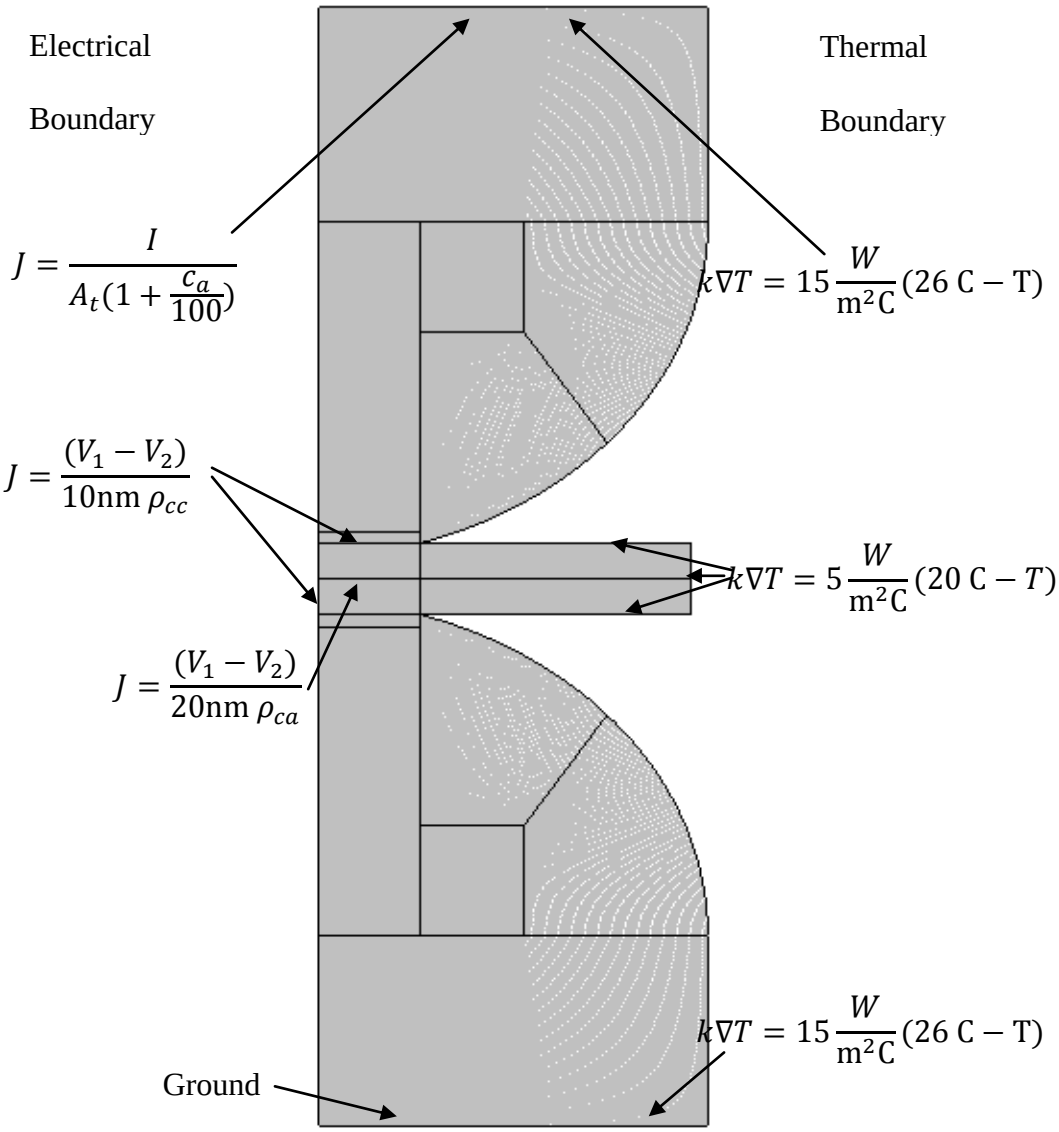

Figure II-11. Boundary conditions summary.

Parameter	Value
Current (KA)	21
Weld Time (ms)	66.7 (4 cycles, 60 Hz)
Force (lbs)	500*

*According to the studies of Ta-Chien in [18].

Table II-1. Simulated welding schedule.

Figure II-12 shows the results of the electric simulation, the surface and streamline plots show the total current density distribution on the geometry at t = 1 ms. In the figure is clearly seen how the maximum current density is located at the periphery of the contact interface. To corroborate this fact, Figure II-13A shows the current density distribution at the electrode interface and Figure II-13B the current density distribution at the faying interface. On both figures the current density profile shows an exponential increase with respect to geometry. The concentration of current density in the periphery is a well documented phenomenon that is attributed to electrode geometry and the diversion that the current has on the worksheets. Figure II-12 clearly shows how the current flows not only towards the center of the plates but also on the lateral direction. The same phenomenon was observed by Geenwood in [21] and Nied in [22] during the investigation of "ring" welds in galvanized steel for the automotive industry. Bowers et al in [23] observed the same concentration of current. However, he attributed this fact to electrode geometry. After modeling truncated electrodes with different angles, he concluded that when the electrode-sheet interface angle approaches 90 degrees the current distribution tends to be uniform.

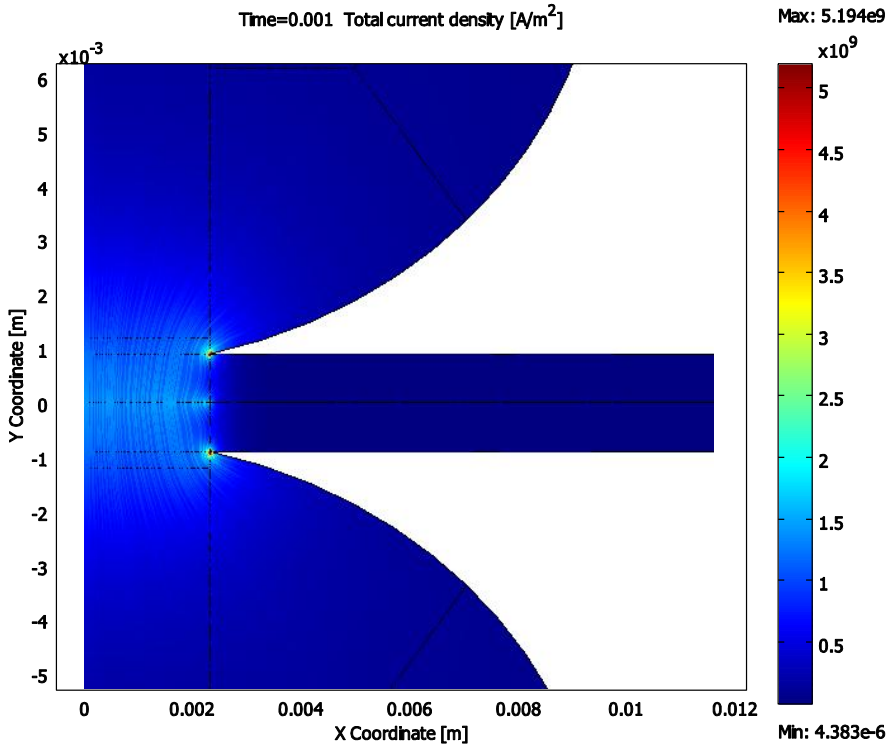

Figure II-12. Current density distribution on the whole geometry.

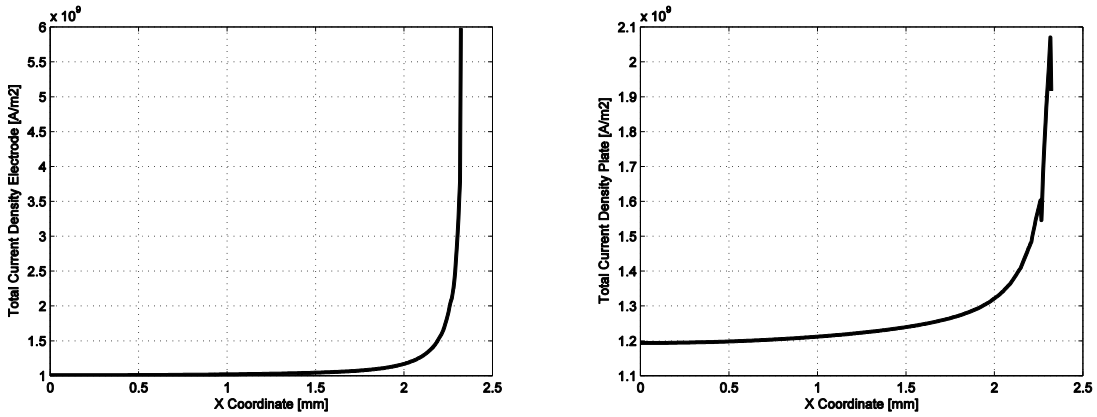

A B

Figure II-13. Current density distribution. A- Electrode-worksheet interface. B- Faying interface.

Figure II-14 to Figure II-17 shows the molten nugget growth dynamics. Nugget formation starts from the very first welding cycle. This is occasioned by the considerable effect that contact resistance has on heat generation. At low temperatures contact resistance is (Figure II-10) significantly higher than the bulk resistivity of aluminum (Figure II-8). Therefore, the heat generation is considerably higher in the first ms of the welding process and is attributed entirely to contact resistance [25-27].

At the end of the first cycle a nugget with 0.3 mm of height and 1.3 mm of diameter is formed (Figure II-14). Figure II-15 and Figure II-16 show the temperature distribution at the end of the second and third welding cycles respectively. The molten nugget grows 0.25 mm in height and 0.9 mm in diameter from the first to the second cycle and 0.2 mm in height and 1 mm in diameter from the second to the third cycle. This growth represents 85% of growth on the vertical direction and 71% on the lateral direction compared to the final nugget size of 0.88 mm of height and 4.5 mm of diameter shown in Figure II-17. Destructive verification revealed an error of 15% between the modeled and real nugget diameter for a 30 welds experiment with two simulated currents (19KA and 21 KA).

Once that melting occurs, the contact resistance stops playing a role on heat generation and the bulk resistivity of the material is the main contributor for the heat generation within the plates. This resistance increases with temperature at a very low rate. In addition, the contact area increases significantly as the temperature increases (Figure II-9) causing a drop in current density. The combination of these two events cause a decrease of the heat generation on the second half of the welding process reducing nugget growth during this stage.

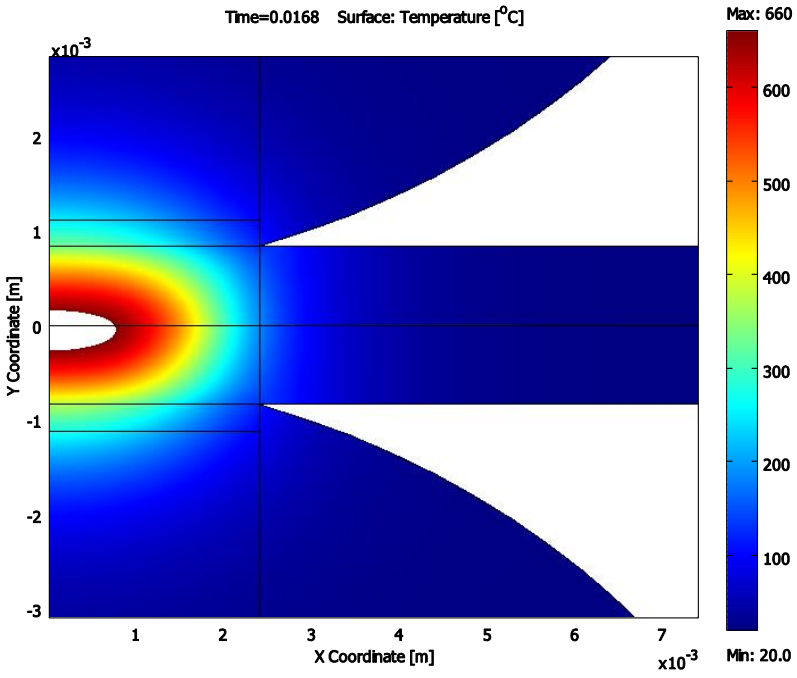

Figure II-14. Temperature distribution at the end of the first cycle.

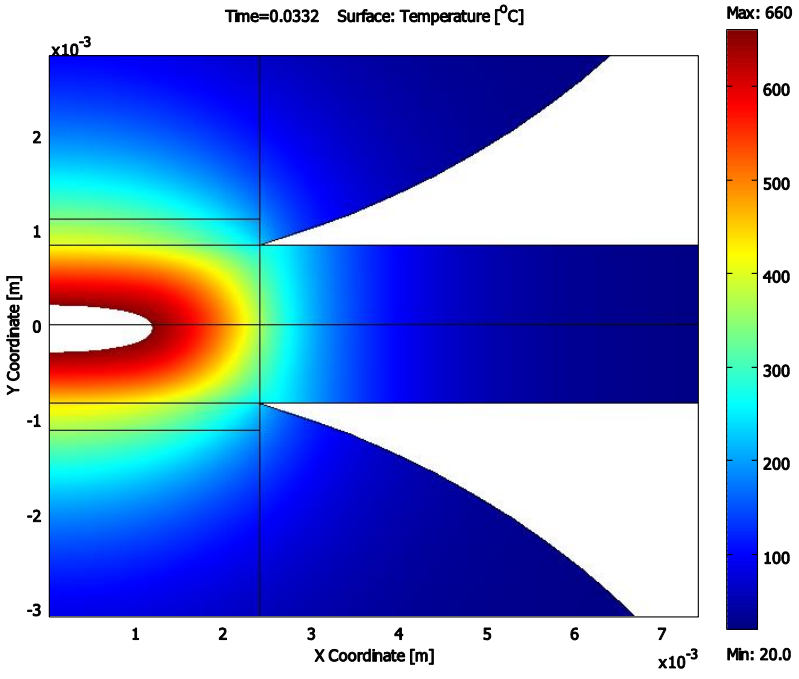

Figure II-15. Temperature distribution at the end of the second cycle.

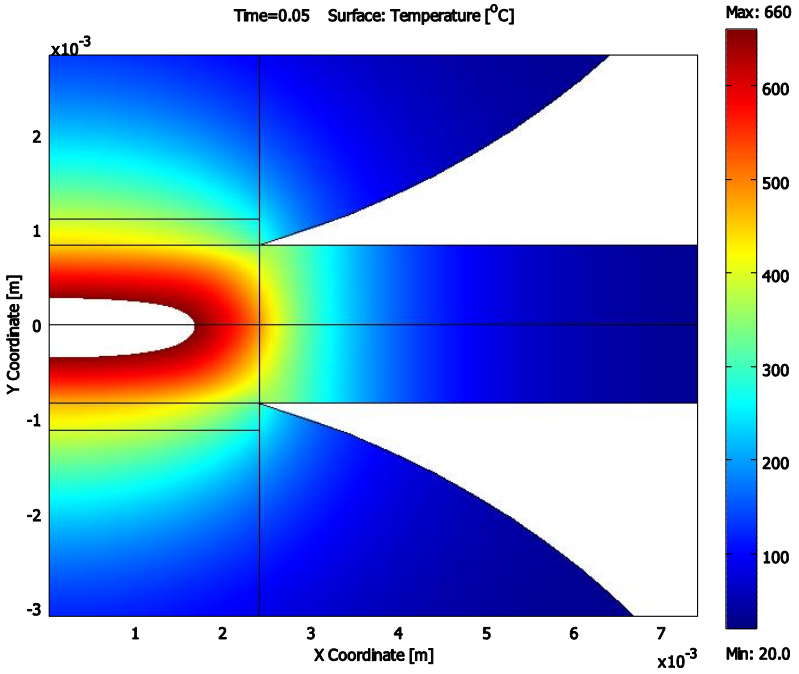

Figure II-16. Temperature distribution at the end of the third cycle.

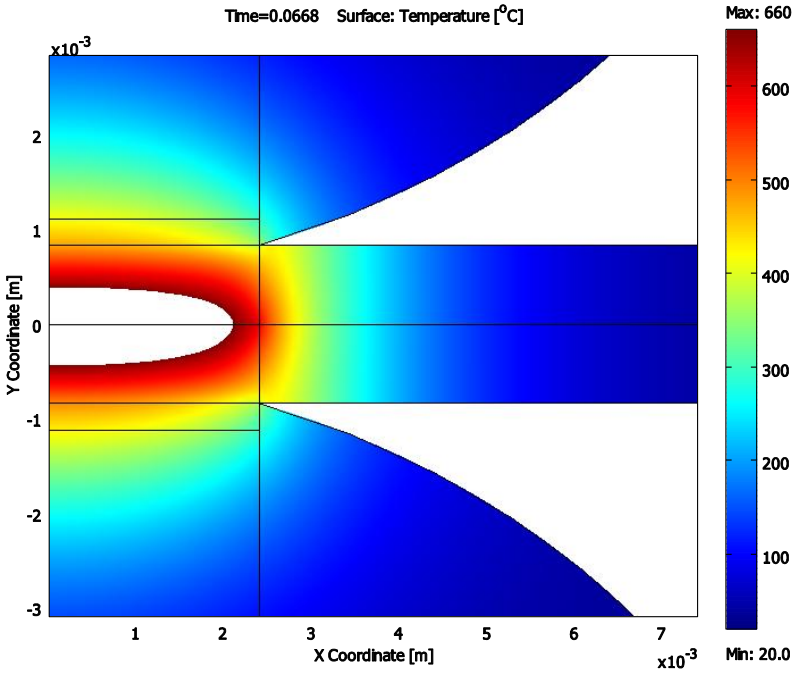

Figure II-17. Temperature distribution at the end of the fourth cycle.

For comparison purposes Figure II-18 summarizes the nugget growth during the spot welding of two 0.7 mm mild steel plates. The model was prepared and described in [20]. The simulated welding schedule consists of 10 welding cycles with a current of 8.2 KA. Figure II-18 clearly shows how the nugget growth dynamics for steel are completely different than the dynamics on aluminum. On steel, the nugget starts forming on the second half of the welding cycle. The model revealed that melting started on the beginning of the seventh cycle. The nugget size at the end of the ninth cycle shown in Figure II-18C has 0.46 mm of height and 3.6 mm of diameter. Through the following cycle the nugget continues growing until achieving a maximum size of 0.6 mm of height and 4 mm of diameter at the end of the 10^{th} cycle.

The temperature distributions across the *y* coordinate at the center of the nugget were obtained at different welding times for both models. For the aluminum weld a temperature distribution was obtained every 0.8 ms and for steel every 2 ms. Figure II-19 shows the temperature distributions for the aluminum weld. Figure II-19A shows all the temperature distributions in a single plot and the image shown in Figure II-19B was formed taking into consideration the time when the temperature distribution was acquired. Each column on the image corresponds to the temperature distribution on a particular welding time. The color on each pixel corresponds to the temperature value. Figure II-20 shows the temperature distributions for the steel weld.

By observing and comparing Figure II-19 and Figure II-20 one can notice the huge differences between the steel and aluminum spot welding process.

On steel, (Figure II-20) the temperature starts increasing from the center of the plates at a constant rate. As welding time progresses the temperature increases as well

until melting occurs at the 110 ms mark (Figure II-20B). After melting the nugget height starts to augment and the temperature on the liquid region increases at a higher rate than the solid part. This can be seen as the black region that appears on Figure II-20B after the 130 ms mark.

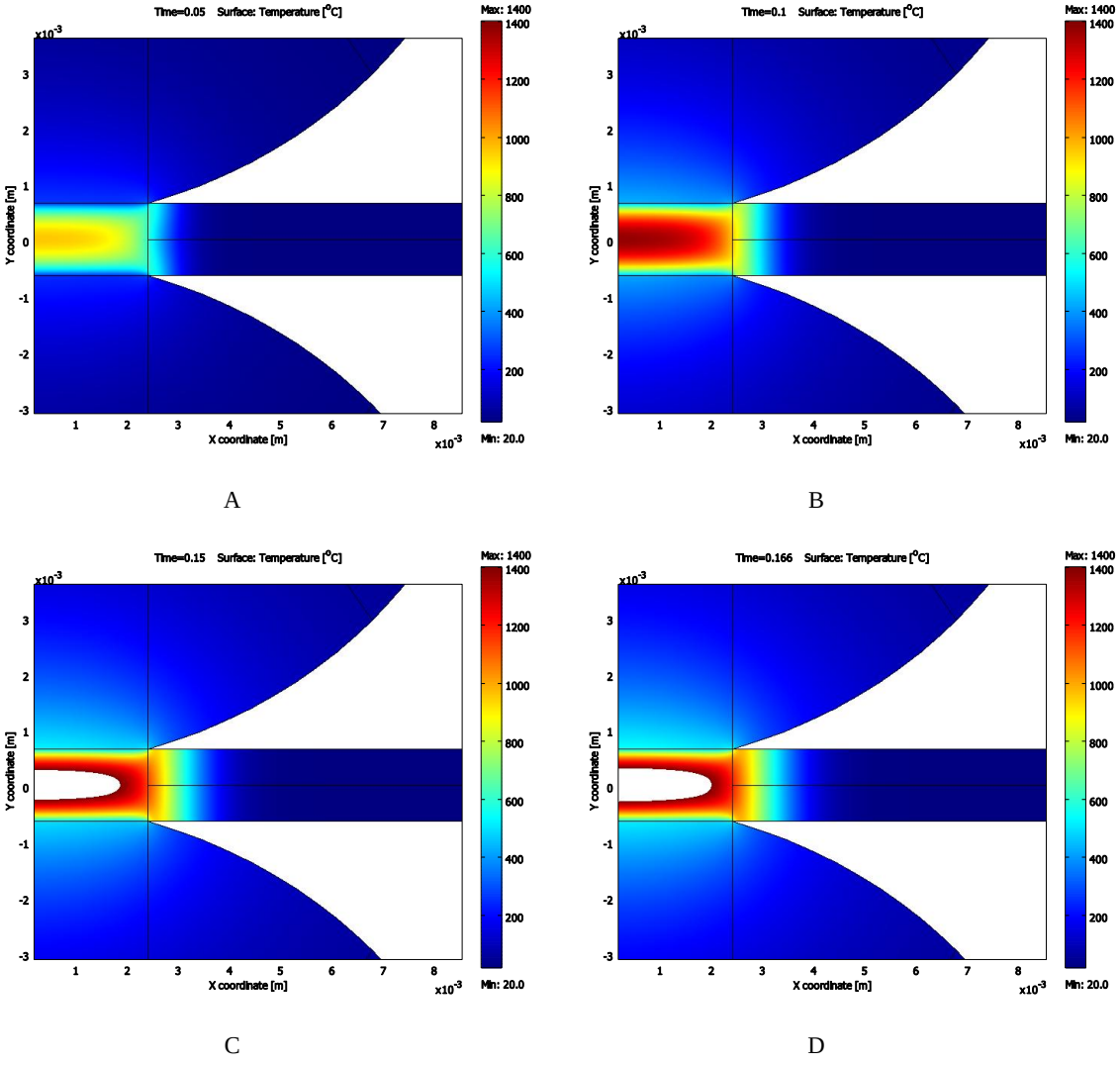

Figure II-18. Temperature distributions in a steel weld. A- 3rd cycle. B- 6th cycle. C- 9th cycle. D- 10th cycle. Results from model presented in [20]

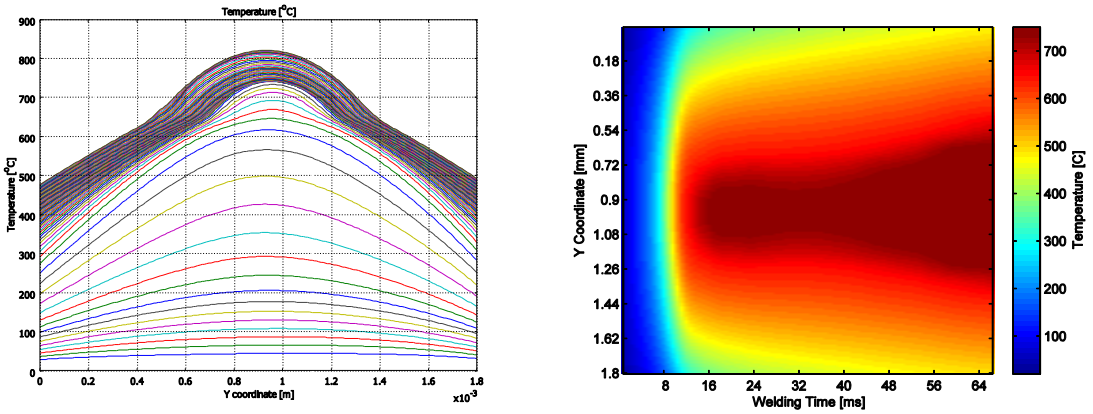

A B

Figure II-19. Aluminum temperature distributions acquired every 0.8 ms. A- Time independent plot. B- Time dependant map.

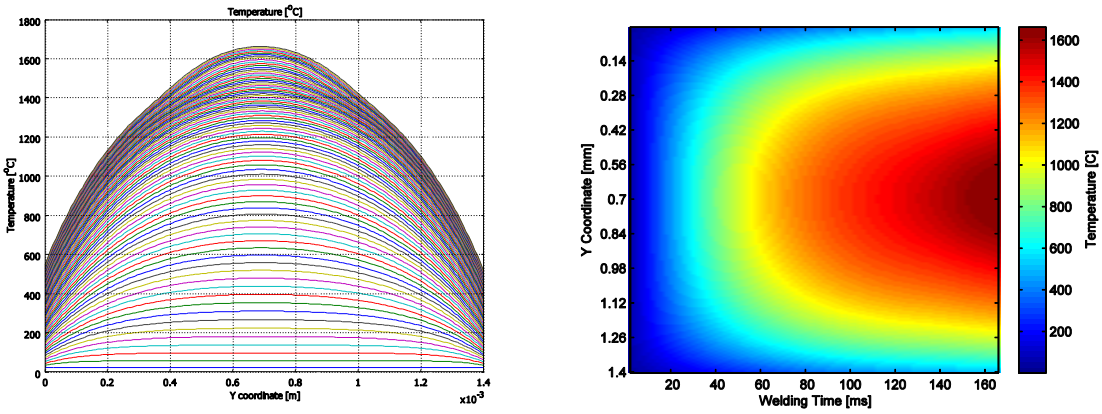

A B

Figure II-20. Steel temperature distributions acquired every 2 ms. A- Time independent plot. B- Time dependant map. Results from model presented in [20]

For aluminum (Figure II-19) the temperature starts increasing from the center of the plates as well, although at a much accelerated rate. Melting starts after 16 ms (Figure II-19B) 1/4 of the welding time compared to 3/4 on steel. Changes on nugget height and temperature in the liquid region are not as pronounced as in steel. Therefore, the temperature distribution remains relatively constant on the second half of the welding process.

Figure II-21A and Figure II-21B show the average and maximum temperature for each temperature distribution of the aluminum and steel model respectively. The curves clearly show the behavior already described where the temperature changes on aluminum are much higher in the first ms of the welding process and the changes on steel are gradual and constant during the whole welding process.

The differences between temperature distributions arise from the electric resistance dynamics on both materials. In contrast to aluminum, the contact resistance between the steel plates is considerably lower compared to the bulk resistivity [25-27]. In addition, the temperature dependence of bulk resistivity shows a higher increase rate on steel [24]. It was previously explained that the main heat contributor for aluminum is contact resistance and that this resistance is present only before melting (Figure II-10). As a result, the temperature distribution on aluminum (Figure II-21A) shows an accelerated increase on the first milliseconds of the process, produced by the influence of contact resistance. This is followed by stabilization and a slight increase of temperature on the second half of the welding cycle, caused by bulk resistivity.

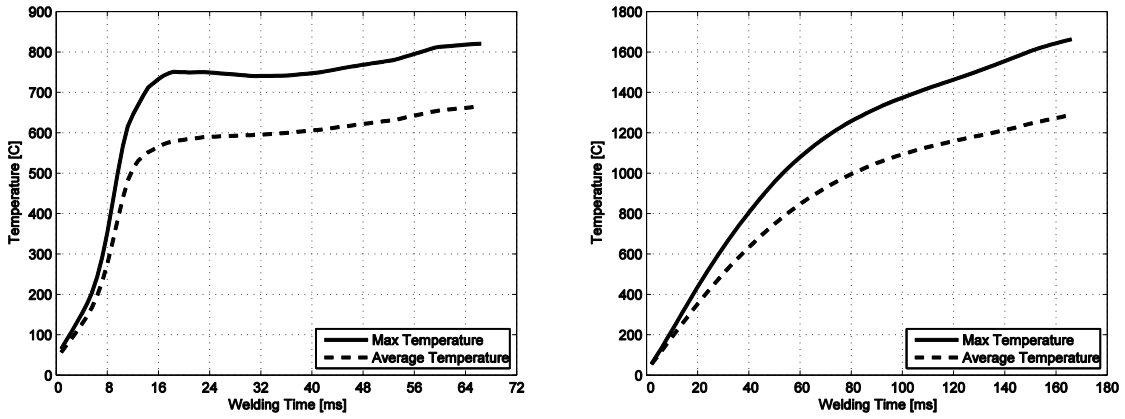

A B

Figure II-21. Maximum and average temperatures. A- Aluminum. B- Steel

Sound Propagation through the Aluminum Spot Welds

In the previous section the transient temperature distributions in the aluminum spot weld were obtained and compared to steel. It is possible to use this information to calculate the material property changes such as the gradients on the mass density and elastic constants. These gradients will dictate the acoustic wave propagation through the layered structure. This section of the dissertation presents a finite difference 1D wave propagation model through heterogeneous media. The objective of the model is to study the differences between the wave propagation through aluminum and steel spot welds and determine if the reflected signal can be used for the weld quality determination on aluminum.

The equation shown in Equation II-3 is the governing equation for the wave propagation model. This equation, derived by Chertov in [28], differs from the 1D wave equation by an extra term which is responsible for the coordinate dependence $f(x)$ of the elastic constants. The equation was derived based on the assumptions that the solid-liquid interfaces are parallel to the other interfaces and hence wave propagation is perpendicular in every interface. Also it is assumed that the main beam of the signal is well concentrated around the central axis. Based on previous research [28] it is known that these assumptions hold and the one-dimensional model provides a reliable picture of wave propagation in the setup. The governing equation allows the description of vibrations in heterogeneous media having arbitrary elastic properties and density profiles $\rho(x)$. These profiles are caused by the temperature changes caused during welding and are time variant. However, their rate of change is relatively small compared to the time of

wave propagation. Therefore, it is possible to consider the temperature distribution as stationary during the period the wave passes through [28].

$$\frac{\partial f(x)}{\partial x}\frac{\partial u}{\partial x} + f(x)\frac{\partial^2 u}{\partial x^2} = \rho(x)\frac{\partial^2 u}{\partial t^2} \qquad \textbf{Equation II-3}$$

The finite difference formulation of Equation II-3 using central differences is shown in Equation II-4. By grouping common factors and solving for u_i^{n+1} we obtained Equation II-5. This equation takes into consideration the density and elastic properties on each element i on the geometry and allows the calculation of the displacement u at time step $(n+1)$ from the time steps (n) and $(n-1)$.

$$\frac{f_{i+1}^n - f_{i-1}^n}{2\Delta x}.\frac{u_{i+1}^n - u_{i-1}^n}{2\Delta x} + f_i^n.\frac{u_{i+1}^n - 2u_i^n + u_{i-1}^n}{\Delta x^2} = \rho_i^n.\frac{u_i^{n+1} - 2u_i^n + u_i^{n-1}}{\Delta t^2} \qquad \textbf{Equation II-4}$$

$$u_i^{n+1} = ru_{i-1}^n\left(\frac{f_{i-1}^n - f_{i+1}^n}{4} + f_i^n\right) + ru_{i+1}^n\left(\frac{f_{i+1}^n - f_{i-1}^n}{4} - f_i^n\right) + 2(1-r)u_i^n - u_i^{n-1} \qquad \textbf{Equation II-5}$$

$$r = \frac{\Delta t^2}{\rho_i^n \Delta x^2}$$

The temperature dependence of material properties such as velocity, density and young modulus were obtained from different sources. In the previous section in Figure II-8, the temperature dependence of the aluminum density is presented. Chan et al in [29] and Weaver et al [30] performed measurements of the sound velocity in aluminum at different temperatures. The measurements showed different linear behavior when the temperature was lower than the melting point and after melting. Figure II-22 shows the

linearization of such measurements. Finally using density (ρ) and sound velocity (c), the temperature dependence of the young modulus E can be calculated using Equation II-6.

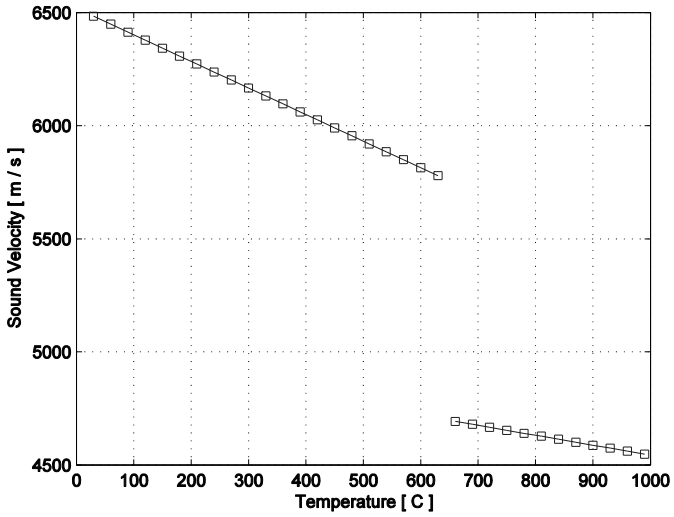

Figure II-22 - Temperature dependence of aluminum sound velocity. Measurements from [29].

$$c = \sqrt{\frac{E}{\rho}} \qquad \textbf{Equation II-6}$$

Figure II-23A and Figure II-24A show the temperature distributions in half of the setup after 2 welding cycles and at the end of welding respectively. To improve the temperature plot only 0.3 mm of the copper cap are shown in the figure. For each temperature distribution there is a corresponding sound velocity distribution. Figure II-23B and Figure II-24B show the velocity distributions for each temperature profile. From the figures it is noticeable that there is an abrupt change on velocity not only in the different layers of the setup (copper and aluminum) but also between the solid and liquid region of the aluminum plate.

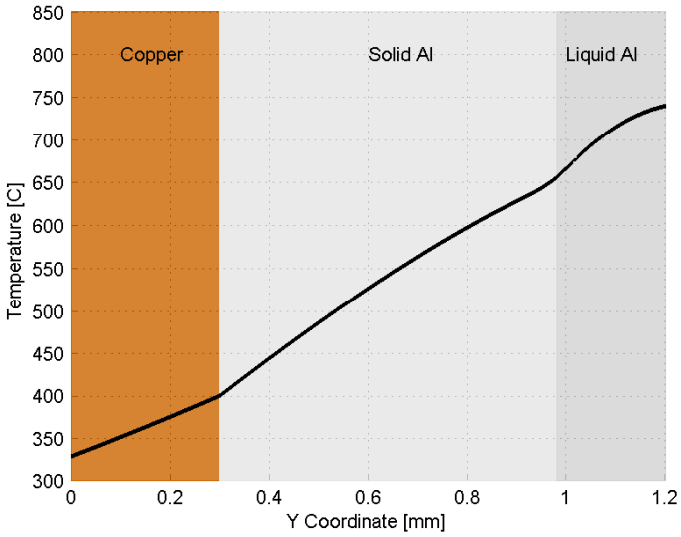

A

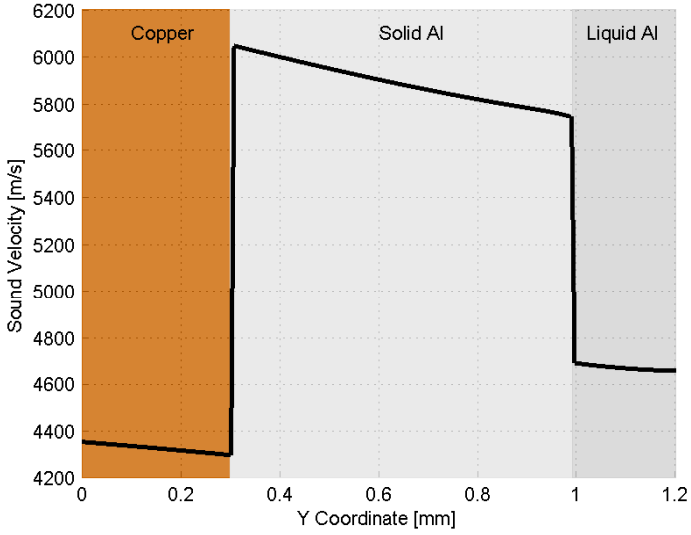

B

Figure II-23 -A- Temperature distribution. B- Sound velocity distribution after 2 welding cycles

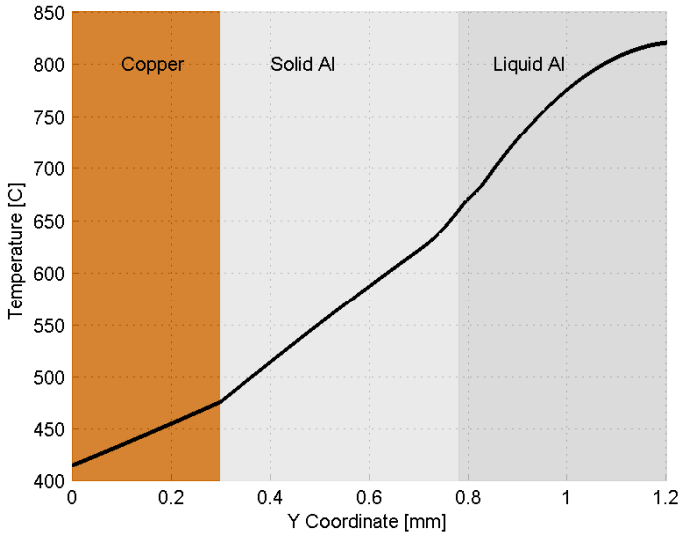

A

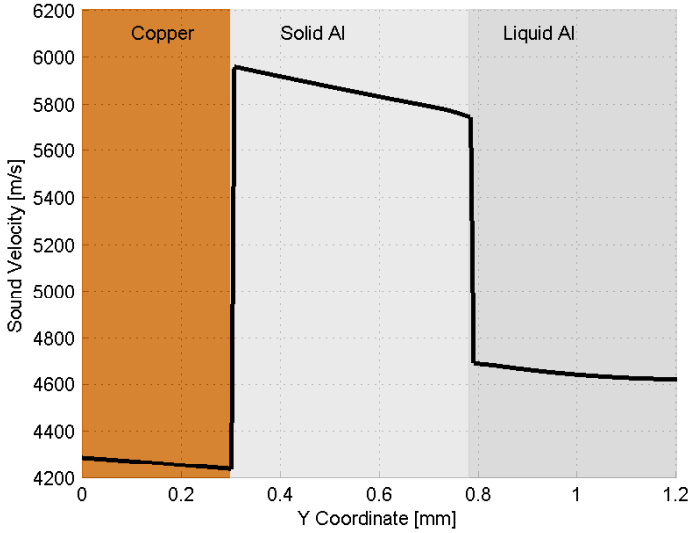

B

Figure II-24 – A - Temperature distribution. B- Sound velocity distribution at the end of welding.

Figure II-25 shows the wave pressure dynamics in the different media at the end of the welding process. Note that a column of water was added to the geometry. The water temperature was assumed constant (26 ºC). The wave starts to move from the water layer and experiences multiple reflections on the different interfaces. The arrow on the top or bottom of each wave represents the propagation direction. On each boundary, the reflection and transmission coefficients for pressure are shown. These coefficients were calculated using the equations shown in Equation II-7, where Z_1 and Z_2 represent the acoustic impedance of the media.

$$R = \frac{Z_2 - Z_1}{Z_2 + Z_1} \qquad T = \frac{2Z_2}{Z_1 + Z_2}$$ **Equation II-7**

Figure II-25 summarizes the wave propagation through the different media. The wave travels from the water (Figure II-25A) to the copper layer with a transmission coefficient of 1.93 (Figure II-25B). Then, at the Cu-Al the wave is transmitted with a coefficient of 1.18 and reflected with a coefficient of 0.21 (Figure II-25C), this reflection is the first reflection (reflection number 1) gated on the M-Scan previously shown (Figure II-7). The drastic changes in properties between solid and liquid aluminum provoke an extra reflection at the melting boundary. In this interface the wave is transmitted with a coefficient of 0.84 and reflected with a coefficient of -0.15 (Figure II-25D). The negative sign on the reflection coefficient indicates that phase inversion takes place. This occurs when the wave is travelling from a low density (high wave speed) region towards a high density (low wave speed) region ($Z_2<Z_1$), which is the case between solid and liquid aluminum.

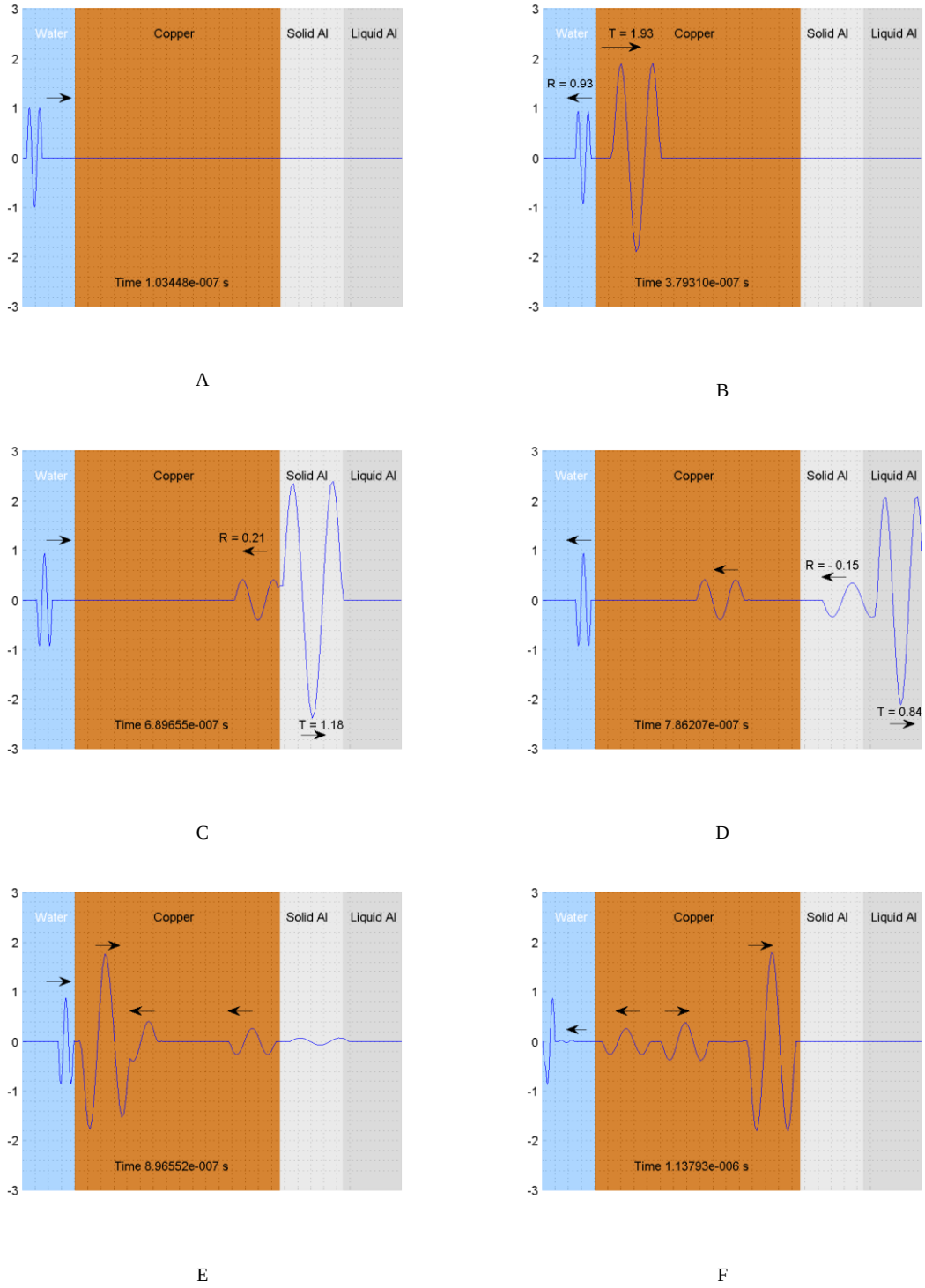

Figure II-25 - Wave propagation through the different layers. (Subscript indicates the sequence of propagation).

Figure II-25E shows the wave interaction on the setup occurred after 0.8 μs. On the left area of the copper region one can see 2 waves superimposed on each other corresponding to an echo transmitted from the water to the copper and the reflection occurred at the Cu-Al interface. After 1.13 μs the Cu-Al reflection is transmitted from the copper back to the water, this wave can be seen on the right figure of Figure II-25F on the right side of the water region. Finally, this weak reflection returns to the piezoelectric transducer and it's digitized by the system to become reflection number 1 on the M-Scan.

It was previously mentioned that the TOF at the end of welding is used to estimate the nugget diameter on steel spot welds. To corroborate this fact on aluminum, simulated TOF curves were calculated. Since the space is discretized, the total TOF at time n can be calculated as the summation of the TOF through every grid node. To achieve this task the sound velocity on each grid point can be calculated based on its temperature and the temperature dependence of sound velocity shown in Figure II-22. The temperature between grids was assumed as the average between both nodes. Thermal expansion on each grid node has to be considered on the TOF calculations as well. The temperature dependence of the thermal linear expansion coefficient ($\alpha_i(T) = L/\Delta L$) was taken from [13]. Equation II-8 describes the calculations performed on each time step to determine the TOF (t_i^n), where N denotes the number of nodes, d_0 denotes the initial distance between nodes and d_i denotes the updated distance after considering thermal expansion.

$$t_i^n = \sum_{i=1}^{N-1} \frac{d_i}{\frac{c_{i(T)}+c_{i+1(T)}}{2}}, \quad d_i = d_0(1+\alpha_i(T)) \qquad \textbf{Equation II-8}$$

Figure II-26 shows the TOF curves for aluminum spot welds with a 4.5 and 2.5 mm diameter nugget. The curves follow the temperature dynamics shown on Figure II-19. The moment of melting can be observed for the two curves as the drastic change of slope shown at the 12ms welding time for the 4.5 mm nugget and 24 ms welding time for the 2.5 mm nugget. An important thing to notice is the small variation of the TOF at the end of welding between the two curves (30 ns) this change represents a 4.1% variation between an acceptable and a non acceptable weld, opposite to steel where the variation of time of flight is 20% [5].

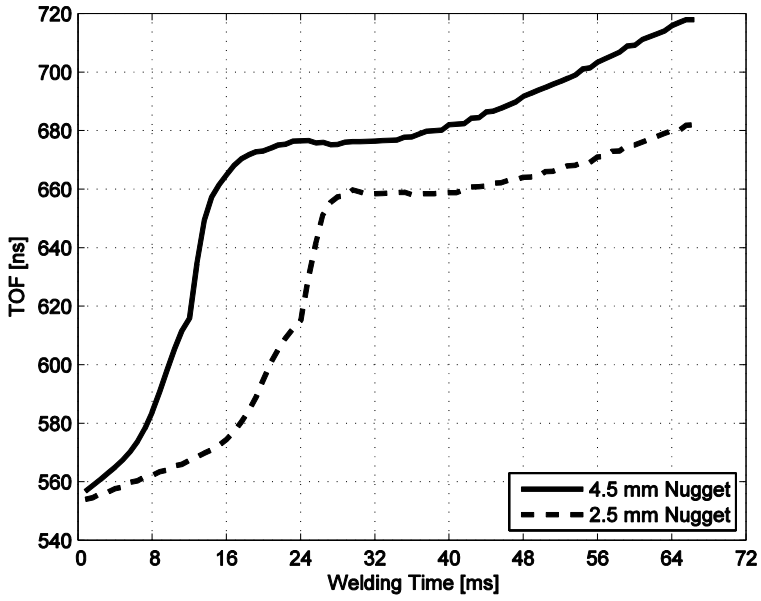

Figure II-26 - TOF curves for aluminum spot welds with a 4.5 and 2.5 mm diameter nugget

Problem Statement

This chapter presented a deep analysis of the differences between the aluminum and steel spot welding processes and the acoustic wave propagation through such welds. The limitations and challenges to implement the RIWA system on aluminum stand out on this analysis.

The high thermal conductivity and the short welding times used on the spot welding process of aluminum required a 0.1 ms time step on the welding model in order to achieve convergence. This time step is 10 times lower compared to the 1 ms step used on the steel model. This fact suggests that experimentally, higher pulse repetition frequencies (PRF) are required to ultrasonically monitor the aluminum spot welding process. The lack of information observed on the first M-Scans acquired (Figure II-7) concur with this fact. This problem was resolved in the early stages of the research by working closely with the original hardware research and design team that developed the RIWA system [31]. The acquisition board was updated significantly by this group in order to achieve A-Scan intervals (1/PRF) in the order of fractions of milliseconds.

The updated hardware brought much more information to the ultrasonic data acquired with it. Figure II-27 shows one of the firsts M-Scan acquired with new board. The A-Scan interval used was 0.7 ms per A-Scan. In the figure can be seen that the dynamics of the back wall reflection are much more detailed than the previous M-scans, also the reflections corresponding to the top and bottom of the liquid nugget are visible. Chapter 4 will describe the different features observed on the M-Scans in detail.

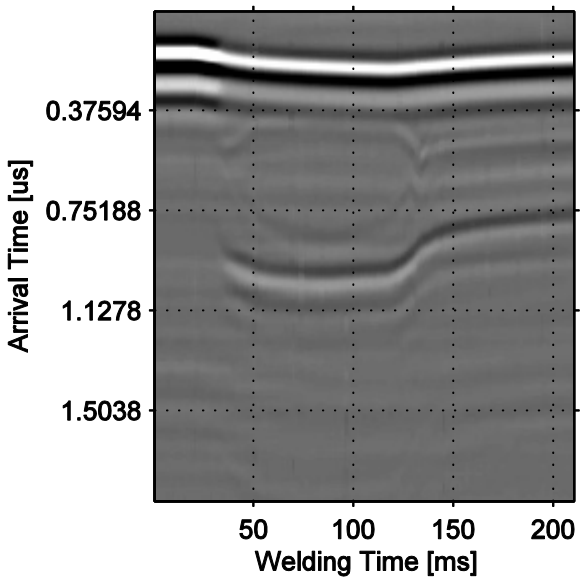

Figure II-27 - M-Scan acquired with 0.7 A-scan Period

The second problem detected on the analysis was that the main parameter used to determine the quality on steel spot welds (TOF at the end of welding) is not applicable to aluminum. To confirm this finding experimentally, a linear correlation between TOF at the end of welding and nugget diameter was attempted for aluminum using the new acquisition board. Note that the experimentation was done on a 2T stack up of 0.9 and 1.9 mm. Figure II-28 shows the result of the experiment. TOF measurements suffer from an error of 2-3% coming mainly from the peak detection technique used. The correlation shows an R^2 value of 0.54, this fact, clearly shows that TOF is not a good ultrasound parameter to estimate nugget diameter on aluminum. Therefore, another parameter useful to estimate nugget diameter in aluminum should be extracted from the ultrasonic M-Scan.

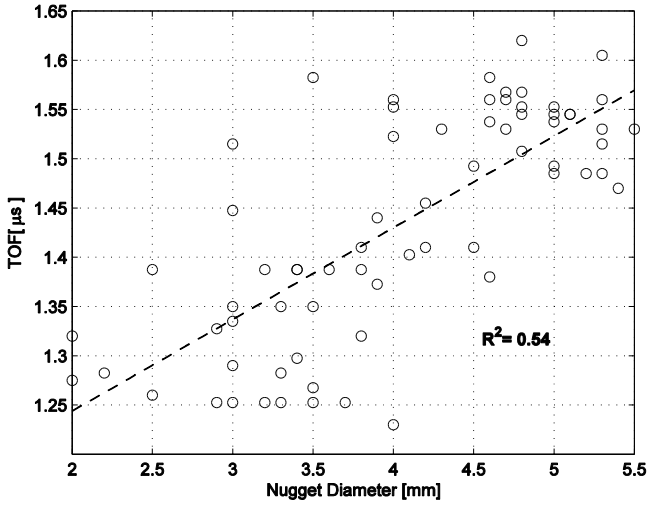

Figure II-28 - TOF and Nugget Diameter Linear Correlation

During the acquisition of the experimental data shown in Figure II-28, two more challenges were encountered, electrode overheating and electrode deterioration. It has been already explained that aluminum spot welding suffers from heavy electrode deterioration caused by the high contact resistance and hence heat generation at the copper-aluminum interface. This localized heat which is removed by the cooling water running inside the electrode causes rapid electrode deterioration. Occasionally, the heat generated on the electrode is enough to elevate the water temperature above the boiling point. When this occurs, the acoustic wave generated by the transducer can no longer be propagated to the copper cap.

Electrode deterioration by itself is another issue. As degradation progresses, pits are formed on the copper caps. This affects the ultrasonic M-Scans by blocking the sound that is propagated from the copper cap to the aluminum plates. Periodic deterioration can be observed as the gradual disappearance of the back wall reflection. Figure II-29 shows this gradual disappearance. In order to study electrode deterioration in detail and find a

way to overcome it, chapter 3 will present an experimental characterization of the aluminum RSW process, where several cap life time studies were performed.

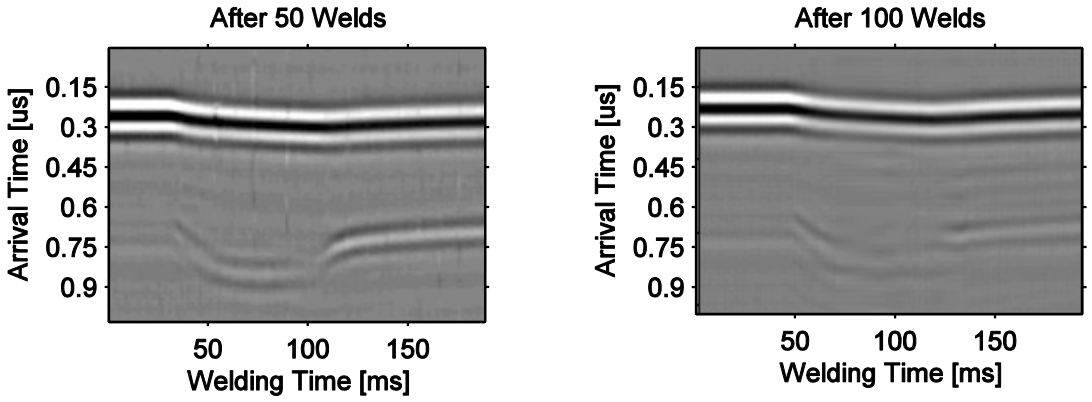

Figure II-29 - Signal disappearance

References

1. *In-Process Ultrasound NDE of Resistance Spot Welds,* by A.M. Chertov, A.C. Karloff, **W. Perez Regalado**, A. Lui, R. Gr. Maev. Journal of the British Institute of Non-Destructive Testing 2012. Vol. 54, No. 5, pp. 257-261.
2. *Real Time Ultrasonic System for Resistance Spot Weld Inspection. Integration in Assembly Line*, by A.M. Chertov, R. Gr. Maev, **W. Perez Regalado,** A.C. Karloff. Proceedings Canadian NDT Conference (CINDE), 2012. Paper 3-5.
3. Real Time Ultrasonic Aluminum Spot Weld Monitoring System, by **W. Perez Regalado**, A.M. Chertov, R.Gr. Maev. Proceedings of the Review of Progress in Quantitative NDE 2009 (QNDE). Vol. 1211, No. 1, pp. 1152-1157.

4. *Lokalisierung der Erstarrungsfront beim Stranggieben von Stahl*, by Von W. Kurz and B. Lux. 1959. Vol. 5, pp. 123-130.
5. *Development of the New Physical Method for Real Time Spot Weld Quality Evaluation Using Ultrasound*, by A.M Chertov. PhD dissertation 2007, University of Windsor.
6. *Specification for Automotive Weld Quality – Resistance Spot Welding of Steel.* American Welding Society Standard AWS D8.1M:2007
7. *Monitoring of Pulsed Ultrasonic Waves' Interaction with Metal Continuously Heated to the Melting Point*, by R.Gr. Maev. Review of Progress in Quantitative Nondestructive Evaluation, Ames, Iowa, USA, 2001. Vol. 20B, pp. 1517-1525.
8. *Method of Quantitative Evaluation of Elastic Properties of Metal at Elevated Temperatures*, by A. Pthchelinsev and R.Gr. Maev. Review of Progress in Quantitative Nondestructive Evaluation, Ames, Iowa, USA, 2001. Vol. 20B, pp. 1509-1517.
9. *Transducer Built Into an Electrode* by R.Gr. Maev, A. Ptchelintsev and J. Mann. US Patent Number 6,297,467, Filed: April 1, 1999, Issued: October 2, 2001.
10. *Real Time Ultrasonic Inspection System for Resistance Spot Welds. Case Study in Production Environment*, by R.Gr. Maev, A.M. Chertov, **W. Perez Regalado**, A.C. Karloff, A. Tchipilko, P. Lichaa, D. Clement and T. Phan. Proceedings of the XV Sheet Metal Welding Conference, American Welding Society, 2012. Paper 2-5.

11. *Coefficients for Calculating Thermodynamic and Transport Properties of Individual Species,* by B.J. McBride, S. Gordon and M.A. Reno. NASA Technical Paper 3287 (1993).
12. *Use of Thermal Expansion Measurements to Detect Lattice Vacancies near the Melting Point of Pure Lead and Aluminum* , by R. Feder, A.S. Norwick, Physical Review 1958. Vol. 109, No. 6, pp. 1959-1963.
13. *The Thermal Expansion of Pure Metals: Copper, Gold, Aluminum, Nickel, and Iron,* by F.C. Nix and D. MacNair, Physical Review, 1941. Vol. 60, No. 8, pp. 597-605.
14. *Thermal Expansion of Some Crystals with the Diamond Structure*, by D.F. Gibbons, Physical Review, 1958. Vol. 112, No. 1, pp. 136-140.
15. *Portable data-acquisition and analysis system for thermal conductivity measurements*, by W.D. Drotning. Review of Scientific Instruments, 1984. Vol. 55, No. 11, pp. 1804-1816.
16. *Electrical Resistivity of Aluminum and Manganese*, by P.D. Desai, H.M. James and C.Y. Ho, J. Phys. Ref. Data, 1984. Vol. 13, No. 4, pp. 1131-1172.
17. *Thermal Conductivity of the Elements*, by C.Y. Ho, R.W. Powell and P.E. Liley, J Phys. Chem. Ref. Data, 1972. Vol. 1, No. 2, pp. I.11-I.68.
18. *Fundamental Study of Contact Resistance Behavior in RSW Aluminum*, by M.A Ta-Chien, Ph.D. Dissertation 2003, The Ohio State University.
19. *Thin-Film Resistance Model*, COMSOL Multiphysics Modelling Guide, Chapter 13. October 2007.

20. *New developments for in situ ultrasonic measurement of transient temperature distributions at the tip of a copper resistance spot weld electrode,* by A.C. Karloff, A. M. Chertov, J. Kocimski, P. Kustron, R. Gr. Maev. Ultrasonics, IEEE Symposium - IUS 2010. pp. 1424-1427.
21. *Temperatures in spot welding,* by J.S Greenwood. British Welding Journal 1961. Vol. 8, No. 6, pp. 316-322.
22. *The finite element modeling of the resistance welding process,* by H.A. Nied. Welding Journal 1984. Vol. 63, No. 4, paper 1-23.
23. *Electrode geometry in resistance spot welding*, by R. J. Bowers, C. D. Sorensen and T. W. Eagar. Welding Journal, 1990. Vol. 69, No. 2.
24. *Resistance Welding: Fundamentals and Applications*, by H. Zhang, J. Senkara Second Edition, CRC Press, 2011.
25. *Modeling dynamic electrical resistance during resistance spot welding,* by S.C. Wang and P.S. Wei. Journal of Heat Transfer, 2001. Vol. 123, No. 3, pp. 576-585.
26. *Optimization and Validation of a model to predict the Spot Weldability Parameter Lobes for Aluminum Automotive Body Sheet*, by D. J. Browne, C. J. Newton, and D. Boomer. Proc. Advanced Technologies & Processes (IBEC ’95) 1995, pp. 100-106.
27. *Spot welding of aluminum sheet: a statistical approach to measure the influence of different surfaces*, by M. Thornton, C. Newton, B. Keay, and T. Evans. Proc. Advanced Technologies & Processes (IBEC ’96), 1996, pp. 58-66.

28. *Experimental study and theoretical modelling of ultrasonic wave propagation in resistance spot welds*, by A.M. Chertov. M.Sc thesis, University of Windsor, 2003.
29. *Measurements of the Velocity of Sound in Liquid Aluminum to 1800 K*, by J.P. Chan J. Proc. 5th Symposium on Thermo Physical Properties,1970, pp.541–563.
30. *Temperature Dependence of Ultrasonic Diffuse Fields, Implications for the Measurement of Stress*, by R. Weaver and O. Lobkis. Proc Review of Progress in Quantitative Non-destructive Testing, 2001. Vol. 557, pp. 1480- 1488.
31. *Two-Channel Measuring Acoustic Microscope*, by S. Titov, R.Maev, A.Bogachenkov. Journ. of Scientific Tool and Experimental Methods, 2000. Vol. 43, No.2, pp. 275-278.

CHAPTER III

EXPERIMENTAL CHARACTERIZATION OF THE ALUMINUM RSW PROCESS

This chapter focuses on the aluminum spot welding process and the different variables that affect weld quality specially electrode deterioration. The majority of the data presented in this chapter was prepared for one of our industrial partners based on our collaborative research project. Therefore, the material characteristics were chosen based on their requirements and the variables of the experimentation were selected in order to reduce changes on their facilities and/or processes.

The first stage of the chapter concentrates in determining the optimum welding schedule for the selected material and stack up combination. Then a series of electrode lifetime experiments were performed. Special attention was put on the effect that plate orientation and welding gun polarity has on electrode life. Finally, the last section of the chapter includes a novel approach proposed in order to reduce the current used to weld aluminum diminishing electrode deterioration.

Each weld produced on this chapter was ultrasonically monitored. The analysis of the M-Scans acquired is described in chapter 4.

Experimental Procedure

The material selected for this study was 0.9 mm and 1.9 mm Al6022 aluminum alloy sheets with the properties shown in Table III-1. The surface of the aluminum was not treated. The electrodes were 4.8 mm face commercially available B-Nose C15000 Copper (99.8% Cu, 0.15% Zr) caps. The plates were welded using an ABB robotic arm with an X-type welding servo gun and MFDC welding equipment.

Property (Units)	Value
Electrical Resistivity ρ (10 $^{-8}$ Ω m)	3.723
Yield Strength (MPa)	122
Tensile Strength (MPa)	250
Elongation (%)	27

Table III-1 - AA6022 properties.

Using the welding schedule listed on Table III-2, electrode life tests were conducted on the 0.9 mm – 1.9 mm stack up. Welding coupons with the geometry shown in Figure III-1 were designed in order to be easily fixed in our facilities and the locations of the welds were chosen to maximize the number of welds per coupon while avoiding the shunting effect. Neither current stepping nor force stepping were used in the experiment. To determine the electrode face growth as a function of weld number, no cap dressing was applied either. One coupon was destroyed every 100 welds in order to

determine the average nugget diameter. Also on the same interval, carbon imprints were taken of both electrodes. Once the average nugget diameter dropped to the minimum acceptable size (4 mm), 50 more welds were produced, if the nugget diameter was still below the acceptable range, the test was concluded. Three sets of experiments were conducted, on two of them the 1.9 mm plate was facing the positive (anode) electrode and on the third one the 0.9 mm plate was facing the anode.

Parameters (Units)	0.9mm – 1.9 mm	1.9 mm – 1.9 mm
Force (lbs)	800	950
Weld Time (60hz Cycles)	4	8
Current (KA)	26.5	31

Table III-2 - Welding schedules for the two stack ups used.

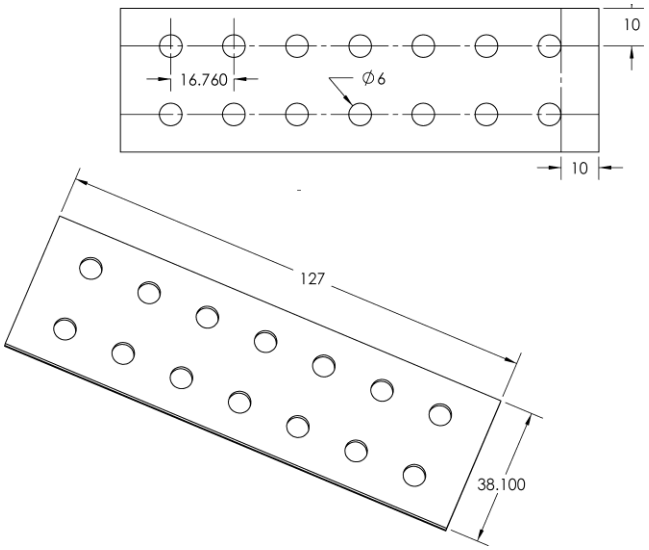

Figure III-1 - Welding coupon geometry. Dimensions in mm.

In order to assess the heat generated on each individual electrode, temperature measurements were carried using a Mikron MI-140 pyrometer. The electrode caps surface was painted with flat black high temperature paint. The emissivity on the pyrometer was adjusted and calibrated accordingly. Special attention was placed on the distance between the pyrometer and the electrode cap. To assure accurate measurements, the location of the pyrometer was chosen in order to achieve a focused measurement spot with a diameter of 1 mm. The measuring spot was on the outside face of the cap 1 mm away from the contact with the aluminum plates. Figure III-2 shows a photograph of the experimental set up and the location of the pyrometer relative to the welding gun. To isolate the effect of polarity in the electrode temperature during welding, a separate experiment was performed where the welding stack up was symmetrical. The welding schedule used is shown in Table III-2, the thickness chosen for the aluminum plates was 1.9mm.

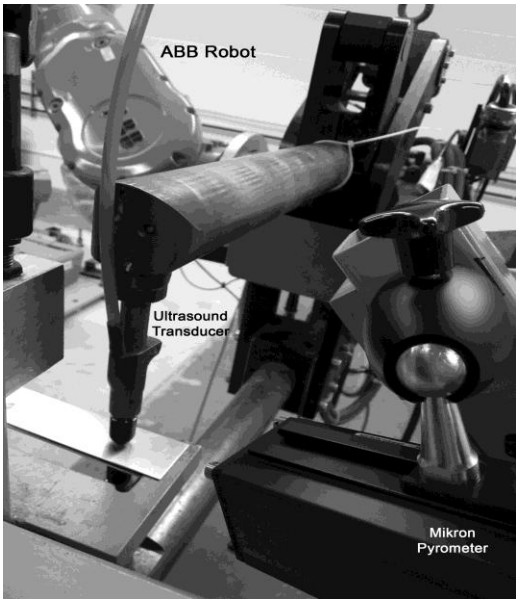

Figure III-2 - Experimental Setup.

Welding Lobes

In order to determine the welding lobes for the selected material combination, the minimum current I-Min to form the minimum nugget size (4mm) and the maximum current I-Max that will cause expulsion, were determined experimentally for three force ranges: 700,800 and 900 lbs. An initial current I-Start point was chosen for any given force- weld time combination. Force ranges and I-Start were chosen based on the recommendations of the Auburn University's Materials Processing Center for aluminum alloys on the series 5XXX.

Using I-Start, the given force and the given weld time, an aluminum coupon with 6 spot welds was produced; subsequently the nugget diameter was assessed by destructive means (peel test). Depending on the average nugget diameter, the current was increased or decreased 1 KA until I-Min was determined. Once I-Min was determined, the current was increase until I-Max was found by the presence of expulsion. The procedure was repeated for all the possible force – weld time combinations. Figure III-3 shows the welding lobes for different forces, and the optimum welding schedule found by calculating the centroid of the polygon formed with the perimeter of all the welding lobes. Table III-2 shows the optimum welding schedule (0.9mm-1.9mm).

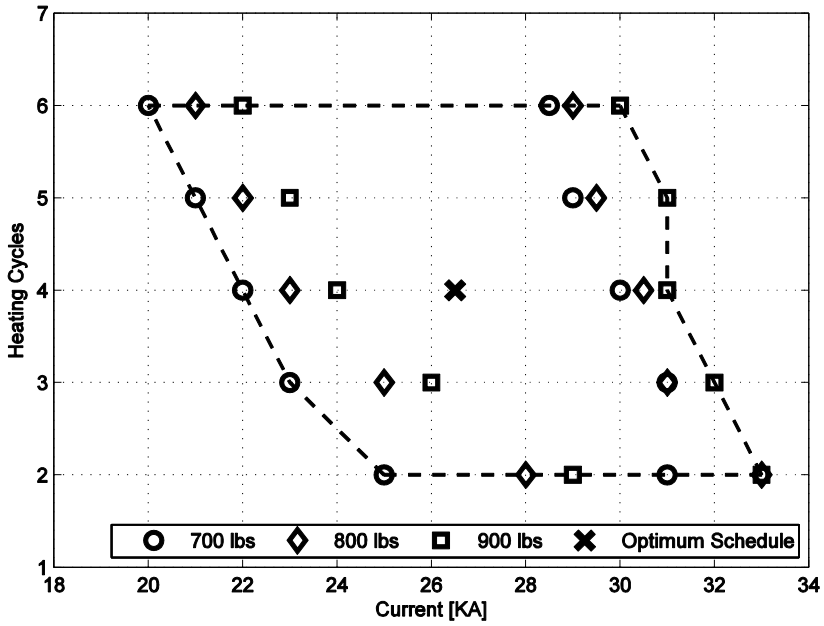

Figure III-3 - Welding lobes

Cap Degradation Study

The problem statement in Chapter 2 described that one of the difficulties to implement the RIWA system on aluminum is electrode deterioration. The significance of this is that the signal gradually disappears as the electrode deteriorates. A deeper understanding of the different stages of electrode deterioration is required in order to evaluate if such degradation can be overcome or to determine the limitations of the ultrasonic system. This is the main objective of the electrode deterioration experiments presented in this section. However, a second goal is to determine the effect that plate orientation (dissimilar thicknesses) and polarity has on the electrode cap life time.

Using the optimum welding schedule, and the experimental procedure explained in the previous section, cap lifetime studies were carried out under two different scenarios: 0.9 mm plate facing the anode (Case A) and 1.9 mm plate facing the anode (Case B). In order to study the repeatability of the results a third experiment was performed where the 1.9 mm plate was facing the anode (Case B2).

Figure III-4 shows, the carbon imprints of the anode and the cathode caps for the three cap lifetime experiments. The figure clearly shows the different stages of the electrode deterioration. The first indication of electrode deterioration was a change of color on the cap face to a dark gray. This change of color was attributed to aluminum pick up from the electrode. After 100 welds the first visual signs of pitting appeared in the carbon imprints on the anode side. These pits started on the periphery of the contact area for Case A and B2 and in the center of the cap for Case B. The pits grew until forming large cavities on the electrodes. For Case A the pits formed a ring in the periphery of the contact area and after 600 welds the pits started to move towards the center of the cap. However for Case B and B2 the pits shifted to the center of the electrode just after 400 welds.

Figure III-4 clearly shows that the deterioration is mainly present on the anode electrode; the reason for this phenomenon is known as the Peltier effect [1]. This effect describes the heat difference that occurs due to an electric voltage between two dissimilar metals junctions. The current flow through these junctions drives a transfer of heat from one junction to the other (temperature is decreased in one junction and increased on the other) determined by the direction of the current. In a typical RSW set up using DC, current flows only in one direction providing consistency to the Peltier effect throughout

the heating pulses [1] [2]. The temperature measurements described in the next section and shown in Figure III-7 demonstrate that the anode electrode junction (electrode-plate) increased its temperature and the cathode electrode reduced its temperature, confirming the Peltier effect. This resulted in a faster electrode degradation of the anode electrode compared to the cathode electrode as shown on the carbon imprints in Figure III-4.

Figure III-5 summarizes the cap lifetime results of the three cases; the end of the cap life (EOL) is marked for each case. The worst performances were obtained in Case B and B2 with a maximum number of 450 and 550 welds respectively. The variability of the nugget size during these experiments was very high and the minimum nugget size was achieved several times. The best results were achieved in Case A, with a maximum number of welds of 730, almost 300 welds more than Case B. For Case A, the Nugget sizes remained in the 4.6 - 4.4 mm range during the whole experiment before cap failure.

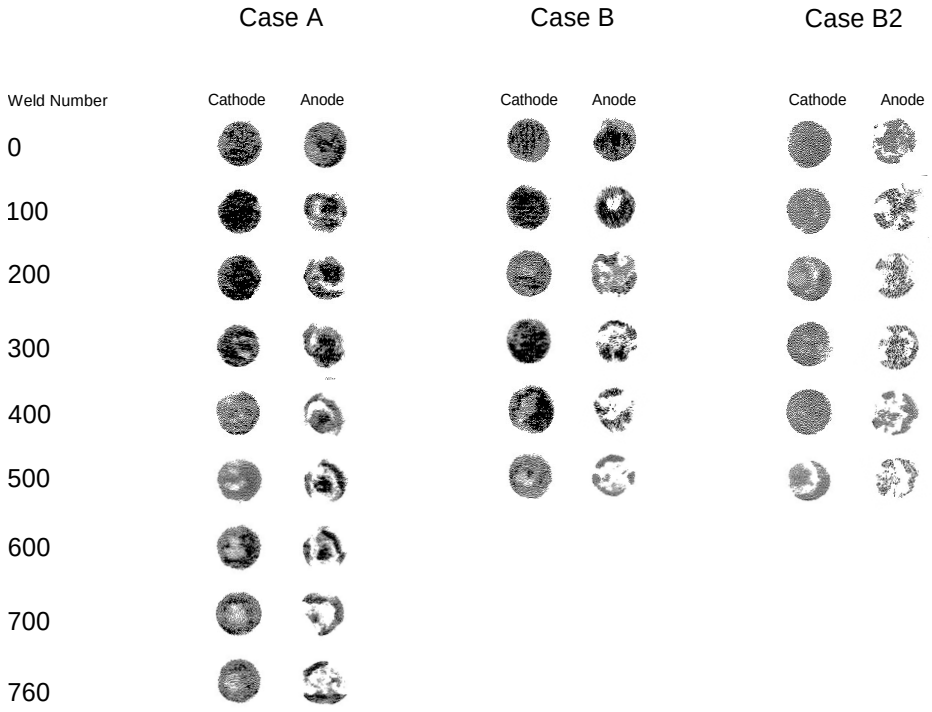

Figure III-4 - Carbon imprints for the three cap lifetime studies.

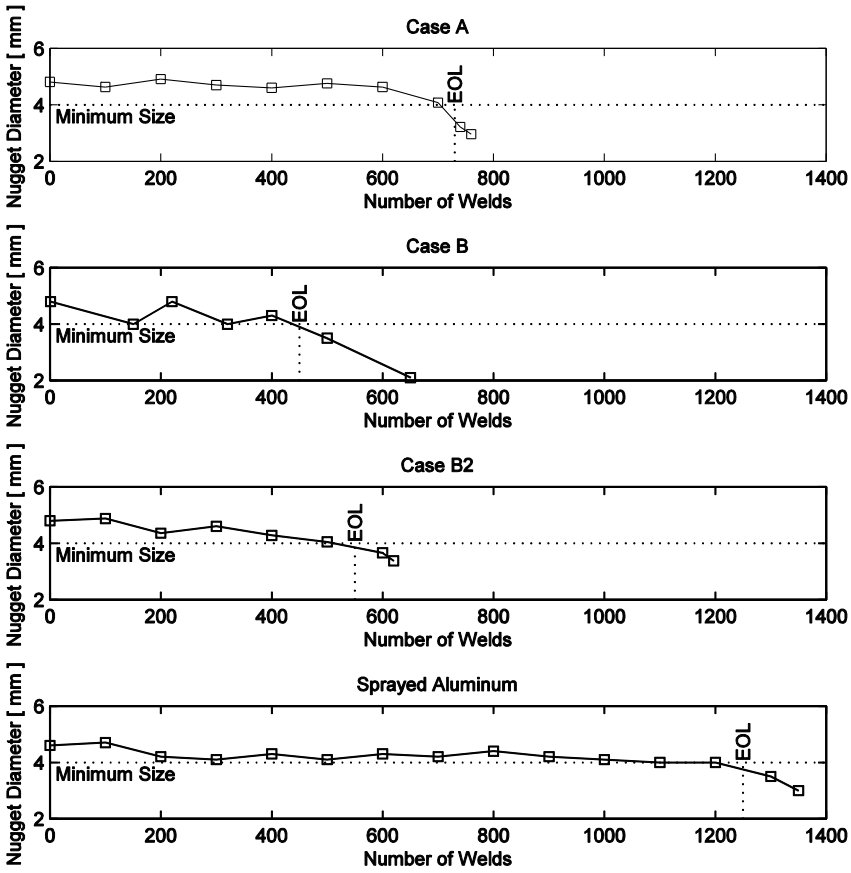

Figure III-5 - Cap lifetime results.

The face diameter was monitored throughout the experiments. Figure III-6, summarizes the cap growth on the anode electrode for the three cases. Note that the nugget diameter and face size measurements are susceptible to instrumentation error of ±0.02 mm. In Figure III-6 it is clearly seen how the face growth for Case A is considerably less compared with the other two cases. The anode cap grows at a rate of 0.1 mm per 100 welds, except near the end of the cap lifetime where it jumps to 0.7 mm per 100 welds. The jump in face growth matches the shift and growth of the pits in the center of the electrode. This can be attributed to the increase of heat generation at the caps produced by the increase of current density due to the reduction of the contact area

produced by the pitting. The face diameter during failure was 6.5 mm for the three experiments.

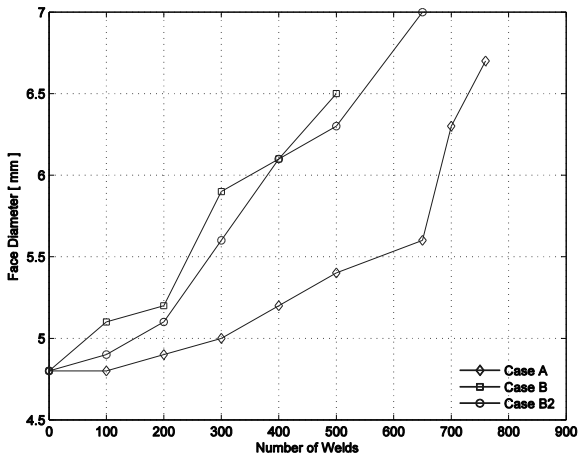

Figure III-6 - Anode cap face growth

Temperature Measurements

Figure III-7 shows the temperature dynamics of both electrodes during the welding of one sample in the symmetrical setup experiment (1.9mm-1.9mm). In the figure the bars indicate the instrument error of ±5°C. The beginning and end of the heating cycle are marked with dashed lines. The contact conditions were assumed symmetric and therefore any change of temperature between the electrodes during the heating cycle was attributed to the polarity and the Peltier effect. The figure clearly shows, how when the current stops flowing, the temperature of the anode electrode (120 °C) is much higher than the cathode electrode (70 °C). This observation confirms the huge effect that polarity has on the electrode degradation.

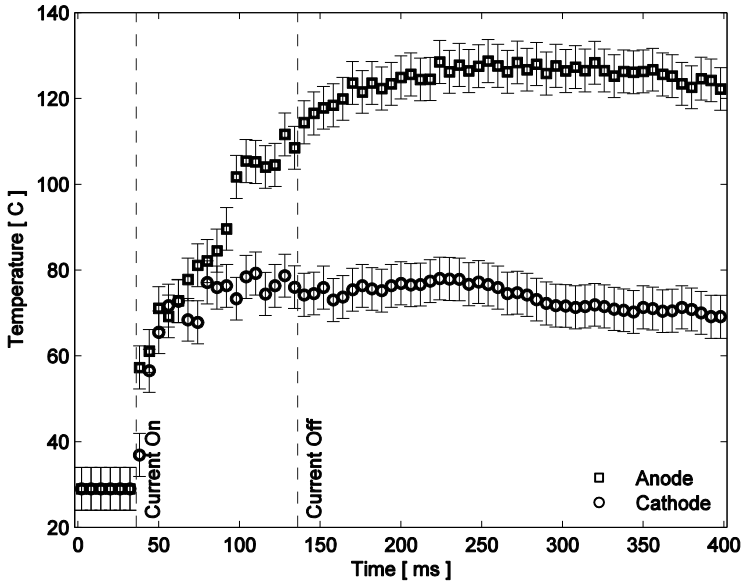

Figure III-7 - Temperature dynamics of the anode and cathode electrode during welding.

In order to study the effect of the plate orientation and polarity, temperature measurements on the anode electrode were done for the case A and case B cap lifetime experiments. Figure III-8 shows the temperature measurements of one sample of each case. The figure shows lower temperature values (75 °C) when compared to the results shown in Figure III-7 (120 °C), the reason for the reduction is the difference in current and welding time on the welding schedules used on each experiment. For case A the anode temperature measurements showed lower values. In Figure III-8 it is seen that the maximum temperature for case A is 65 °C compared to 75 °C for case B, this trend was observed in all the temperature measurements of the experiment.

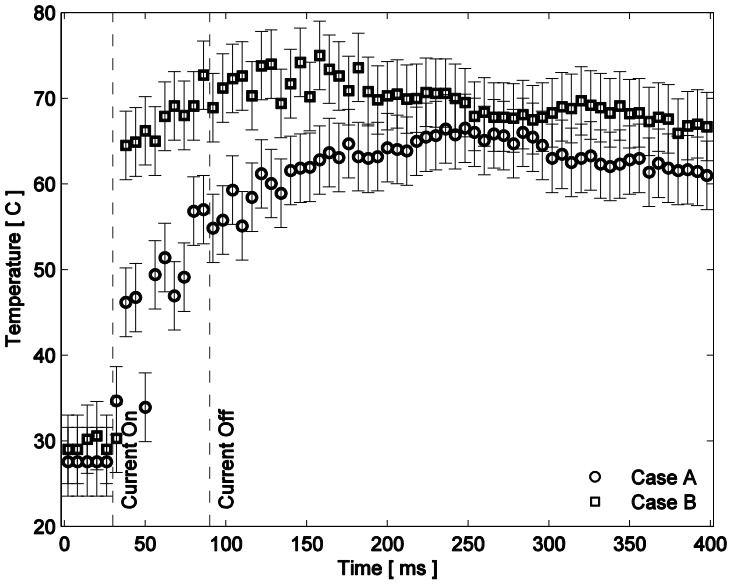

Figure III-8 - Anode temperature dynamics for Case A and B.

Cold Spray and Resistance Spot Welding: An Alternative for Aluminum Welding

This section presents the results of research that was conceived during the development of this dissertation. It's a topic of great interest and should be explored in detail by itself. The methodology and results presented here is aimed to be merely an introduction to the subject.

The experimentation, the welding model and the literature review revealed that contact resistance plays an important role for the aluminum RSW process. Its presence at the faying interface generates the heat necessary to form the weld, but on the copper interface causes localized heat and promotes rapid electrode deterioration. Solutions proposed on the literature are based on two general trends. The first approach consists on removing the oxide layer of the aluminum surface in order to diminish contact resistance.

However, the proposed cleaning methods remove the contact resistance at the faying interface as well, causing the necessity of higher currents in order to form the welds. Besides, oxide formation is instantaneous and its thickness grows as time progresses, therefore the benefits of the cleaning methods is temporal. The second approach is based on modifying the electrode geometry/composition to tolerate the heavy deterioration. These approaches have not been implemented in the production floor for different reasons, mainly the difficulty of dressing such caps preventing its reutilization.

The idea explored in this section is based on the premise that the weldability of the material should be independent of its surface condition. In other words, the heat generation on the aluminum RSW process should be independent of its random contact resistance. To achieve such independence the usage of an intermediate material at the faying interface is proposed. In such a manner the heat generation will be based on the bulk resistivity and thickness of such material.

The use of insert metals in spot welding has been explored before, mainly for the welding of dissimilar metals. These methods involve the placement of a bonded substrate, often formed through explosive welding or cold cladding as an intermediate layer to aid in the weld process. This bonded material serves the purpose of acting as an interface between the two materials to be welded and allows formation of a weld between similar metals.

Low Pressure Cold Spray (LPCS) technology has been explored as well [6]. The facility and portability of deposition and the variety on the selection of powder composition makes this technology a good candidate for the creation of intermediate layers. This technology has been successfully used for the spot welding of aluminum and

steel [3,4]. Therefore, LPCS was selected as the intermediate layer deposition method for the proposed technique.

Initially 4 powder compositions were proposed based on the resistivity of the individual components of the powder and the alloying capabilities of the composition with aluminum. Powders were sprayed on the surface of the substrate with a constant inlet air temperature and fixed pressure of 500 C and 0.62 MPa, respectively. The LPCS spray gun was held by a 3 axes robot at a constant standoff distance of 15 mm and moved across the substrate surface at a transverse speed of 2 mm/s. The powder feeding rate was about 8-12 g/min using an external powder feeder system. The powders were provided by AEE powder Supply Company with particle size -325 mesh. The powder blends were mechanically mixed during 10 hours. Before deposition, substrates were grit blasted using alumina powders with particle size -100 mesh. The LPCS system was equipped with a custom made nozzle extension made by EDM machining.

Figure III-9 shows the representative microstructure from a transverse cross-section of the coating when the powder mixture used was based on nickel and titanium. It can be found that the distribution of Ti (dark gray) particles across the coating was uniform. Large black particles at the coating and the substrate interface are seen which correspond to alumina particles embedded into the substrate during the grit blasting step. Porosity of the cold sprayed layer is defined to be in the range of 10-12%.

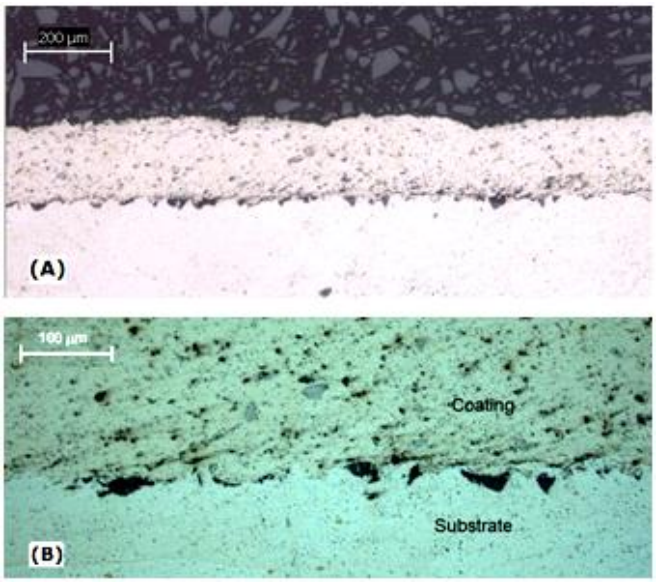

Figure III-9 - Optical micrographs of GDS sprayed Ni-Ti composite layer at low (A) and high (B) magnifications.

Welding lobes (acceptable combination of parameters to avoid cold welds and expulsions) were acquired for each powder composition. Figure III-10 shows such welding lobes. From the figure it's clearly seen that by using coatings B,C and D the objective of diminishing welding current has not been achieved (compared to Figure III-3). However, coating A produced a slight reduction of current (from 26.5KA to 21KA) when welding time was increased. Based on the fact that bulk resistance increases with temperature in contrast to contact resistance which diminishes with temperature, the reduction of current shown on the welding lobe with the increased welding time provided a good indication that the main heat contributor to the welds using this coating was bulk resistance. To corroborate this fact several welding pulses with fixed duration were used. Results obtained using 3 welding impulses were astonishing. The current required in order to form an acceptable nugget diameter was only 14KA, a drop of almost half compared to the 26.5KA required to form a similar nugget without coating.

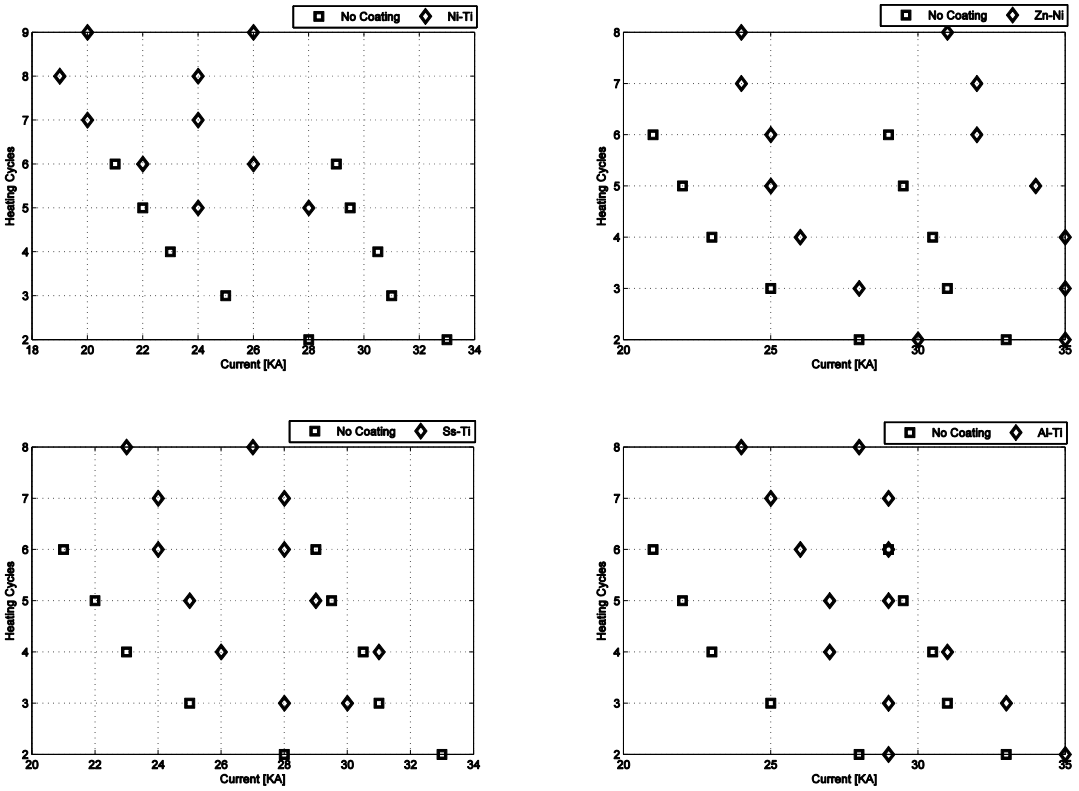

Figure III-10 - Welding lobes for the different powder compositions.

The ultrasonic system was a useful tool to monitor nugget growth and determine the heating time and cooling time between pulses for the impulse welding schedule. Figure III-11 shows an ultrasonic M-Scan acquired during welding using the schedule shown in Table III-3, the duration and location of each welding pulse is marked. It is clear from the M-Scan presented in the figure that the aluminum plate begins to form a nugget from the interface layer which then spreads through the plates. On the M-scan, one can see the dynamics of the sound reflection off the solid-liquid interface and it's seen how the cooling time is not sufficient to cool the liquid aluminum nugget at the center of the plates allowing its growth to proceed during further pulses.

Parameters (Units)	Value
Force (lbs)	800
Number of Pulses	3
Heat Time (60hz Cycles)	8
Cool Time (60hz Cycles)	2
Current (KA)	14

Table III-3 - Welding schedule used for the coated plates.

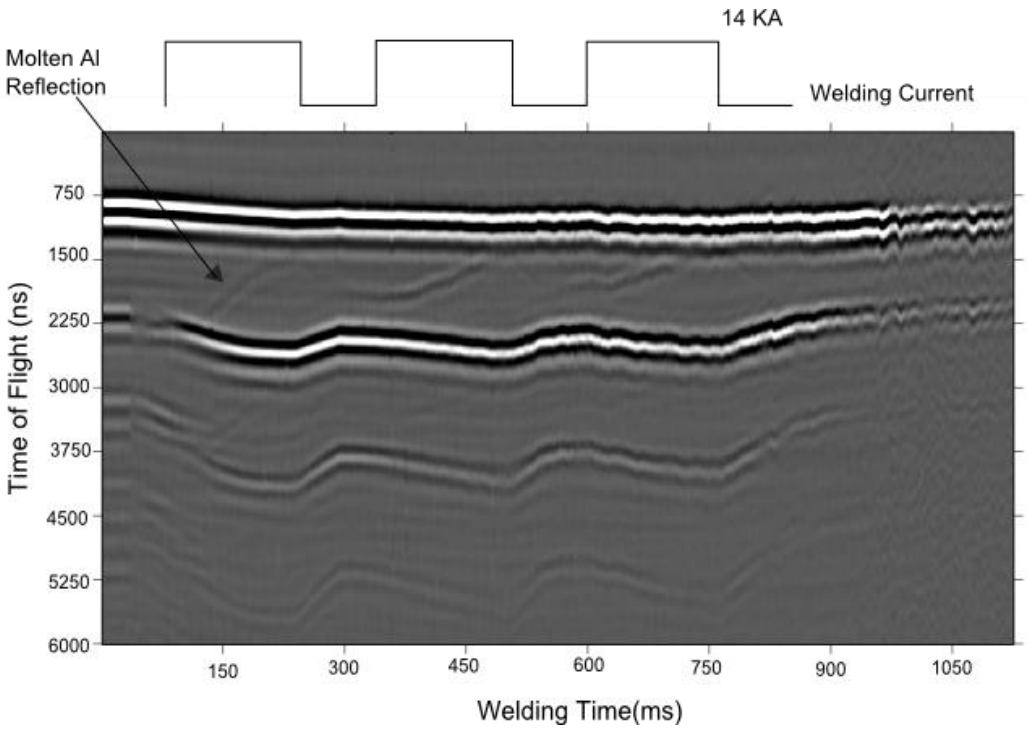

Figure III-11 - M-Scan acquired during welding using schedule shown in Table III-3

In order to determine the advantages of the current reduction explained above, a fourth cap lifetime experiment was performed using the nickel titanium coating and the

welding schedule shown in Table III-3. The last plot shown in Figure III-5 shows the results of such experiment.

Conclusions

Three cap lifetime experiments were performed during the resistance welding of Al6022 sheets with uneven thickness (0.9 mm – 1.9 mm). To study the effect of polarity and plate orientation, two cases were analyzed. Case A where the 0.9 mm plate was facing the anode electrode and case B where the 1.9 mm plate was facing the anode electrode. To ratify the results case B was repeated (case B2). The results of these experiments showed that the electrodes on case A lived 60% more compared to case B and 30% more than case B2.

Electrode deterioration was analyzed periodically by performing carbon imprints of the electrodes and measuring the contact area. The first indication of deterioration was signs of alloying between aluminum and copper noticeable by a change of color on the electrodes. After 100 welds the alloys started to detach from the electrode creating pits, these pits grew until cap failure. The anode electrode clearly showed heavy deterioration compared to the cathode electrode for the three experiments.

In order to study the effect of polarity on electrode deterioration, temperature measurements were carried on the anode and cathode electrode during the welding of a symmetric setup (1.9mm – 1.9 mm). The measurements showed that the anode electrode temperature was on average 40°C higher than the cathode electrode. This drastic change on temperature explains the heavy deterioration on the anode electrode for the three cap

lifetime studies. Another set of temperature measurements were performed on the anode electrode evaluating the case A and case B experiments. It was found that the temperature on the anode electrode for case A was on average 10°C lower than case B. The presented results give a good guideline in selecting plate orientation with respect to polarity during the resistance welding of aluminum. Based on these results it is advised to locate the thinner plate of the welding stack-up facing the anode electrode [5].

Ultrasonic M-Scans acquired with the transducer installed on the anode electrode showed the first signs of signal disappearance around 50 welds. This phenomenon matched the change of color on the face of the cap caused by the alloying between copper and aluminum. After 100 welds the back wall reflection disappears completely (Figure II-29) due to the lack of acoustical contact caused by the pits formed on the face of the anode electrode. However, when the transducer was installed on the cathode electrode the back wall reflection was present during the complete lifetime of the cap. Figure III-12A and Figure III-12B shows ultrasonic M-Scans acquired with the transducer installed on the cathode electrode after 500 and 600 welds respectively. Water temperature on the cathode electrode didn't reach the boiling point during the whole experiment and therefore, signal was present on all the M-Scans. This fact was confirmed by the temperature measurements that showed a difference about 40°C between both electrodes. All this facts indicate that in contrast to steel monitoring, the location of the transducer is not optional. If the RIWA system is planned to be used on the inspection of aluminum welding then the ultrasonic transducer should be installed on the cathode electrode.

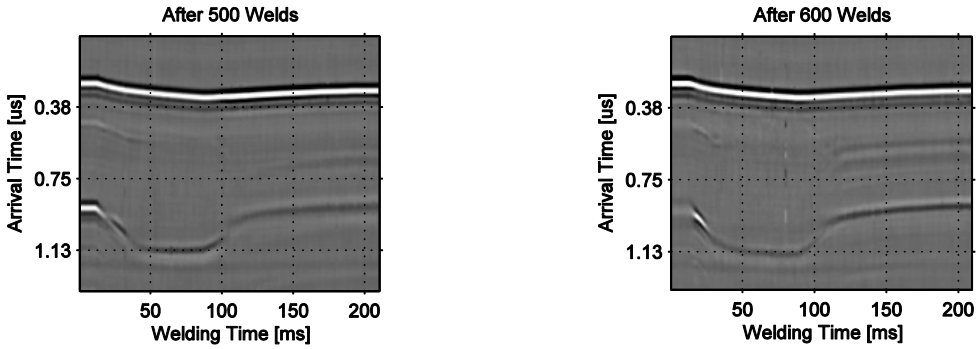

A **B**

Figure III-12- M-Scans acquired from the cathode electrode. A- After 500 Welds. B- After 600 Welds

Finally, the last section of the chapter presented an interesting approach whereby the usage of an intermediate layer made by cold spray the usage of impulse welding was made possible on aluminum. The current in order to form an acceptable nugget size was dropped from 26.5 KA to 14 KA. The reduction in current increased the electrode life to 1250 welds, 3 times more compared to case B. The proposed approach eliminates the necessity of expensive transformers and allows manufacturing plants to spot weld aluminum alloys even though they were designed to spot weld steel parts.

References

1. *Electrical Contacts: Principles and Applications*, by P. G. Slade. CRC Press, 1999.
2. *Some Tribological Influences on the Electrode-Worksheet Interface During Resistance Spot Welding of Aluminum Alloys*, by M. Rashid. Journal of Materials Engineering and Performance, 2011. Vol. 20, pp. 456-462.
3. *Dissimilar Metals Joining Using Intermediate Layers made by Cold Spray*, by **W. Perez Regalado**, A.M. Chertov, D. Dzhuriskiy, V. Leshchynsky and R.Gr. Maev. Proceedings of the XV Sheet Metal Welding Conference 2012, American Welding Society. Paper 4-3.
4. *Recent Developments in the Joining and the Evaluation of Dissimilar Metals: A Novel Two Step Process with Ultrasonic Monitoring*, by **W. Perez Regalado**, A. Ouellette, A.M. Chertov, V. Leshchynsky and R.Gr. Maev. Materials Evaluation ASNT Journal 2013. Vol. 71, No. 7, pp. 828-833.
5. *Polarity and Stackup Orientation: Effect on Electrode Life in Resistance Welding Aluminum*, by **W. Perez Regalado**, A.M. Chertov, and R.Gr. Maev. Proceedings of the XV Sheet Metal Welding Conference 2012, American Welding Society. Paper 4-5.
6. *Introduction to Low Pressure Gas Dynamic Spray*, by R.Gr. Maev and V. Leshchynsky. John Wiley & Sons, Aug 14, 2009

CHAPTER IV

ANALYSIS OF ALUMINUM ULTRASONIC M-SCANS

The ultrasonic M-Scans contain significant information about the processes taking place within the welded plates. Figure IV-1 shows an aluminum M-Scan and an schematic view of a scan acquired during the manufacturing of one of the welds described in chapter 3, where the plate thicknesses are uneven (0.9 mm - 1.9 mm). The ultrasonic transducer was installed on the cathode electrode and the 0.9 mm plate was facing the transducer.

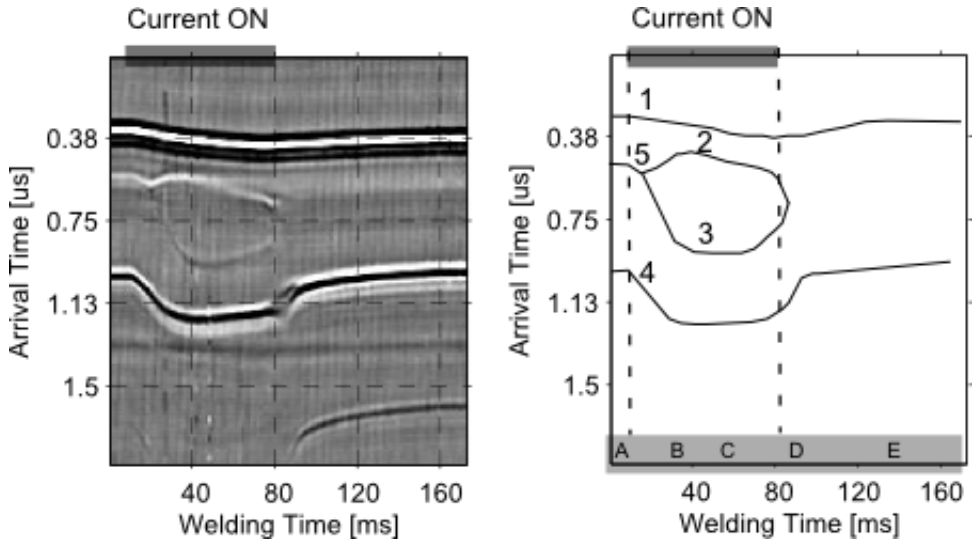

Figure IV-1- Aluminum M-Scan with Schematic view.

The line marked as reflection 1 on Figure IV-1 represents the copper-aluminum contact. The lowest, curved interface (reflection 4) is the aluminum-copper contact. Everything between these two curves takes place within the welded plates and brings

information about the weld formation. If we concentrate on the *x* axis on the image, several regions can be identified. The first region labeled as A, corresponds to the time when the aluminum plates are already squeezed by the electrodes, but no current has been applied. In this region one can see only three reflections corresponding to the copper-aluminum, aluminum-aluminum and aluminum-copper boundaries labeled as reflections 1,5 and 4 respectively. As electrical current begins flowing (region B), temperature starts increasing within the plates and the speed of sound in the heated metal gradually drops. The ultrasonic wave returns later since more time is required to travel through the welded plates. This can be seen as the delay observed in reflection 5 and 4. In region B melting occurs, noticeable by the split of reflection 5 into reflections 2 and 3 corresponding to the reflections caused by the top and bottom of the molten nugget. The next interesting region (C) appears on the second half of the heating cycle. In this region the delay on reflection 4 stops increasing and nugget growth is reduced considerably even when current is still flowing. Finally the current is turned off and the reverse process of cooling and solidification begins, labeled as area D. The slope of reflection 4 changes its sign considerably due to the increase of the sound speed in the cooler material and the liquid weld pool shrinks towards the center. Cooling continues until complete solidification. The temperature within the plates drops, making the lower curve approach the horizontal orientation (Region E).

Extensive research has been conducted on the analysis of the different features that can be extracted from the ultrasonic data. This chapter presents a summary of such features. The first section of the chapter focuses on estimating the amount of heat generated in each individual aluminum plate. The main objective of this study was to

explain the cap lifetime results shown on chapter 3, and understand the differences between case A and B of such study.

The following sections of the chapter concentrate on determining parameters that can be useful to determine the quality of the weld, such as nugget diameter and liquid penetration.

Heating Rate and Temperature Effects

The previous chapter presented an interesting study of the effect that plate orientation and polarity have on cap lifetime. Temperature measurements on a symmetrical setup (two 1.9 mm plates) showed that the anode electrode temperature was on average 40°C higher compared to the cathode electrode. This fact clearly shows the huge effect that the Peltier effect has and the importance of polarity on aluminum RSW. To determine the optimum plate orientation on uneven setups (0.9 mm - 1.9 mm plates) temperature measurements were done on the outside of each electrode under different plate orientations. It was found that by facing the 0.9 mm plate towards the anode electrode the temperature dropped an average of 10°C on each weld extending the cap lifetime by 60%.

While the temperature measurements on the previous experiments were of utmost importance, a more interesting quantity is the determination of the amount of heat generated on each individual aluminum plate. In such way one can decide which plate should face the anode electrode to diminish its deterioration. The ultrasonic system (RIWA) has shown to be a good tool for such applications [1,2].

In order to calculate changes of temperature with ultrasonic data, the temperature dependence of the sound velocity in the heated material should be known. Chapter 2 already presented the measurements obtained by Chan et al in [3] and Weaver et al in [4] where the sound velocity in aluminum was measured up to 1500ºC (T_{max}). The measurements can be approximated with two linear functions. One for when the temperature is between room temperature ($T_{room} = 25$℃) and the melting point ($T_{melt} = 660$℃) and another one for when the temperature is higher than the melting point. Equation IV-1 summarizes these two cases, where *c* represents the sound velocity in m/s and *T* the temperature in ºC.

$$c(T) = \begin{cases} -1.175T + 6519 & \text{if} \quad T_{room} \leq T < T_{melt} \\ -0.44T + 4983.7 & \text{if} \quad T_{melt} \leq T \leq T_{max} \end{cases} \qquad \textbf{Equation IV-1}$$

The delay in reflections 4 and 5 observed after the start of welding and before melting are of utmost importance. In this time range indentation and thermal expansion may be neglected, therefore, the distance traveled by the acoustic wave is given by the plates thickness. With the known distance *d* and the time of flight *t* measured from the ultrasonic M-scan, and the fact that we are working in pulse-echo mode, the sound velocity can be calculated using Equation IV-2. Finally, using Equation IV-1 and the calculated velocity *c*, the average temperature *T* can be calculated for each A-Scan in this time range.

$$c = \frac{2d}{t} \qquad \textbf{Equation IV-2}$$

Figure IV-2 shows an ultrasonic M-Scan, together with its binary version highlighting the received reflections. The start of welding and the moment of melting are marked with dotted lines. The transducer was located in the cathode electrode with the 0.9 mm plate facing the transducer.

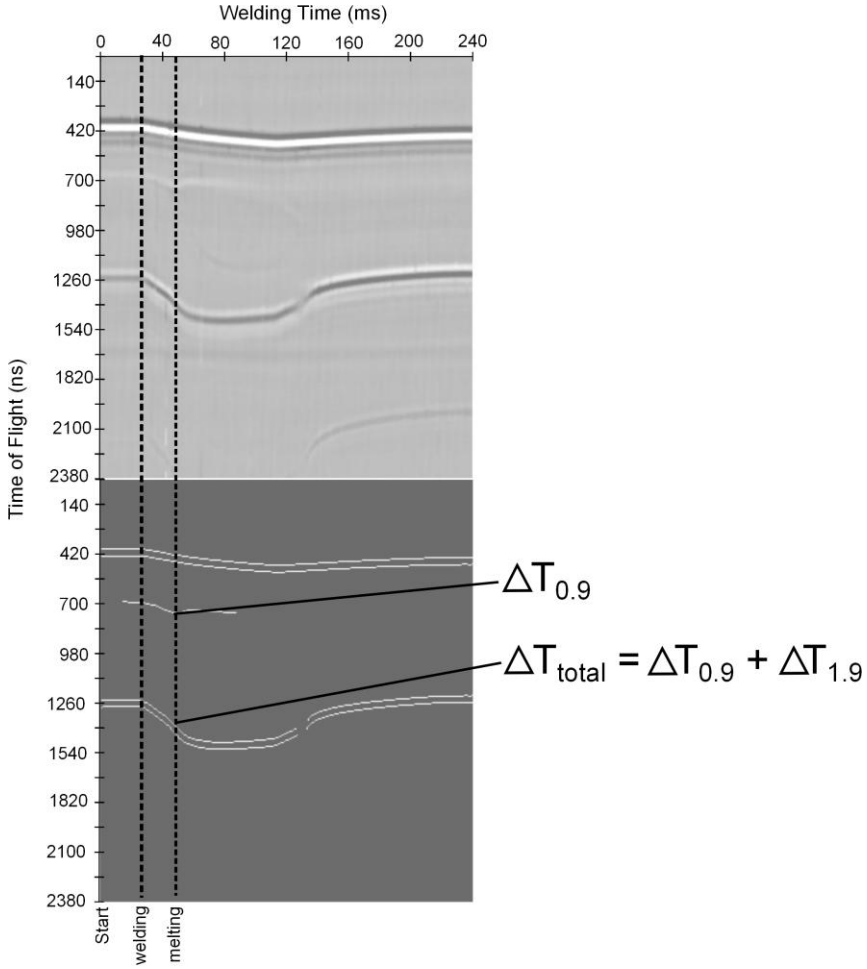

Figure IV-2- Delays caused by the increase of temperature in the 0.9 mm plate ($\Delta T_{0.9}$) and 1.9 mm plate ($\Delta T_{1.9}$).

On Figure IV-2, the delays caused by temperature changes on the 0.9 mm plate ($\Delta T_{0.9}$) and the complete stack up are marked (ΔT_{total}). These delays caused by the

differences of temperature between A-Scans ($\Delta T_{total} = \Delta T_{0.9} + \Delta T_{1.9}$) can be used to calculate the amount of heat generated on each individual plate in that instance of time. It's well known [5] that the mass of the weld zone can be calculated by approximating it as a short cylinder using Equation IV-3 and the given electrode diameter *d*, stack up thickness *h* and the density of aluminum ρ. Therefore the amount of heat in Joules (*Q*) on each plate can be calculated using it's mass *m*, the calculated change of temperature ΔT, and the specific heat of aluminum c_p (Equation IV-4).

$$m = \frac{\pi}{4} d^2 h \rho \qquad \textbf{Equation IV-3}$$

$$Q = m c_p \Delta T \qquad \textbf{Equation IV-4}$$

The heat measured from the ultrasonic data had an average value of 5.37 KJ on the 1.9 mm plate and 2.29 KJ on the 0.9 mm plate. Also, from the ultrasonic M-Scans (Figure IV-2) is seen that the delay of the nugget reflection on the 1.9 mm plate increases faster compared to the 0.9 mm plate. These facts show that even when contact resistance is the major contributor for heat generation during aluminum welding, bulk resistance plays an important role on the heat generation as well. The thicker the plate, the higher the bulk resistance and consequently higher heat generation in such plate.

Heat measurements from the ultrasonic data match the electrode temperature measurements shown in chapter 3. Temperature on the cap surface was higher when the thick plate was located towards the anode electrode. These results reaffirm that by facing the thicker plate towards the anode electrode degradation is accelerated.

Nugget Diameter Estimation

Nugget diameter is one of the most important parameters when determining the quality of a spot weld [6]. As a general criterion, the spot weld nugget must have a diameter of $5\sqrt{t}$, where *t* is the governing metal thickness (usually the minimum) of the plates being welded. For instance, spot welding of two 0.9 mm sheets together should result in an expected nugget of 4 mm diameter. This parameter is very important and any quality engineer measures it in order to accept or reject a spot weld.

It's important to keep in mind that the transducer used in the RIWA system consists of a single piezoelectric element and therefore is only able to monitor one dimension (the vertical axis of the spot welds). Information about the lateral dimension cannot be directly measured with the current setup, but based on the physics of the process and the information available, it can be estimated. It was previously mentioned that the parameter to determine nugget diameter from the ultrasonic M-Scan on steel spot welds is the maximum TOF of the signal that passes through the welded plates and comes back to the receiver (reflection 4). The main mechanism causing the increase of TOF is the velocity drop due to the temperature increase (vertical axis) within the welded plates. Statistical studies conducted on steel spot welds have shown a very high correlation between maximum TOF and nugget diameter. However, the initial study explained in the last section of chapter 2 showed that maximum TOF cannot be used to estimate nugget diameter on aluminum. The welding models described on Chapter 2 can be used to explain the main reasons of this difference between the inspection of aluminum and steel.

Figure II-20 show the transient temperature distributions of the vertical axis for a steel spot weld and Figure II-21B the average and maximum temperature for each distribution. Figure II-21B clearly shows that the average temperature in steel spot welds increases considerably as welding time increases. Since sound velocity is inversely proportional to temperature (Figure II-5), this fact explains the increase of TOF seen on reflection 4 on the steel M-Scans (Figure II-4). However, in order to correlate this TOF (which corresponds to the temperature increase on the vertical direction) to nugget diameter (lateral direction) a study of the nugget growth dynamics is required. While Figure II-18 shows how the molten nugget grows on the last welding cycles of steel spot welds, the figure does not provide a good description of the geometry changes with respect to time. To illustrate these changes, the nugget geometry can be approximated with an ellipse where the minor axis corresponds to the vertical axis of the welding setup and the major axis of the ellipse to the lateral direction of the welding setup.

Figure IV-3 shows a schematic of these assumptions. In such way, the foci (F) and hence, the eccentricity (ε) of the ellipse can be calculated for each time step using Equation IV-5.

$$\varepsilon = \sqrt{\frac{a^2 - b^2}{a^2}} = \sqrt{1 - \left(\frac{b}{a}\right)^2} = \frac{F}{a} \qquad \textbf{Equation IV-5}$$

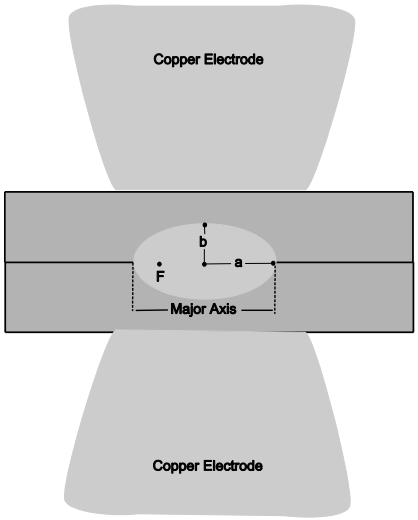

Figure IV-3- Nugget ellipse schematic.

The eccentricity can provide information of the relation between the height and diameter of the nugget. A decrease of eccentricity will suggest that nugget growth on the vertical direction exceeds the growth on the lateral direction and vice versa, an increase on eccentricity will indicate that nugget growth is substantial on the lateral direction (nugget diameter) and minimum on the vertical direction (nugget height). Figure IV-4 shows a diagram of these facts. Figure IV-5 shows the calculation results of the transient eccentricities for the simulated steel spot weld. The plot clearly shows that the eccentricity presents a linear behavior with a positive slope, indicating the majority of the nugget growth is on the lateral direction on every time step. Since temperature and TOF across the vertical direction of the weld increases with welding time and nugget diameter increases as well (Figure IV-6), the TOF across the vertical direction is a good ultrasonic parameter to estimate nugget diameter on steel.

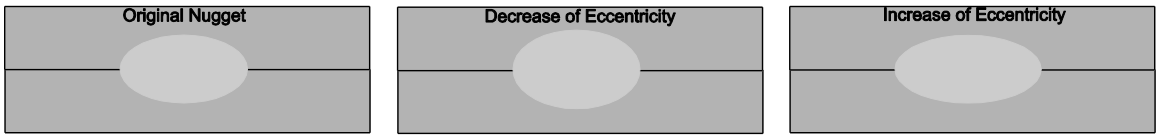

Figure IV-4- Illustration of an increase and decrease eccentricity.

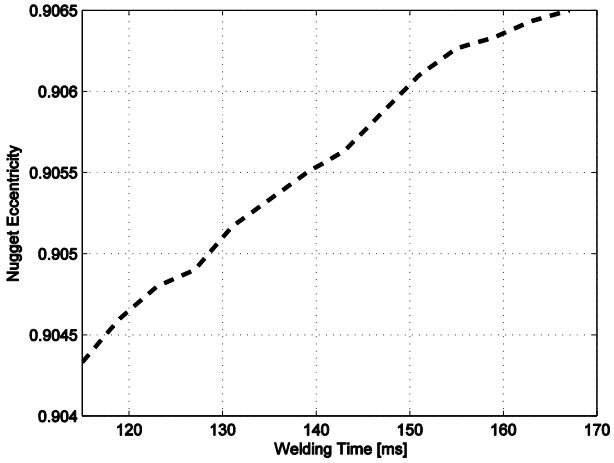

Figure IV-5- Transient eccentricity for the simulated steel spot weld.

Aluminum shows a completely different behavior. Temperature changes on the vertical axis are minimal on the second half of the welding cycle (Figure II-19). For this reason, TOF changes are minimal on this region (region C Figure IV-1). To understand the nugget growth dynamics on aluminum, the same eccentricity analysis described above was applied to the simulated aluminum spot weld model. Figure IV-6 shows the results of these calculations. In the figure can be seen that during the first 45 ms of welding, eccentricity values show a negative slope, meaning that during this time nugget growth on the vertical direction (nugget height) exceeds the nugget growth on the lateral

direction. After 45 ms the eccentricity values show a positive slope indicating that in this range nugget growth on the lateral direction exceeds the growth on to the vertical direction. Chapter 2 describes that 30% of nugget diameter is developed on the last cycle of the welding process. Since in this time range (after 45 ms) temperature changes are minimal on the vertical axis (Figure II-21A), and hence TOF does not increase considerably (region C Figure IV-1), TOF cannot be used to estimate nugget diameter on aluminum.

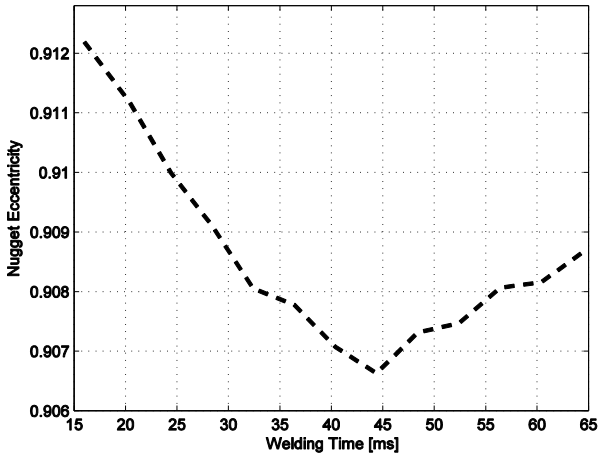

Figure IV-6- Transient eccentricity for the aluminum spot weld.

Experimental verification of the aluminum eccentricity results included ultrasonic inspection and destructive testing. Ultrasonic M-Scans showed that nugget height grows only during the first 45±5 ms of the welding process (Figure IV-1 and Figure IV-8). This fact is in accordance with the eccentricity values, where the results show a negative slope (Figure IV-6) in the same time range, followed by a change to a positive slope. To verify nugget diameter, an experiment where the welding time shown in Table III-2 was varied from 1 to 4 cycles was performed. Thirty welds were done using each welding time, peel test and nugget diameter measurements were done for each case. Electrodes were cleaned

every 10 welds to avoid electrode deterioration. Table IV-1 shows the results of these measurements. The penetration of the nugget formed after 1 welding cycle was very low to enable a pullout button on the destructive test, causing the high standard deviation for this welding time. However, after 2 cycles penetration was enough to allow accurate diameter measurements. Nugget diameter at the end of the second cycle was 3.2 mm. On the third and fourth cycles the nugget grows to 3.5 and 4.5 mm respectively. These results clearly show the behavior explained by the eccentricity analysis where lateral growth is higher on the last 2 cycles of the welding process (positive slope Figure IV-6 after 45 ms). A more clear visualization of this fact can be seen in the experimental analysis performed by Rashid et al in [7]. The main focus of the author was to study the surface interaction at the worksheet/worksheet interface and its effects on nugget growth. However, on his analysis the author performed periodic cross-sections with increasing welding time. Figure IV-7 presents the results of Rashid [7]. The figure clearly shows that during the first 2 cycles nugget growth on the vertical direction exceeds the growth on the lateral direction (negative slope on eccentricity) until achieving its maximum height between the second and third pulse. Once that nugget development on the vertical direction is finalized, lateral growth is substantial on the following cycles (nugget diameter).

Welding Time	Nugget Diameter (mm)	Std. Deviation (mm)
1 cycle (16.7 ms)	3.2	0.3
2 cycles (33.3 ms)	3.2	0.15
3 cycles (50 ms)	3.5	0.09
4 cycles (66.7 ms)	4.5	0.09

Table IV-1 – Nugget diameter measurements for different welding times.

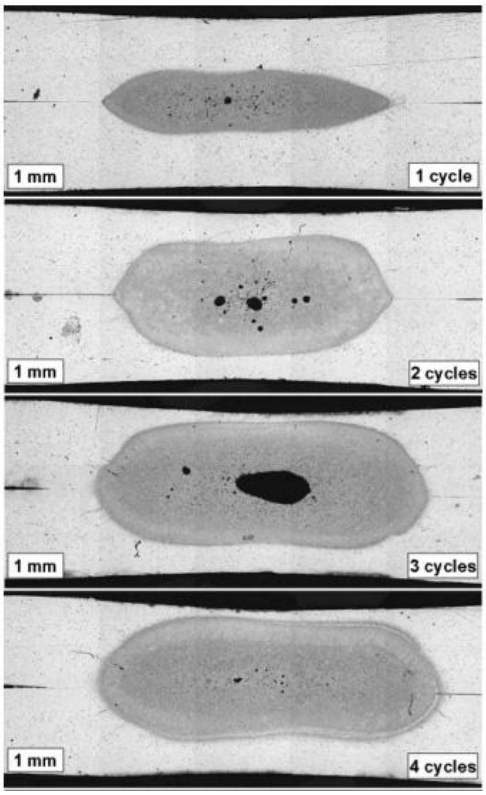

Figure IV-7- Cross-Sections for different welding times. Courtesy of Rashid et al in [7].

The studies previously described showed that there is not a correspondence between the maximum TOF and nugget diameter on aluminum. However, the analysis described above, the simulations presented in Chapter 2 and the experimental data acquired on Chapter 3 showed a fundamental difference between a non acceptable weld and an acceptable weld. Acceptable welds show melting and achieve the maximum temperature on the vertical axis sooner in time than non acceptable welds. In other words, the faster the nugget finishes developing in the vertical direction, the bigger the diameter will be. Simulated and experimental TOF curves showed the same behavior. Figure IV-8A and Figure IV-8B illustrates this fact on two M-Scans of welds with a nugget of 2.5 and 4.5 mm respectively, note that the arrival time for the front (F) and back (B) wall reflections are marked with a blue and yellow line respectively and the current on (C_{on}) and current off (C_{off}) moments of the welding process are marked with two blue lines as well. On the figure it can be seen that the 2.5 mm nugget M-Scan achieved melting at the 40 ms mark and the maximum temperature (beginning of region C) at the 80 ms mark, while the 4.5 mm nugget M-Scan achieved melting at the 35 ms mark and the maximum temperature at the 55 ms mark. This behavior was observed on every aluminum M-Scan. Note that the beginning of region C is noticeable not only by the decrease of the back wall delay but also on the reduction of nugget growth on the vertical direction.

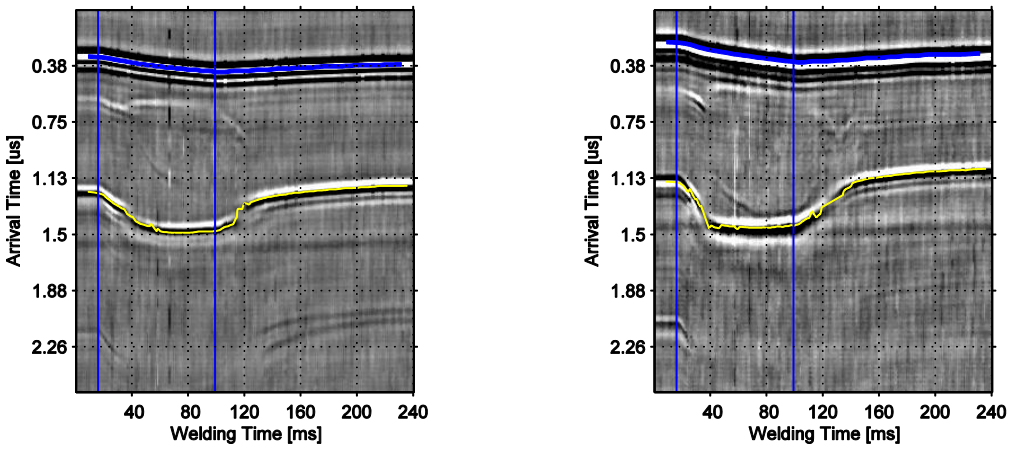

Figure IV-8- Aluminum M-Scan comparison. A - 2.5 mm nugget. B - 4.5 mm nugget.

A good ultrasonic parameter that is able to estimate nugget diameter in aluminum should be sensitive not only to the maximum temperature on the vertical axis (TOF), but also to the time when that temperature is achieved. A metric sensitive to these two variables is proposed in Equation IV-7. If we consider the back wall echo *B* of each A-Scan i as signal $x_i(t)$ and the first signal before starting the welding process ($i = c_{on} - 1 = 0$) as a reference signal $x_0(t)$. Each signal in the set of N back wall echoes acquired during the welding process can be seen as a delayed version of the reference signal $x_0(t)$ (Equation IV-6). The delay D_i will reach its maximum on the beginning of region C and then it will remain fairly constant until the end of the welding process. Therefore, if we analyze the accumulation of the delay during the complete welding process, D_{ac} (Equation IV-7), we will observe an increase on its value if melting and region C are achieved sooner in time or a decrease otherwise. D_{ac} was calculated for the simulated curves showed in Figure II-26. The results showed $D_{ac} = 9.15\ \mu s$ for the 4 mm nugget

and $D_{ac} = 5.91\ \mu s$ for the 2 mm nugget a difference of 36% between an acceptable and a non acceptable weld.

$$x_i(t) = x_0(t - D_i) \qquad 1 \leq i \leq N$$ **Equation IV-6**

$$D_{ac} = \sum_{i=1}^{N} D_i$$ **Equation IV-7**

The correlation of D_{ac} with nugget diameter was tested on the different stages of cap degradation. The welded coupons were destructively tested to check the nugget size. The corresponding measured diameters were related to the obtained ultrasonic data. Figure IV-9 shows the correlation data for a new electrode cap pair (Figure IV-9A) and a pair of electrodes used for 400 welds (Figure IV-9B), the transducer was installed on the cathode electrode. The correlation curves showed an average error in weld size estimation of 0.7 mm. For nugget sizes in the range of 4.0 to 6.0 mm this error in prediction is acceptable for reliable quality inspection [8]. Note that these two cases are presented to illustrate that even at the end of the cap lifetime (Figure IV-9B), the proposed metric correlates well with nugget diameter and it is possible to use the RIWA system in degraded caps by adjusting the correlation parameters (slope and intercept). However, in production it is common to dress the electrodes; this action, returns the electrode face to its original shape (new state) increasing its life and performance. For aluminum applications, electrode dressing is performed every 100-150 welds. Therefore, the correlation data for new electrodes (Figure IV-9A) can remain unchanged to estimate

nugget diameter during the cap life. This correlation was used to estimate nugget diameter in the following chapters.

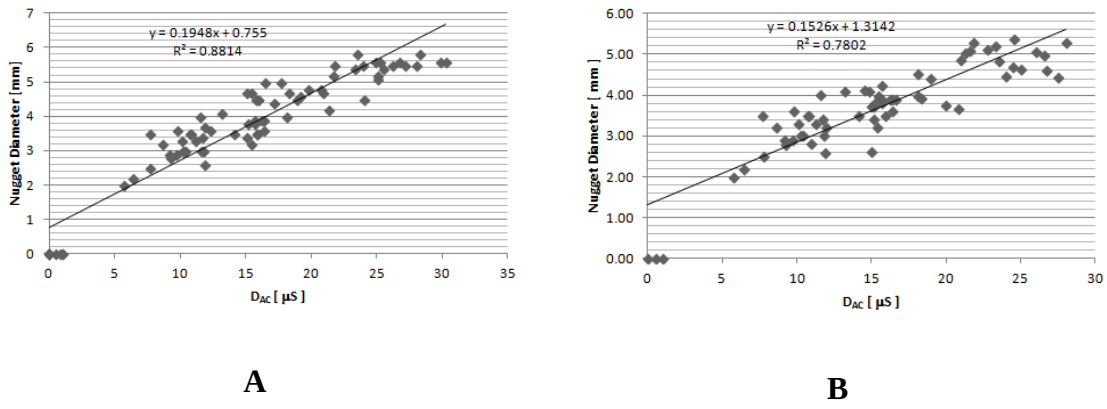

A **B**

Figure IV-9- D_{ac} to nugget diameter correlation curves. A – New electrode cap. B - Cap after 400 welds.

Liquid Penetration Measurements

While nugget diameter is an important parameter in determining the weld's quality, there are other features of the weld, such as liquid penetration, which may complement nugget diameter and provide useful information. According to automotive standards, the liquid penetration should be above 35% in respect to plate thickness [6]. The combination of these two parameters (nugget diameter and liquid penetration) provide an optimum description of a weld's strength and hence its quality.

The RIWA system is able to directly measure the liquid penetration thanks to reflections number 2 and 3 which arise due to the acoustic impedance mismatch between the solid and liquid metal. The theoretical intensity of such reflections can be calculated

with Equation IV-8 based on the acoustic impedances ($Z = \rho C$, where ρ denotes density and C sound velocity) on each side of the liquid boundary ($Z_{Solid} = Z_1$ and $Z_{liquid} = Z_2$). Such impedances can be calculated assuming equal temperature from both sides of the boundary and that the metal is solid from one side and liquid from another (T_{melt-} and T_{melt+}). Calculations for aluminum considering a speed of 6490 m/s and a density of 2700 kg/m^3 on the solid part and a speed of 4690 m/s and a density of 2389 kg/m^3 on the liquid part, produced as a result an intensity reflection coefficient of 0.049. Calculations show that the reflection coefficient between solid and liquid aluminum is more than 4 times higher compared to steel (0.011), suggesting that the aluminum properties allow an enhanced visualization of the nugget reflections on aluminum M-Scans.

$$I = \left(\frac{Z_2 - Z_1}{Z_2 + Z_1}\right)^2 \qquad \textbf{Equation IV-8}$$

To establish the correspondence of the liquid penetration observed on the ultrasonic data and the actual geometry of the weld, 20 welds were manufactured using different welding schedules to achieve variable liquid penetrations. Metallographic cross-sections were prepared for each sample in order to visualize the weld geometry. The preparation of the cross-sections was done using a Buehler Delta AbrasiMet 1000 for cutting, a Buehler SimpliMet for sample packing and Buehler PowerPro 3000 for grinding and polishing. Finally, the samples were etched with Keller's reagent for 10 seconds.

Figure IV-10 shows the cross-sections and corresponding ultrasonic M-Scans of two welds with different liquid penetration. The figures clearly show that there is a direct correspondence between the ultrasonic data and the cross-section of the sample. Figure IV-10A shows a shallow nugget with a penetration of 33% and Figure IV-10B a penetration of 65%. Measurements from the ultrasonic data showed an average error of 9%. Note that the percentage measurements on the ultrasonic data were done with respect to plate thickness at the current off moment.

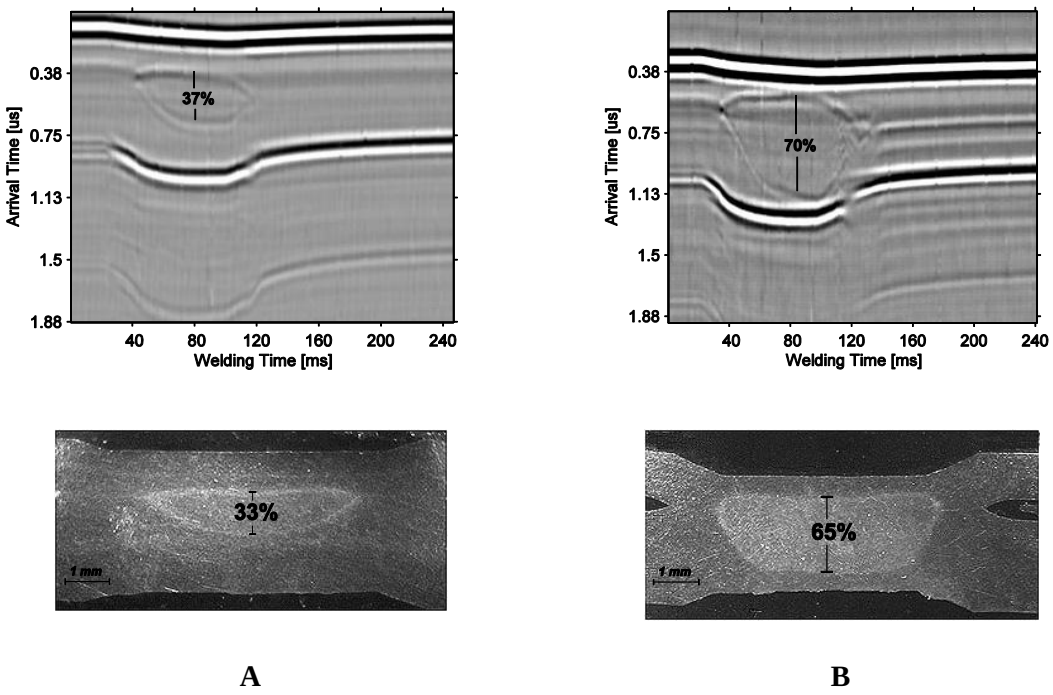

Figure IV-10- Liquid penetration measurements. A – 33% penetration. B – 65% penetration.

Central Interface

The analysis described in this chapter has been focused on distinguishing between acceptable and non acceptable welds by measuring the molten nugget height and

estimating its diameter. The most obvious case of an unacceptable weld is when there is no melting at all (stick weld). Figure IV-11 shows an ultrasonic M-Scan of an aluminum stick weld. As described in the previous section, the delay of reflection number 4 on every A-Scan is minimal. Another interesting feature is the central interface. Note that reflection number 5 (central interface) never splits into reflection number 2 and 3 indicating that melting didn't occur. The central interface is present before, during and after welding. This fact is used during the characterization of steel spot welds. If the central interface is present after the current off moment, the weld is labeled as a stick weld.

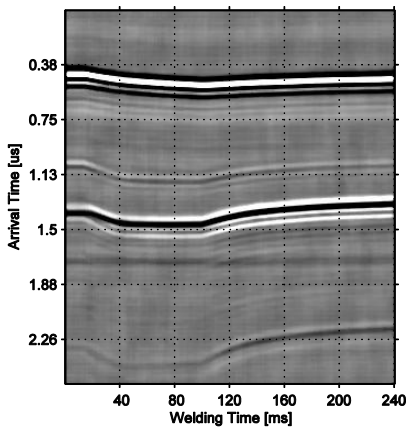

Figure IV-11- M-Scan for an aluminum stick weld.

Aluminum M-Scans showed an interesting phenomenon. In some cases, acceptable welds show an extra reflection between the front back wall reflections (central reflection) after solidification. Figure IV-12 shows this phenomenon. Note that for the aluminum M-Scan shown in Figure IV-12 the 1.9 mm plate was facing the transducer.

The reflection at the Al-Al boundary can be observed in the 0 to 20 ms time range before the welding process starts. As described before, during the welding process this interfaces splits due to melting. It's clearly seen that a nugget with penetration above 60% was achieved. However, after solidification (in the 160-240 ms time range) a reflection between the plates is present. Note that the arrival time of such reflection is different than the central interface observed before the welding process. It has been found that this reflection is caused due to porosity.

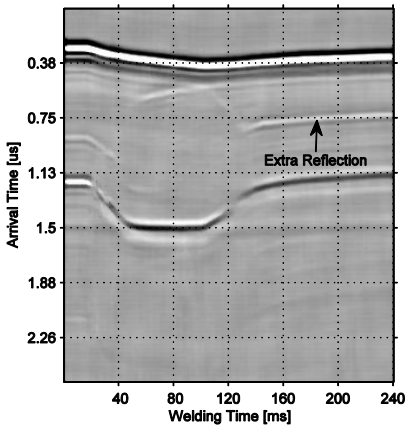

Figure IV-12- Aluminum M-Scan with a central reflection after solidification.

Porosity in resistance spot weld nuggets is very common and is more common in aluminium alloys than steel. These voids result when the alloying elements such as Mg and Zn evaporate to form gaseous bubbles. After solidification, these gaseous bubbles are trapped between the solids to create voids. Voids are usually located at the centre of the molten pool where the temperature is highest. The black spots shown in the cross sections in Figure IV-7 are examples of such voids.

Conclusions

This chapter presented a deep analysis of the aluminum M-Scans. The first section described a method to measure the heat generation on each individual plate from the ultrasonic data. The method is based on the delays observed on the aluminum-aluminum and aluminum-copper reflections and the temperature dependence of the sound velocity on aluminum. The results showed that heat generation on the 1.9 mm plate is more than two times the heat generated on the 0.9 mm plate.

The rest of the chapter focused on extractable characteristics from the ultrasonic data in order to be able to determine the weld's quality. The second section described in detail and compared the nugget growth dynamics on aluminum and steel. It was concluded that nugget growth on aluminum differs greatly when compared to the nugget growth on steel. The main differences are that a majority of the aluminum diameter is developed during the first welding cycles followed by growth in nugget height. Just a few milliseconds after starting the second half of the welding process nugget height achieves its maximum (Region C). After these facts, nugget diameter continues to grow until obtaining its final size. Steel, on the contrary, shows a constant steady nugget growth on both directions. Nugget development in steel occurs on the second half of the welding process. Based on these events an ultrasonic metric D_{ac}, able to estimate nugget diameter from the ultrasonic data was proposed. Using this metric, it was found that nugget estimation can be achieved with an average error of 0.7 mm.

Finally, the last two sections showed that liquid penetration measurements can be performed directly from the ultrasonic data. This is possible thanks to the reflections

caused by the top and bottom of the molten nugget. Measurements showed an average error of 9%. When melting does not occur, the central interface does not disappear; this may be an indication of a stick weld. However, a special case where a central reflection is present in welds with good penetration was described.

References

1. *Ultrasonic Method and Apparatus for Thermal Process Monitoring in Flat Parallel Structures. A Case Study Using Resistance Spot Welding*, by **W. Perez Regalado**, A.C. Karloff, A. Lui, A.M. Chertov, R.Gr. Maev. Proceedings of the 12th International Symposium on Non-destructive Characterization of Materials, July 2011. Paper A-054.
2. Thermal Process Monitoring in Flat-Parallel Structures using Ultrasound, by **W. Perez Regalado**, A.C. Karloff, A. Lui, A.M. Chertov, R.Gr. Maev. Conference presentation at the 12th International Symposium on Nondestructive characterization of Materials (NDCM-XII),Virginia Tech, Blacksburg, Virginia, USA, July 2010.
3. *Measurements of the Velocity of Sound in Liquid Aluminum to 1800 K*, by J.P. Chan J. Proc. 5th Symposium on Thermo Physical Properties 1970, Vol. 14, No. 4, pp.541–563.
4. *Temperature Dependence of Ultrasonic Diffuse Fields, Implications for the Measurement of Stress*, by R. Weaver and O. Lobkis. Proc Review of Progress in Quantitative Non-destructive Testing 2001. Vol. 20, No. 1, pp. 1480-1488.
5. *Resistance Welding: Fundamentals and Applications*, by H. Zhang, J. Senkara Second Edition, CRC Press, 2011.

6. *Chrysler Resistance Welding Maintenance Manual, Manufacturing Technical Training*. T510-1998.
7. *Nugget formation and growth during resistance spot welding of aluminium alloy 5182*, by M. Rashid, J. B. Medley and Y. Zhou. Canadian Metallurgical Quarterly 2011.Vol. 50, No. 1, pp. 61-71.
8. *Real Time Ultrasonic Inspection System for Resistance Spot Welds. Case Study in Production Environment*, by R.Gr. Maev, A. Chertov, A. Karloff, **W. Perez Regalado**, A. Tchipilko, P. Lichaa, D. Clement and T. Phan. Proceedings of the XV Sheet Metal Welding Conference, American Welding Society, 2012. Paper 2-5.

CHAPTER V

SPOT WELD QUALITY CHARACTERIZATION

The previous chapter described the features that may be extracted from the ultrasonic M-Scans in order to characterize the weld. While these features (liquid penetration, nugget diameter estimation, central interface disappearance) are easily recognizable by a human inspector, the automatic detection of such characteristics, which is the final goal of this dissertation, is not a trivial task.

The focus of this chapter is to present the details of how the A-Scans and M-Scans were digitally processed to extract such features. The main purpose of the first two sections of the chapter is to detect the front and back wall reflections in order to calculate D_{ac}. In the first section a brief comparison of the most common signal processing algorithms used to detect ultrasound pulses is presented together with the results on aluminum M-Scans. Then, an image processing algorithm that detects the principal curve formed at the front and back wall reflections is proposed and presented.

The next objective is the detection of the low-contrast reflections produced by the molten metal in order to measure the liquid penetration. Finally, a fuzzy system responsible of determining the final quality of the weld based on these parameters is presented in the last section of the chapter.

Review of Pulse Detection Methods

In order to calculate D_{ac}, the metric described in chapter 4 able to estimate the nugget diameter, the location of the different reflections along each individual A-Scan should be determined. Several methods exist to achieve this task. Some of the most common techniques are based on detecting the pulse based on its amplitude. Techniques such as: amplitude thresholding, maximum peak detection, zero crossing detection and envelope peak detection have been extensively used [1-3]. Pulse detection by threshold is the simplest and therefore one of the most commonly methods used. The usage of this technique is limited to applications with high signal to noise ratio (SNR) and with no pulse overlapping. The selection of the threshold value is highly dependent of the measurement setup. While a high threshold value might detect too few points, a small value would result in the detection of noise as a pulse. The inspection of only a single value could interpret singular noise spikes as a valid signal. Besides, because of the shape of a reflected pulse, a single reflection might be interpreted as multiple peaks. Instead of defining threshold values, and assuming the signals are zero-mean, it is possible to use the zero crossings of the signal for pulse detection [2]. Looking for the change of the signal's sign is very straight forward and easy to implement. However, the presence of noise will still affect the detection. Figure V-1 shows an aluminum M-Scan and the results of detecting and thresholding two peaks along each A-Scan based on the amplitude. It is clearly seen that noise affects the detection and that the low amplitude of the back wall reflection during melting is not detected.

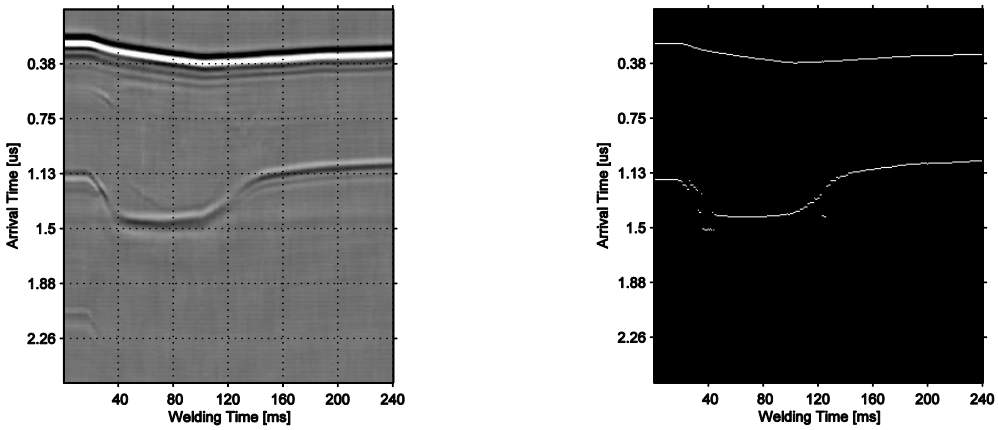

Figure V-1- Pulse detection based on two thresholds.

The usage of the analytical representation of the signal (Hilbert transform) is a common way of avoiding these issues. The envelope effect of this representation simplifies the pulse detection by finding maximums or thresholding the envelope. Figure V-2 shows the detection of the front and back reflections of the same aluminum M-Scan by finding two maximums in the envelope of each A-Scan. The figure clearly shows that for pulses with high SNR such as the front wall reflection the detection shows a continuous curve. However, when the signal amplitude decreases noise is detected as a valid signal. However, the detection of the back wall reflection at the moment of melting improves with this method compared to the results shown in Figure V-1.

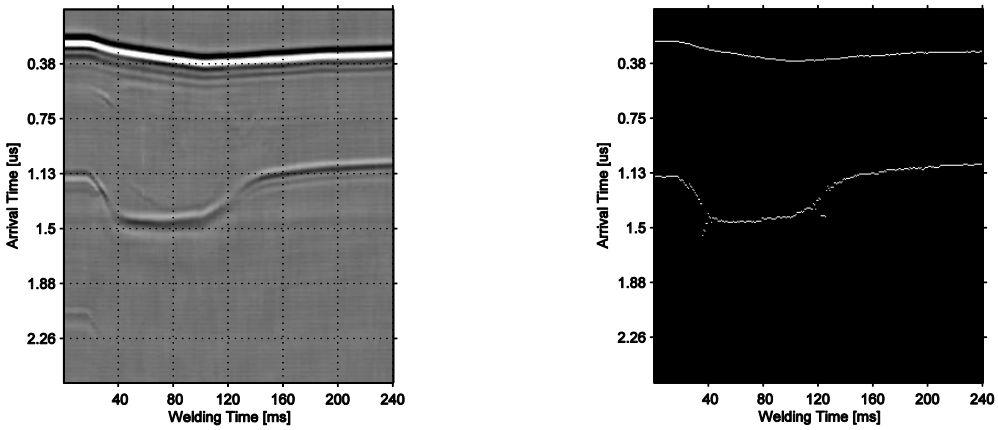

Figure V-2- Pulse detection based on the peak of the envelope.

Another approach for pulse detection is based on template matching by correlation methods. In this approach, the shape of the signal should be known before processing the signals. The most important consideration when using these methods is the choice of the peak shape. Intuitively the best shape would either be the originally emitted pulse or its negation (acoustic impedances mismatch might cause a phase shift). The approach followed in the results shown in Figure V-3, was to obtain a template pulse for the front and back wall reflection. These templates were extracted from the first A-Scan before starting the welding process. Then, the templates were correlated with each A-Scan and finally two maximums were obtained from the correlation results. This method showed continuous results on the first half of the welding process. However, on the second half (after the 100 ms mark) an artificial discontinuity on the back wall reflection is detected. This phenomenon is caused by the frequency-dependent attenuation on the liquid metal. It's well known [4] that as the wave passes through the liquid layer high frequencies are attenuated. The frequency-dependent attenuation yields to a signal shape change on the time domain which produces the miss-detections on the cross-correlation

results. In order to improve the detection using this method the effects of the frequency-dependent attenuation should be taken into consideration in the pulse template.

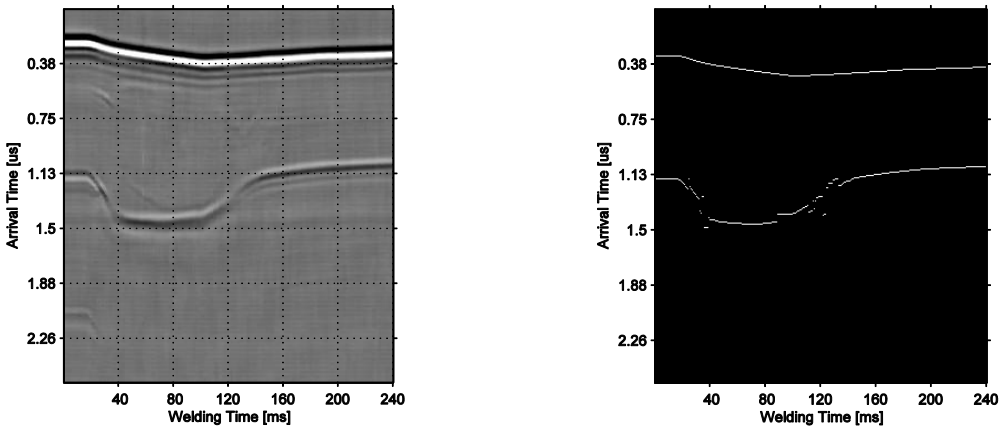

Figure V-3- Pulse detection based on correlation.

The continuous wavelet transform (CWT) has been often used for edge detection in ultrasound images [5]. The wavelet transform is defined by Equation V-1.

$$W_f(\tau, a) = \frac{1}{\sqrt{a}} \int_{-\infty}^{\infty} f(t)\, \psi\left(\frac{t-\tau}{a}\right) dt \qquad \textbf{Equation V-1}$$

Where $f(t)$ is the signal to be analyzed, ψ is often referred to as the mother wavelet which is translated in time by a variable shift τ and scaled by a an amplitude parameter. The mother wavelet can be any function and is chosen based on the application. A common mother wavelet used to process ultrasound signals is the second

derivative of the Gaussian distribution, commonly referred to as the Mexican hat wavelet. This wavelet is a real function which reacts to the second derivative of a signal. The zero crossing of the CWT using the Mexican hat as the mother wavelet would correspond to an edge or discontinuity in the signal to be analyzed [6].

The first step in the edge-detection algorithm is the calculation of the CWT scalogram, which shows the CWT as a function of both scale and time for one A-Scan. The scale array to be used in ultrasound signals as recommended by [5] is shown in Equation V-2 where $N = 4$ and $j = 1, 2, \ldots, 40$. The Figure V-4C shows an example of a scalogram obtained for the A-Scan marked on the M-Scan shown in Figure V-4A and plotted in Figure V-4B.

$$a(j) = 2^{j/N} \qquad \textbf{Equation V-2}$$

Next, the wavelet spectrum $S_f(a)$ (Equation V-3) was calculated for each scale a in the scalogram. By modulating this integral (multiplying it with the inverse of the square of the scale) the energy contribution at a particular scale as a function of scale can be obtained. The scale to perform detections on is then given by the scale value at which we find the maximum of the spectrum. This optimal scale marked with red in Figure V-4C with a red line, is then used to perform the detection. The edge on the signal is defined as the maximum of the squared CWT at the optimum scale.

$$S_f(a) = \frac{1}{a^2}\int_{-\infty}^{\infty} \left|W_f(\tau, a)\right|^2 d\tau$$ **Equation V-3**

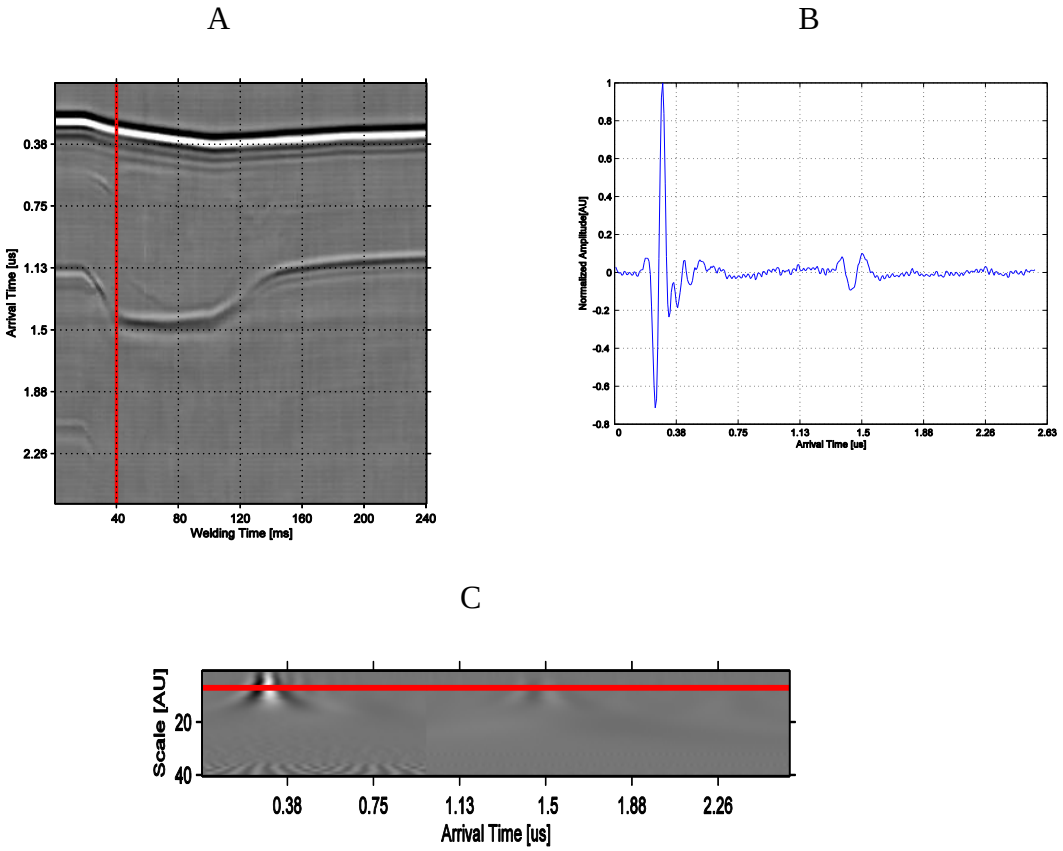

Figure V-4- Edge detection using the continuous wavelet transform (CWT). A-Original M-Scan. B-A-Scan being processed. C- Scalogram of selected A-Scan.

Figure V-5 shows the edge detection using the CWT method. The detection during melting and during the second half of the welding process improves compared to the correlation method. However, when the amplitude of the reflection is low, noise still gets detected as a valid signal. The main drawback of this method is that due to the huge number of calculations required, the detection of a single pulse is time consuming and

computationally expensive. The original author [5] recommends the usage of this method in applications where the shape of the edge is predictable and the number of A-Scans to process can be reduced.

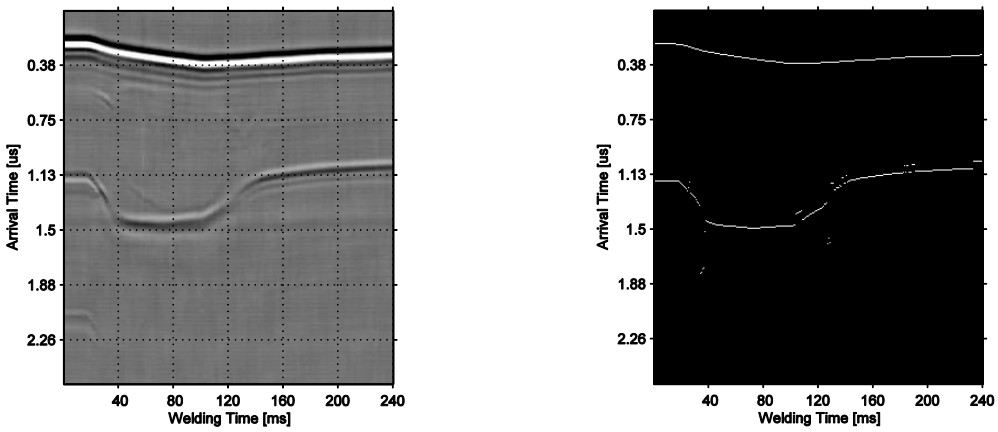

Figure V-5- Pulse detection based on the continuous wavelet transform (CWT).

This section has reviewed some of the most common ultrasound pulse detection techniques. Three general approaches were explored: detection based on amplitude, peak of the envelope and template matching. Results have been presented for each different method as a binary image. While the images are a good basis for visual evaluation of the results of the detection, a quantitative comparison will be presented in the last section of the chapter.

Edge Detection and Principal Curve Determination

The methods described in the previous section have been based in detecting the reflections of the different layers on each individual A-Scan and do not take advantage of repetitive patterns between neighbouring A-Scans. Therefore, when the amplitude of the pulses drops or when the pulse shape changes, the reflections will not be detected. In this present section of the dissertation a multistep algorithm that treats the aluminum M-Scans as greyscale images instead of sets of A-Scans will be presented. The main goal of the algorithm is to detect the curves formed at the copper-aluminum and the aluminum-copper boundaries for every time step during welding in order to calculate D_{ac} (Chapter 4).

Figure V-6A shows a magnified version of the back wall reflection at the current on moment. The text on every pixel represents its greyscale level. In the figure it is clearly seen how before the beginning of the welding process the gray level changes of the image F are considerable on the vertical direction ($\partial F/\partial y$) due to the nature of the image (A-Scans on each column). However, the delays created due to changes in temperature and material properties during welding cause a noticeable change in intensity in the horizontal direction ($\partial F/\partial x$) as well. As an illustration of this fact, Figure V-6B shows the direction of the gradient (∇F) of the same sub image. This vector, described in Equation V-4, provides important information about the magnitude (Equation V-5) and direction (Equation V-6) of the intensity changes.

$$\nabla F = \begin{bmatrix} \partial F/\partial x \\ \partial F/\partial y \end{bmatrix}$$ **Equation V-4**

$$|\nabla F| = \sqrt{\left(\frac{\partial F}{\partial x}\right)^2 + \left(\frac{\partial F}{\partial y}\right)^2}$$ **Equation V-5**

$$\theta = \tan^{-1}\left(\frac{\partial F/\partial y}{\partial F/\partial x}\right)$$ **Equation V-6**

Edge detectors are well known tools to identify such discontinuities. There are a large number of edge detection operators available. However, by far, the most commonly used algorithm [7-8] is the Canny edge detector [9]. Canny mathematically formalized an optimum edge detector that satisfies a set of goals: 1 - Good Detection: locate all real edges. 2 - Good Localisation: minimal distance between the detected edge and 3 - Clear Response: only one response per edge. The first step of the canny algorithm is to perform linear filtering with a Gaussian kernel to smooth noise and then compute the edge strength and direction for each pixel in the smoothed image. This is done by differentiating the image in both dimensions and computing the gradient magnitude (strength) and direction (Equation V-5, Equation V-6). Candidate edge pixels are identified as the pixels that endure a thinning process called non-maximal suppression. In this process, pixels are eliminated based on the comparison of its strength with its neighbours (based on the gradient direction). After, thresholding is performed using hysteresis. In hysteresis two thresholds are used. All the surviving pixels below the lower threshold (T_L) are labeled as non-edges and all pixels above the high threshold (T_H) are labeled as edge pixels. Finally the pixels with strength between the lower and higher

thresholds ($T_L < |\nabla F| < T_H$) that are connected with any edge pixel ($|\nabla F|) > T_H$) are labeled as edge pixels as well.

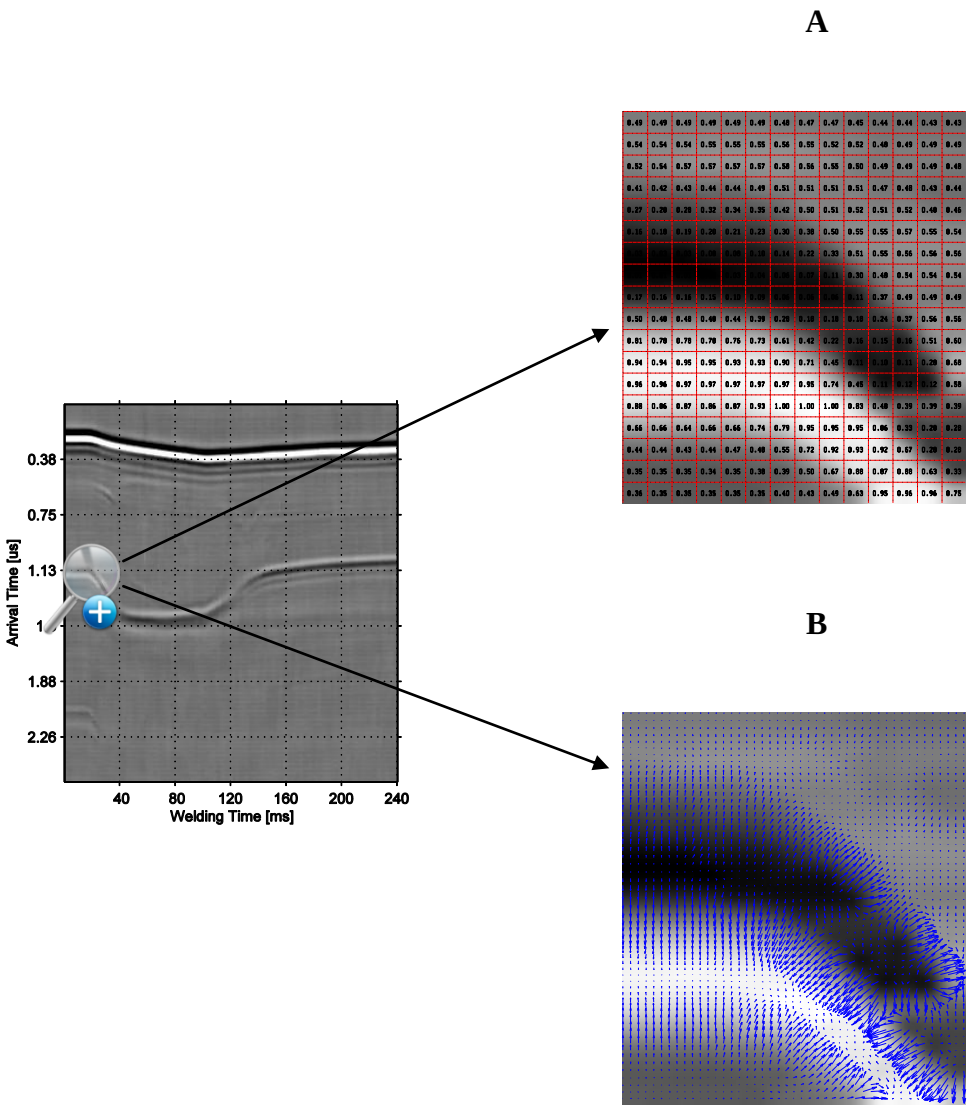

Figure V-6- Image gradient. A- Intensity values. B- Direction of the gradient.

The huge differences in amplitude between the front and back wall reflection make the determination of a global threshold a hard task. If the thresholds are very high the back wall reflection may not be detected and if the thresholds are too low, noise and

undesired tails from the front wall reflection may be detected as a valid signal. To illustrate this fact Figure V-7 shows the edges detected by the canny method using $T_H = 0.01$ and $T_L = 0.006$ (thresholds determined by the algorithm described in [10]). To solve this issue, the first step of the proposed algorithm is the segmentation of the M-Scan in order to separate the front and back wall reflections. This was done using Equation V-7 which estimates the position of the back wall reflection b_r, using the known plate thicknesses p_1 and p_2, the speed of sound c at room temperature, and the sampling frequency f_s. Where f_r is the position of the front wall reflection obtained by the peak of the envelope method. After segmentation, the sub-images shown in Figure V-8A and Figure V-8B were processed independently.

$$b_r = f_r + \frac{2(p_1 + p_2)}{c} f_s \qquad \textbf{Equation V-7}$$

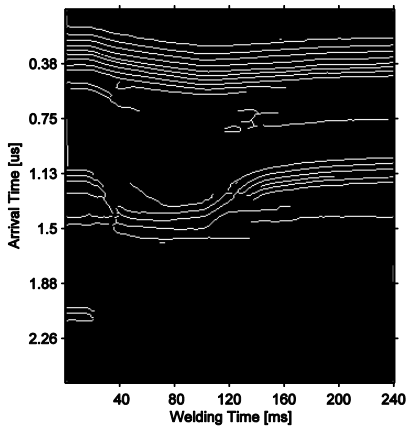

Figure V-7- Detected edges with T_H =0.01 T_L=0.006.

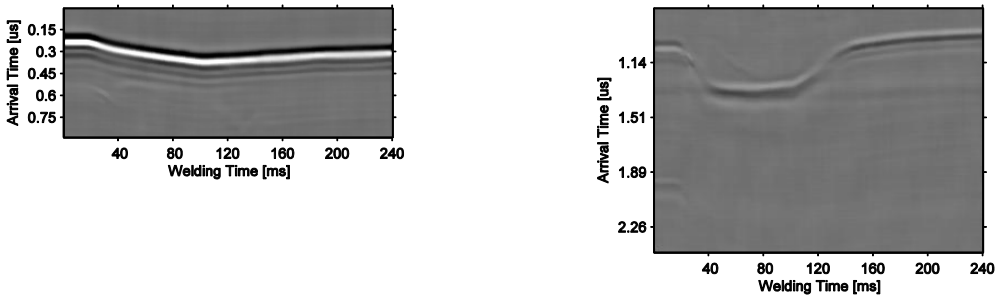

Figure V-8- Segmentation results. A-Front wall sub image. B-Back wall sub image

The segmentation allows the usage of four thresholds instead of two (hysteresis). It was already explained that the intensity changes are considerable on the vertical direction (*y*) and the delays created during welding also cause a noticeable change in intensity on the horizontal (*x*) direction. However, the magnitude of the gradient strongly depends of the changes on each individual A-Scan ($\frac{\partial F}{\partial y} \gg \frac{\partial F}{\partial x} \therefore |\nabla F| \approx \frac{\partial F}{\partial y}$). Using these two facts, the determination of the thresholds for each sub-image can be calculated by analyzing a training set of *N* A-Scans *a* obtained before the beginning of the welding process. The thresholds for each sub-image were calculated using the equations shown below (Equation V-8 - Equation V-10).

$$d_i = \max\left(\frac{\partial a_i}{\partial y}\right) \text{ where } i = 1,2,\dots,N \qquad \textbf{Equation V-8}$$

$$T_L = \frac{1}{N}\sum_{i=1}^{N} d_i \qquad \textbf{Equation V-9}$$

$$T_H = \max(d_i) \qquad \textbf{Equation V-10}$$

Figure V-9 shows the edges detected using the calculated thresholds. The figure clearly shows that noise was considerably reduced (compared to Figure V-7) and that, when the signal is present, the front and back wall reflection are detected. The edge detection results can be useful for M-Scans where the SNR on the individual A-Scans is high, for the rest of the cases where the amplitude of the back wall reflection decreases and in cases where the noise is higher the usage of a pattern recognition algorithm becomes apparent.

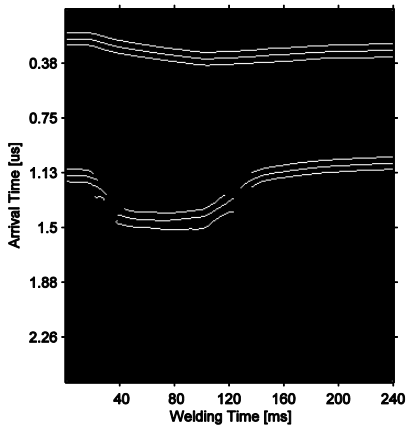

Figure V-9- Detected edges with T_{H1} =0.19 T_{L1}=0.10 T_{H2} =0.05 T_{L2}=0.03.

The application of pattern recognition algorithms such as the radon transform [11] or the Hough transform are common for the detection of straight lines in ultrasound images. For the detection of curves (back wall of aluminum M-Scans) these algorithms can be used iteratively in small windows [12]. However, when large portions of data are missing, which is very common on the back wall reflection of aluminum M-Scans due to electrode deterioration, these algorithms tend to fail. To solve this problem, an algorithm

for finding principal curves was applied in the edges of the detected interfaces. This algorithm was introduced by Verbeek in [13] and its main objective is detecting the curve that *"passes through the middle of the (curved) data cloud"* [13]. This is achieved first by extending the well known clustering algorithm k-means [14] in order to detect k-lines which in a later stage are decomposed into segments, the details of the algorithm are out of the scope of this dissertation but can be found in the original publication of the method [13].

The data used in the principal curve algorithm was only the non-zero pixels obtained in the edge detection stage. In Figure V-10 you can see the data used for the back wall reflection on black and the principal curve detected in blue. In the figure it is shown that the detected curve is continuous and its position matches the center of the data cloud, also it is clear that the algorithm is able to interpolate the areas where the signal is not present such as the melting and solidification moments. To illustrate that the position of the curve is correct Figure V-11A shows the detected line overlaid with the original M-Scan. It's clearly seen that the detected curve follows the back and front wall consistently. It's important to notice that this algorithm was used on the correlations studies (D_{ac}– nugget diameter) described in chapter 4. Finally, Figure V-11B shows a binary image highlighting the detected curve, this figure can be compared to the results shown in the previous section, note that the last section of the chapter will show a direct comparison of all the methods described in this chapter.

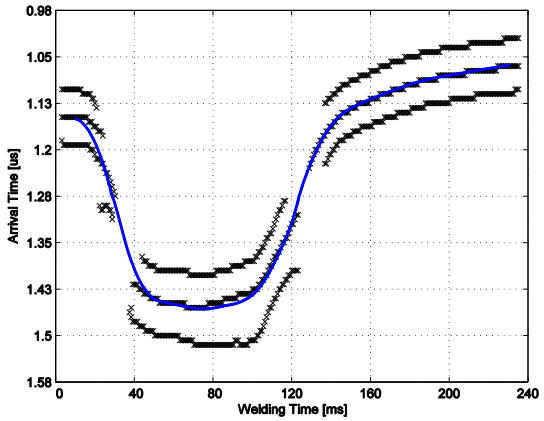

Figure V-10- Back wall reflection data (black) and principal curve detected (blue).

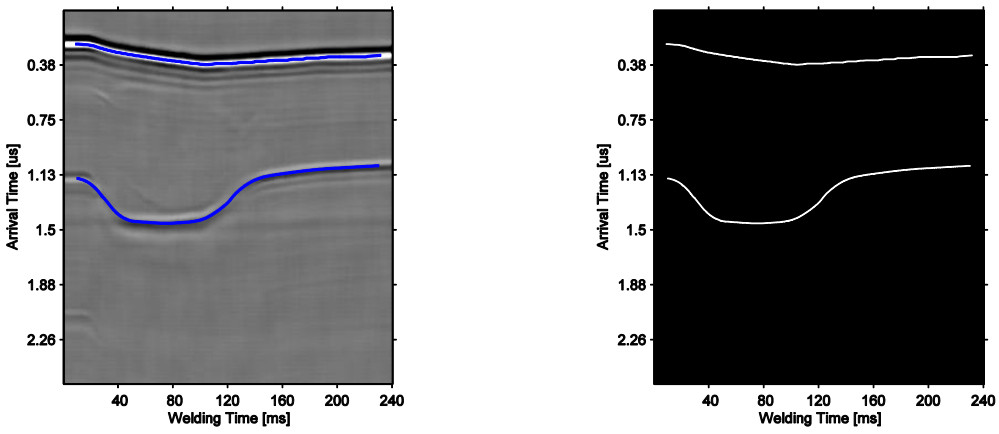

A **B**

Figure V-11- Principal curve detection results. A.- Detected curved overlaid with the original M-Scan. B.- Binary image marking the detected curve.

Liquid Reflections Detection

The detection of the weak reflections caused by the molten metal (reflections number 2 and 3 Figure IV-1) is a challenging task. The amplitude of these reflections is very low and often is obscured by the tails of the other interfaces and noise. The detection of these reflections is a key aspect in order to measure the liquid penetration of the weld.

The first step for the detection of these reflections is the same approach described in the previous section, segmentation. The position of the front and back wall reflection (f_r and b_r) are already known (Equation V-7), therefore a third sub-image can be obtained by segmenting the M-Scan between these two positions. Figure V-12A shows an aluminum M-Scan and the segmentation results (Figure V-12B).

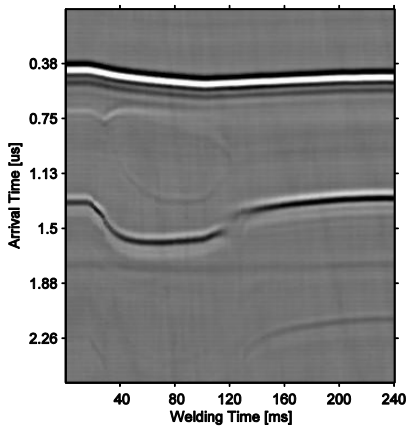

A

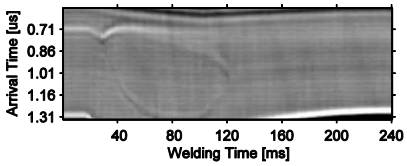

B

Figure V-12- Segmentation of liquid reflection area. A.- Original M-Scan. B.- Segmentation results.

The solid-liquid and liquid-solid reflections during solidification and melting show a linear behaviour (Figure V-12B). The gradient analysis described in the previous section revealed that these reflections show a strong vertical component. Therefore, the Sobel operator [15] on the vertical direction was used to enhance these reflections. Figure V-13A shows the results of this operation. A threshold was then applied to the results. This step has as a result a binary image highlighting the liquid reflections (Figure V-13B).

A **B**

Figure V-13- Filtering and thresholding results. A.- After Sobel. B.- Thresholding results.

The usage of the Hough transform to detect these reflections has proven to be efficient [12]. Figure V-14B shows the lines detected after processing the thresholded image with the Hough transform. The detected lines during solidification now can be used to measure the liquid penetration and the lines near the current on moment can be used to measure the elapsed time for melting.

A **B**

Figure V-14- Hough transform results. A.- Segmented M-Scan. B.- Lines detected.

Figure V-15A shows the pattern detected overlaid with the original M-Scan, and Figure V-15B binary image summarizing the information extracted from the ultrasonic M-Scan. The front and back wall reflections were extracted using the procedure described on the previous section and the liquid reflections were extracted by performing the Hough transform on the sub-image shown in Figure V-14A.

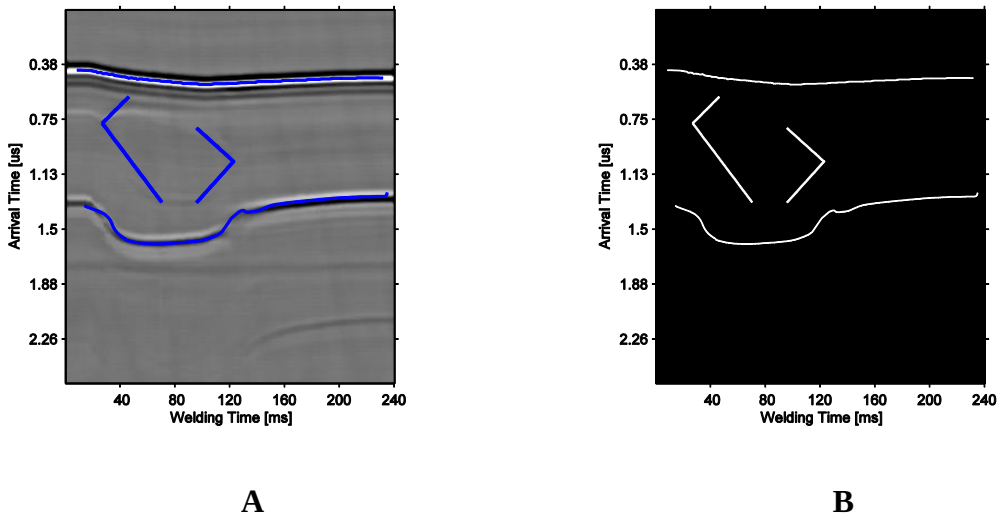

Figure V-15- Recognized pattern. A.- Pattern overlaid on M-Scan. B.- Thresholded pattern.

Quality Characterization Using Fuzzy Inference

Once the full pattern is recognized, a final decision about the weld quality needs to be taken. While the estimated nugget diameter and the measured liquid penetration provide enough information to judge the weld, the simple thresholding of these values to determine if the weld is “good” or “bad” is very imprecise. Qualifying one weld as good, and another one fractions of a millimeter smaller as bad, makes no sense in actual

production. Besides, experience with the final user indicates that when inspecting thousands of welds such detailed quantitative data is not necessary and might be misleading.

To solve these issues the actual RIWA system (for steel) uses a fuzzy inference system (FIS) that has as an output three linguistic variables, green, yellow and red corresponding to welds with good, acceptable and bad quality respectively [4]. In such way, the personnel in charge of the welding process may use this information to detect failures in the welding equipment. For example, if yellow welds start to appear frequently this indicates that weld size has decreased and maintenance will be needed in the near future. However, if red welds appear frequently an immediate corrective action is required.

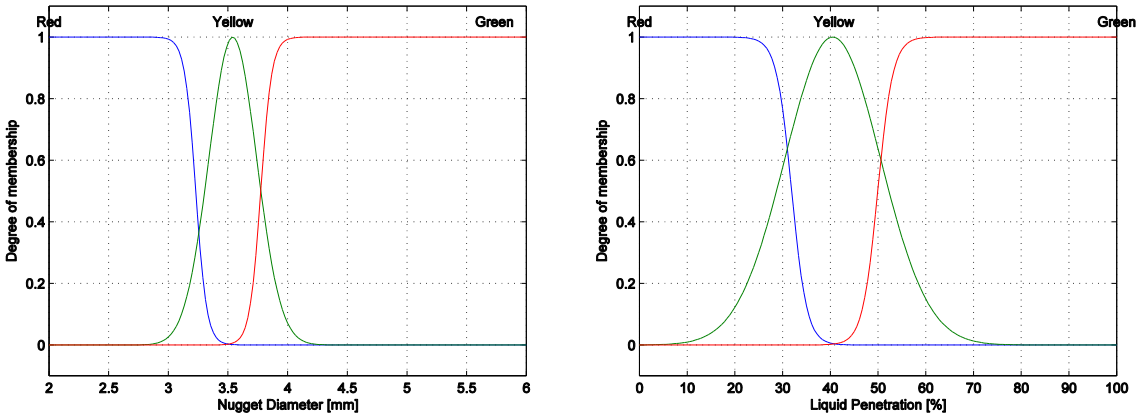

Figure V-16- Membership functions. A.- Nugget Diameter. B.- Liquid Penetration

The inputs of the FIS are the fuzzified weld parameters (nugget diameter, liquid penetration, moment of melting, among others). Figure V-16 shows the member functions used to fuzzify the nugget diameter (Figure V-16A) and liquid penetration parameters (Figure V-16B). The fuzzified inputs were then combined by a set of fuzzy rules. Since the final quality decision should be based on the result of all the fuzzy rules, the rules results must be combined as well. Aggregation is the process by which the rules fuzzy sets (outputs of each rule) are combined into a single resulting fuzzy set. The aggregation method chosen was the summation method [4]. Finally, the resulting fuzzy set must be defuzzified in order to resolve a single quality output value. The defuzzification method used was the centroid calculation [4]. Figure V-17 shows the defuzzification map for the nugget diameter and liquid penetration parameters. Note that the color represents the final quality of the weld.

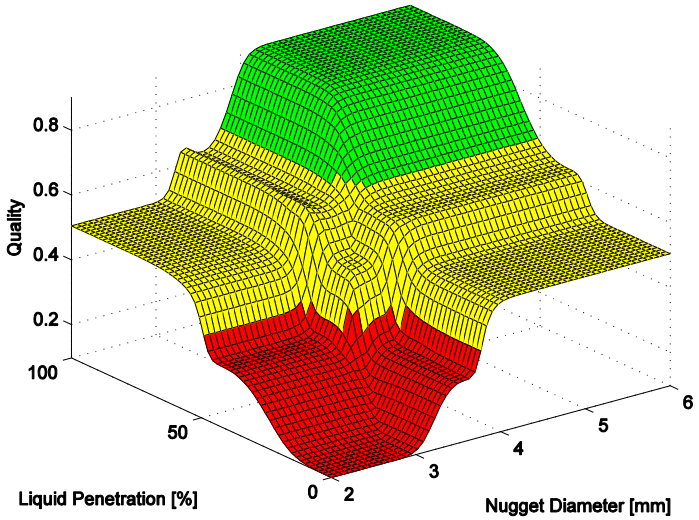

Figure V-17- Defuzzification results.

Since the mechanical properties and hence the quality of the weld in aluminum and steel depend on the same parameters which are the geometric properties of the nugget (diameter and liquid penetration). The methodology developed to judge steel spot welds quality using these two parameters remained unchanged for the aluminum system. However, due to the instability of the aluminum welding process and the rapid electrode deterioration explained on chapter 1, several parameters (electrode temperature, moment of melting and heating rate) were incorporated into the final aluminum FIS.

Conclusions

This chapter described how the aluminum M-scans were processed in order to extract useful information and determine the weld quality. The first two sections of the chapter were focused on determining D_{AC} the parameter used to estimate nugget diameter. Several methods were implemented and tested and also a multi-step principal-curve detection algorithm was proposed to achieve this task. The results were presented as binary images. Figure V-18 shows a comparison of all the methods in a single figure. The coordinates of the non-zero pixels on each binary image are plotted as individual data sets. The figure clearly shows that when the SNR is high, such as the front wall and the back wall reflection before and after welding, the variation of the detection between each method is minimal. However, when the SNR drops in regions such as the melting and solidification moment, the only method that is able to detect the reflection is the principal curve method.

To compare the implemented methods quantitatively the root-mean-square error (RMSE) between each method and the proposed method was calculated. Also the processing time of each method was measured. Note that these measurements were done in an experiment where 100 M-Scans were processed. The algorithms were implemented on Matlab and the processing time measurements were done on a PC with 4 GB of RAM and a Dual Core processor running at 3.2 GHZ. Table V-1 shows these results. The lower error (35 ns) was obtained by the peak of the envelope method. This indicates that the principal curve method and the peak of the envelope resemble each other since both detect the pulse based on the center of its energy. However, the principal curve method takes advantage of repetitive patterns between neighbouring A-Scans and is able to automatically interpolate the position of the pulses when the SNR is low. Therefore, when the SNR is high enough it is recommendable to use the peak of the envelope since it is less computationally expensive. The methods with higher errors are the continuous wavelet transform (CWT) and the max amplitude method, this is mainly caused by the outliers generated at the moment of melting and solidification (Figure V-18), but also because of the artificial discontinuity on the back wall reflection due to the frequency-dependent attenuation and signal shape change.

Timing wise, the slower method is the CWT with 22 seconds of average processing time. This is caused by the numerous calculations required to detect a single A-Scan. The principal curve method has an average processing time of 1.14 seconds. It's important to notice that the algorithms implementation was not optimized. The usage of a programming language such as C++ and parallelism techniques should reduce the timing

by several orders of magnitude. The timing results shown in Table V-1 are merely a comparison between methods.

Method	RMSE (ns)	Average Processing Time (ms)
Max Amplitude	56	100
Peak Envelope	36	600
Cross Correlation	45	700
CWT	68	22,000
Principal Curve	--	1140

Table V-1 – Comparison of signal detection methods.

Another quality parameter is liquid penetration. This parameter was measured by detecting the low amplitude reflections caused by the top and bottom of the molten nugget. The approach to achieve this task was to segment the M-Scan and obtain a sub-image containing only these two reflections. The sub-image was then filtered in order to enhance and threshold the reflections. Finally using the binary image, the Hough transform was used to detect the linear patterns formed by the nugget reflections. Lastly, a fuzzy inference system was introduced on the last section of the chapter. This system receives the weld parameters extracted from the M-Scans which are fuzzified by a set of membership functions. After processing the inputs by a set of fuzzy rules, the system produces as an output the level of quality of the weld (green, yellow or red).

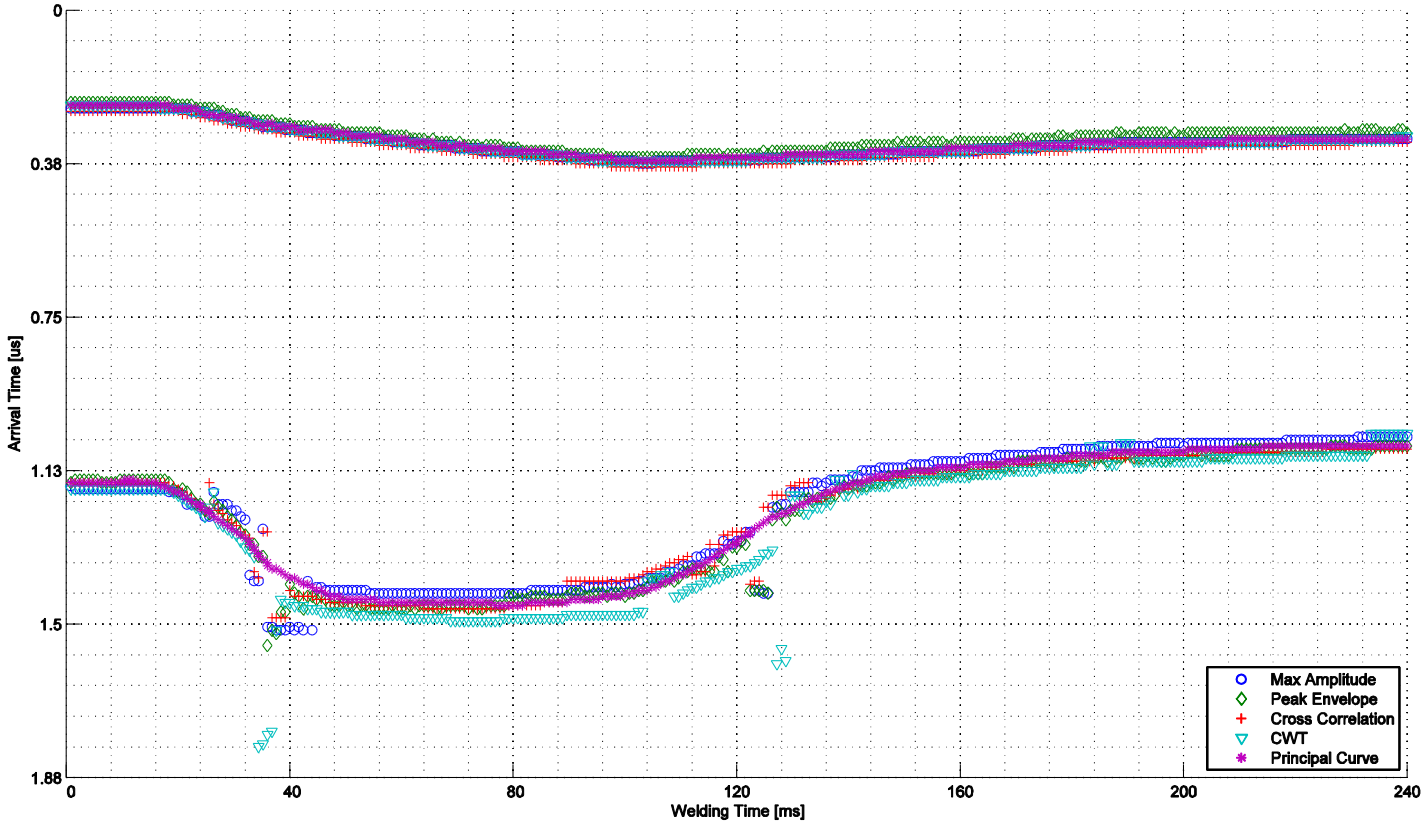

Figure V-18- Comparison of signal detection methods.

132

Figure V-19 show the fuzzy inference system results after processing a set of aluminum M-Scans. Different views of the 3D relation between the quality, the estimated nugget diameter and the measured liquid penetration are presented. In Figure V-19A is clearly seen that the experimental data follows the 3D surface shown in Figure V-17. When analyzing each input individually (Figure V-19B - Figure V-19D) the effect of the input membership functions (Figure V-16) and the non-linear multi-parameter mapping that the fuzzy system provides it's seen. For example, the data point marked with the blue bold line has an estimated nugget diameter of 4.8 mm. If the final quality is judged based only on this parameter the weld will be called green. However, after the evaluation of the liquid penetration parameter (40%) and the defuzzification process, the quality has a final value of 0.6 which is labeled as yellow. This type of qualitative multi-parameter evaluation has attracted the automotive industry specially, since the decision parameters such as liquid penetration, nugget diameter and quality thresholds can be selected based on their individual quality policies.

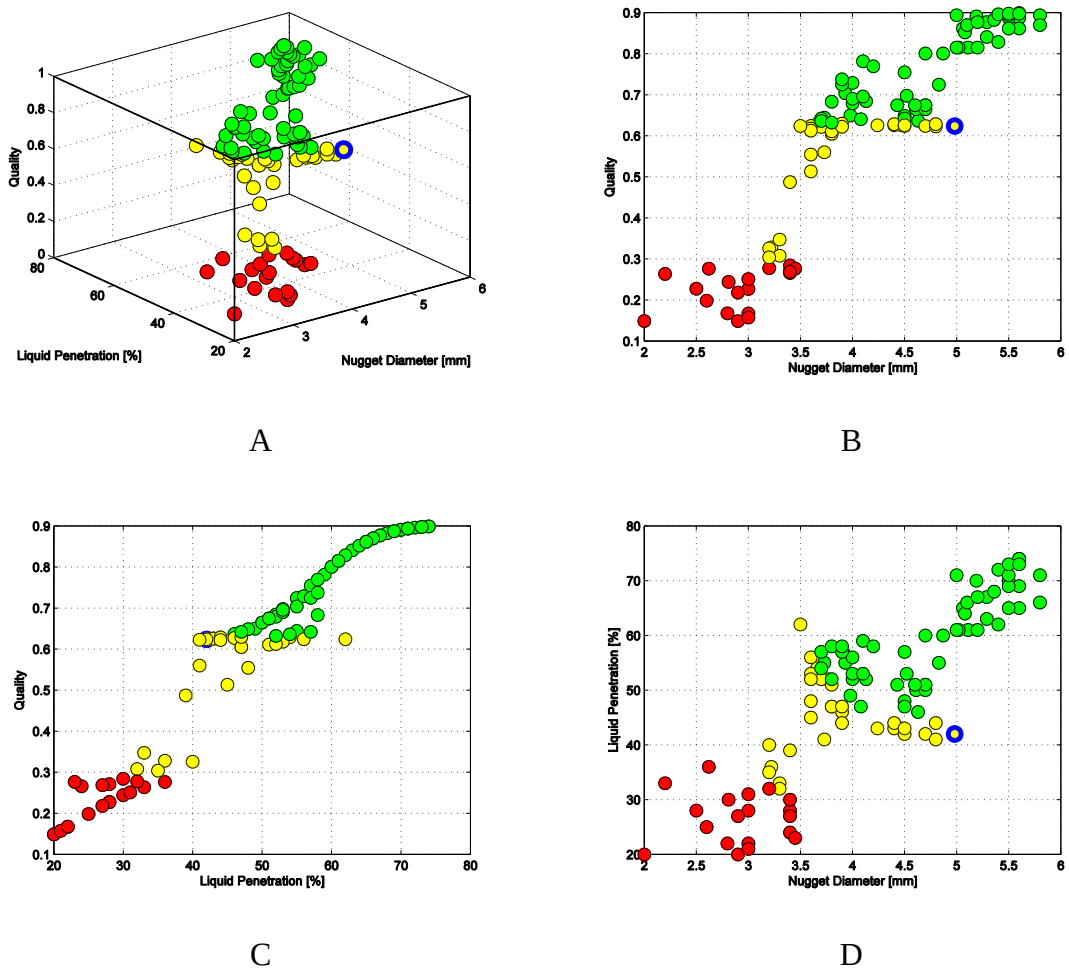

Figure V-19- Fuzzy inference system results for aluminum M-Scans. A- 3D view, B- nugget diameter – quality relation. C- liquid penetration – quality relation. D- nugget diameter – liquid penetration relation.

References

1. *Elaboration of some signal processing algorithms in ultrasonic techniques: application to materials NDT,* by R. Drai, F. Sellidj, M. Khelil, A. Benchaala. Ultrasonics, 2000. Vol. 38, No. 1, pp. 503-507.
2. *Peak Detection Methods for Ultrasonic Thickness Measurements*, by A. Rehbein. Internal Report, Laboratory for Machine Tools and Production Engineering RWTH Aachen University. 2011.
3. *Zero-crossing tracking technique for noninvasive ultrasonic temperature estimation*, by K.C. Ju, H.L Liu. J. of Ultrasound Med Nov 2010. Vol. 11. No. 11, pp. 1607-1615.
4. *Development of the New Physical Method for Real Time Spot Weld Quality Evaluation Using Ultrasound*, by A.M Chertov. PhD dissertation 2007, University of Windsor.
5. *Wavelet-Based Edge Detection In Ultrasound Images*, by J.H. Kaspersen, T. Lango and F. Lindseth. Ultrasound in Med. & Biol. 2001. Vol. 27, No. 1, pp. 89-99.
6. *The Wavelet Transform: Some Applications to Fluid Dynamics and Turbulence*, by J. Liandrat, F. Moret-Bailly. Eur J Mech B/Fluids 1990. Vol. 9, No. 1, pp. 1-19.
7. *Study and Comparison of Various Image Edge Detection Techniques,* by R. Maini, H. Aggarwal. International Journal of Image Processing (IJIP) 2009. Vol. 3, No. 1, pp. 1-11.
8. *Comparison of Edge Detection Algorithms Using a Structure from Motion Task,* by M.C. Shin, D.B. Goldgof, K.W. Bowyer and S. Nikiforou. IEEE Transactions

on Systems, Man, and Cybernetics Part B, August 2001. Vol. 31, No. 4, pp. 589-601.

9. *A Computational Approach to Edge Detection*, by J. Canny. IEEE Transactions on Pattern Analysis and Machine Intelligence, November 1986. Vol. 6, pp. 679-698.
10. *Canny Edge Detection - Automatic/Adaptive Thresholding*. http://www.mathworks.com/matlabcentral/answers/30691.
11. *Extraction of the Straight Line Segments from the Noisy Images as a Part of Pattern Recognition Procedure*, by A.M. Chertov and R.Gr. Maev. Proceedings Advances in Signal Processing for NDE of Materials, Aug 2005. pp.25-31
12. *Real-time Expulsion Detection and Characterization in Ultrasound M-scans of the Resistance Spot Welding Process*, by A.C. Karloff. PhD dissertation 2013, University of Windsor.
13. *A k-segments Algorithm for Finding Principal Curves*, by J.J. Verbeek, N.A. Vlassisand, B. Krose. Pattern Recognition Letters, 2002. Vol. 23. No. 8, pp. 1009-1017.
14. *An efficient k-means clustering algorithm: analysis and implementation*, by T. Kanungo, D.M. Mount, N.S. Netanyahu, C.D. Piatko, R. Silverman, and A.Y. Wu. IEEE Transactions on Pattern Analysis and Machine Intelligence, July 2002. vol.24. No. 7, pp. 881-892.
15. *Estimation of bladder wall location in ultrasound images* by A.K Topper and M. E. Jernigan. Medical and Biological Engineering and Computing, 1991. Vol. 29, No. 3, pp. 297-303.

CHAPTER VI

CONCLUSIONS AND RECOMMENDATIONS FOR FUTURE RESEARCH

Dissertation Summary

Resistance spot welding is a widely used method for joining metal sheets. Since the process is fast and easy to automate, industries such as automotive manufacturing use spot welding as their primary joining technology. More than 4000 spot welds bond the final vehicle. Some of these welds are at critical points and a breakdown can cause mechanical malfunctions or even accidents. To prevent these issues, the non destructive inspection of each one of these welds is crucial. That is the research direction of the University of Windsor group, where the real time integrated weld analyzer (RIWA) has been developed. This product is able to ultrasonically inspect spot welds in mild and high strength steels during its manufacture.

Recent increase in environmental awareness has resulted in consumer demand and government regulations for better fuel efficiency vehicles. For this reason the use of light-weight metals and materials in the automotive industry is growing. Aluminum is a very good candidate to replace steel because of its high strength-to-weight ratio and natural corrosion resistance. However, the spot welding process in aluminum is rather unstable. Chapter 1 describes in detail the main difficulties of welding aluminum and the actual proposed solutions to solve those difficulties.

Preliminary studies showed that the RIWA system was not able to monitor spot welds manufactured in aluminum. The main objective of this dissertation was the development of the real-time ultrasonic inspection system of the aluminum spot welding

process. To achieve this task a deep analysis of the aluminum welding process was performed.

Chapter 2 presented an FEM model of the aluminum spot welding process. The model revealed that contact resistance has a considerable effect on heat generation during the aluminum spot welding process. It was observed that the melting and nugget height growth is accelerated the first milliseconds of the process, followed by a stabilization of temperature on the vertical direction and diameter growth. A FDM model of the acoustic wave propagation through the aluminum spot welds (described on the same chapter) revealed that time of flight (TOF) of the wave passing through the aluminum spot weld does not correlate with the nugget diameter. This discovery was of utmost importance since TOF is the main parameter used to judge the quality on steel spot welds.

In order to acquire useful ultrasonic data, a special acquisition board was developed. The new board is capable of generating and receiving ultrasound signals, converting them into digital form, and sending them to the PC in fractions of millisecond. The development of this board was possible thanks to the hardware research team who are also the creators of the original RIWA hardware.

Chapter 3 presented an experimental characterization of the aluminum spot welding process together with new alternatives to improve the aluminum spot welding process. By using the ultrasonic system; interesting variables such the heat generation on each individual aluminum plate could be measured. With this information important guidelines to increase the electrode life were described. It was found that when welding dissimilar thickness sheets with DC equipment the electrode cap life can be extended by 60% just by facing the thinner plate towards the anode electrode. Also in chapter 3 a

novel technique using intermediate layers made by cold spray was also presented. By using this layer the usage of impulse welding on aluminum was possible. The current required in order to form an acceptable nugget size was dropped from 26.5 KA to 14 KA.

Chapter 4 presented a deep analysis of the aluminum M-Scans. Based on the results of the models presented on Chapter 2 an ultrasonic metric (D_{AC}) able to estimate nugget diameter from the ultrasonic data was proposed. Using this metric, it was found that nugget diameter estimation can be achieved with an average error of 0.7 mm. Also, it was found that liquid penetration measurements can be performed directly from the ultrasonic data.

Chapter 5 presented several algorithmic techniques to extract the exact position of the front and back wall reflection for every welding time in order to calculate D_{AC}. A multi-step algorithm that detects the principal curve formed at these reflections was proposed. Also a special procedure in order to detect the reflections caused by the top and bottom of the molten nugget was presented. Finally, a fuzzy inference system is used for the proper evaluation of the weld quality based on the already described ultrasonic parameters.

Recommendations For Future Research

The next step in the development of the inspection system should be the optimization and implementation of the proposed algorithms in order to have a closed loop feedback with the welding equipment. Based on the quality results, the RIWA system may send notifications to the welding equipment in order to correct the welding parameters and ensure the production of good welds.

Another area that has to be explored is the ability to monitor the lateral dimension of the weld geometry. The usage of a multi-element transducer may aid in the monitoring of the welding process of materials difficult to weld such as aluminum and magnesium and may help researchers to develop optimal welding schedules for such materials.

The cold spray technique described in chapter 3 may be applied on different materials or in combination of dissimilar metals. Current studies revealed that this technique may be useful to spot weld dissimilar metals such as Aluminum-Steel, Aluminum-Magnesium. The metallurgical processes of this technique should be studied in detail.

APPENDICES

A - Copper Properties

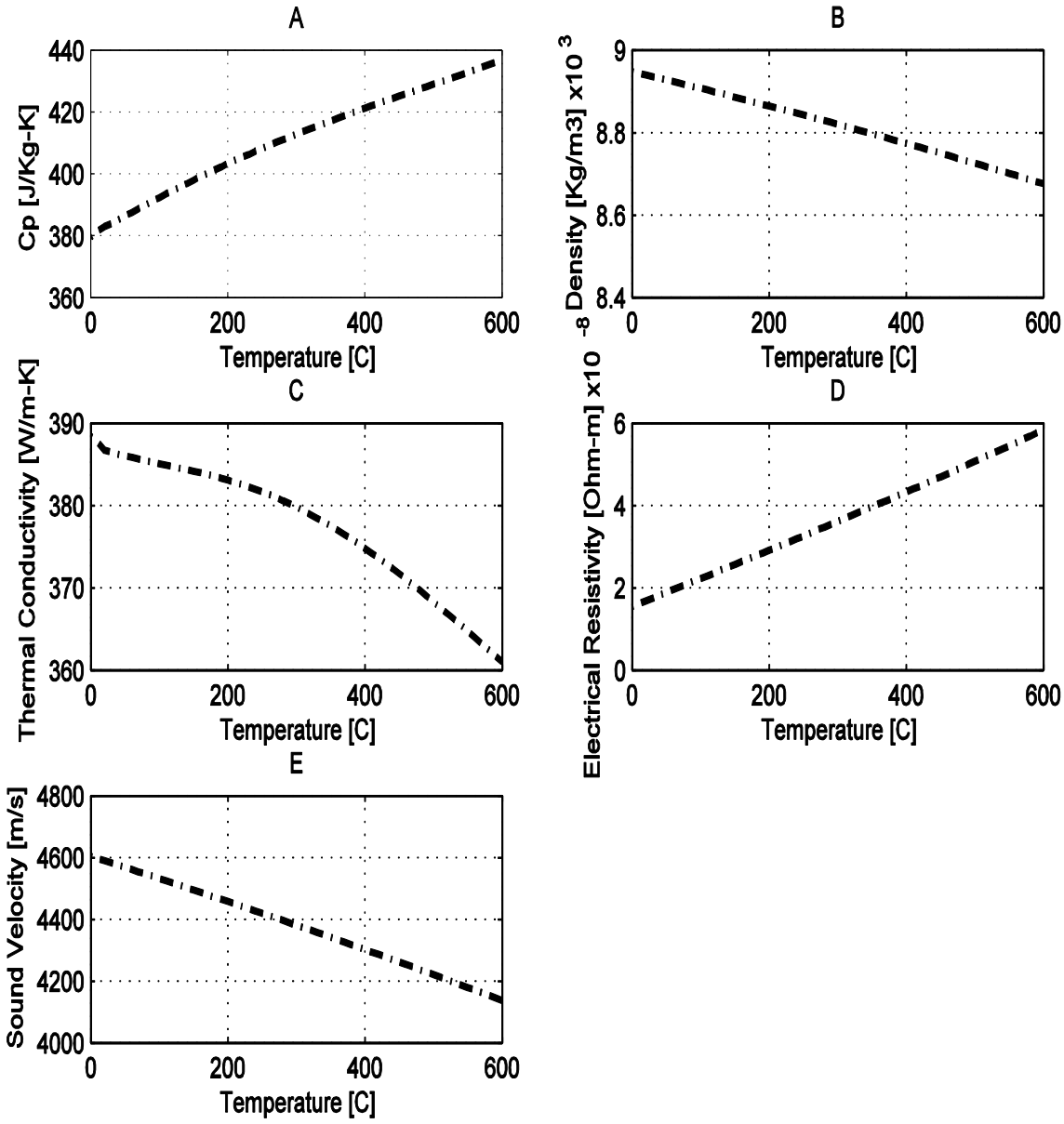

B - Copyright Permissions

Maney Publishing
Research · Knowledge · Innovation

www.maneypublishing.com

Waldo J. Perez Regalado
Institute For Diagnostic Imaging Research.
Inline Group.
Ph. D. Candidate University of Windsor.
Phone: (519) 253 - 3000 ext. 2681.
perezr@uwindsor.ca.

Tuesday 23rd April 2013

Dear Waldo Perez Regalado,

REF: Rashid, M; Medley, J B; Zhou, Y, 'Nugget formation and growth during resistance spot welding of aluminium alloy 5182', Canadian Metallurgical Quarterly, Volume 50, Number 1, 2011, pp. 61-71(11), Figure 3

I am writing to you in response to your request for permission to use the above figure to republish in your forthcoming Doctoral thesis entitled "Ultrasonic Real-Time Quality Monitoring Of Aluminum Spot Weld Process" at the University of Windsor, Ontario Canada. Permission is given subject to the proper acknowledgement of the publisher and copyright holder. Permission is also subject to acknowledgement of the original place of publication of the material listed above, in your forthcoming publication.

Please also list the URLs for the online version of this journal, the URLs are:

www.maneypublishing.com/journals/cmq and
www.ingentaconnect.com/content/maney/cmq

Please note that any elements of the article, whose copyright is owned by those other than the journal's copyright holder, will require further permissions prior to reuse. Please check all items carefully.

Please do contact me here with any further requirements or requests that you may have with regard to this matter.

Yours sincerely,

Rose Worrell
Editorial Assistant
r.worrell@maneypublishing.com

Leeds, UK • London, UK • Philadelphia, USA

Suite 1C, Joseph's Well, Hanover Walk, Leeds LS3 1AB, United Kingdom
Tel +44 (0)113 243 2800 • Direct Line +44 (0)113 386 81__ • Fax +44 (0)113 386 8178

Maney Publishing is the trading name of W.S.Maney & Son Ltd • Registration Number: 1922017 England VAT Number: GB 640 6260 62

VITA AUCTORIS

Waldo Josue Perez Regalado was born in Chihuahua, Chihuahua Mexico in 1983. He received his B.Sc. in Computer Science in 2004 from the Chihuahua Institute of Technology II, followed by M.Sc Degree in Electrical Engineering in 2007 from the Chihuahua Institute of Technology. During his masters he was involved in the design and implementation of a computer vision system capable of inspecting the quality of polarized lenses.

Waldo is currently a Ph.D. candidate in the Department of Electrical and Computer Engineering at the University of Windsor Ontario Canada working under the supervision of Dr. Roman Maev. His research focuses on the ultrasonic real-time quality monitoring of the Aluminum spot weld process. This project has been developed in collaboration with Chrysler, the Institute of Diagnostic Imaging Research (IDIR) and Tessonics Inc. Thanks to his involvement on this project Waldo was named as one of the 2013 top innovators under 35 (TR35) by the MIT's (Massachusetts Institute of Technology) Technology Review magazine Spanish edition. Also in 2011, Waldo, along with the welding research group, was awarded with the William Gardner award from the British Institute of Non-Destructive Testing. This award is granted to the best paper in the proceedings of the NDT Annual Conference by a person in the early stages of their career.